12-2014

Journal of Cave and Karst Studies, Volume 76, No. 3, December 2014

Malcom S. Field

JOURNAL OF CAVE AND KARST STUDIES

December 2014
Volume 76, Number 3
ISSN 1090-6924
A Publication of the National Speleological Society

DEDICATED TO THE ADVANCEMENT OF SCIENCE, EDUCATION, AND EXPLORATION

Published By
The National Speleological Society

The *Journal of Cave and Karst Studies* (ISSN 1090-6924, CPM Number #40065056) is a multi-disciplinary, refereed journal published three times a year by the National Speleological Society, 6001 Pulaski Pike NW, Huntsville, AL 35810-4431 USA; Phone (256) 852-1300; Fax (256) 851-9241, email: nss@caves.org; World Wide Web: http://www.caves.org/pub/journal/.
Check the *Journal* website for subscripion rates. Back issues are available from the NSS office.

POSTMASTER: send address changes to the *Journal of Cave and Karst Studies*, 6001 Pulaski Pike NW, Huntsville, AL 35810-4431 USA.

The *Journal of Cave and Karst Studies* is covered by the following ISI Thomson Services Science Citation Index Expanded, ISI Alerting Services, and Current Contents/Physical, Chemical, and Earth Sciences.

Front cover: LiDAR mapping in Lucas Cave, Jenolan. See Zlot and Bosse, in this issue.

R. Putiška, D. Kušnirák, I. Dostál, A. Lačný, A. Mojzeš, J. Hók, R. Pašteka, M. Krajňák, and M. Bošanský – Integrated geophysical and geological investigations of karst structures in Komberek, Slovakia. *Journal of Cave and Karst Studies,* v. 76, no. 3, p. 155–163. DOI: 10.4311/2013ES0112

INTEGRATED GEOPHYSICAL AND GEOLOGICAL INVESTIGATIONS OF KARST STRUCTURES IN KOMBEREK, SLOVAKIA

René Putiška[1]*, David Kušnirák[1], Ivan Dostál[1], Alexander Lačný[2], Andrej Mojzeš[1], Jozef Hók[2], Roman Pašteka[1], Martin Krajňák[1], and Marián Bošanský[1]

Abstract: A complex of geophysical methods were used to investigate a small karst area aimed at the production of detailed geological mapping, to confirm geological localization of known sinkholes, and to find possible continuations of caves and voids below the surface. The dipole electromagnetic profiling and radiometric mapping (the gamma-ray spectrometry method) were applied to determine the spatial distribution of hard carbonate rocks and weathered valley-fill sediments. Detailed high-definition magnetometry was carried out at selected sites in the studied region with the aim of distinguishing between sinkholes and man-made lime-kilns, pits where limestone was heated and transformed into lime. The microgravity and the electrical-resistivity tomography (ERT) methods were used to create high-resolution images of the underground cave. The results of ERT and the geological survey were used as an initial model for gravity modeling. Subsurface cavities of various sizes are contrasting geophysical objects, and the electrical resistivity can range from very conductive to relatively resistive depending on the composition of the filling materials. The interpretation of resistivity properties is not always straightforward. We must distinguish air-filled (high-resistivity) and loamy water-filled (low-resistivity) cavities and fractures. The combined geophysical methodology permits us to determine a more accurate near-surface geological model, in our case the parallel interpretation of a strong conductive anomaly in the ERT inversion and a predominant density decrease in the gravity modelling yield the presence of cavities at depths approximately of 50 to 60 m below the surface.

Introduction

Explored caves are only a limited portion of those actually existing underground (White, 1990; Ford and Williams, 2007). To obtain information about these hidden caves, or unknown or inaccessible continuations of known caves, we must use indirect methods (Parise and Lollino, 2011; Margiotta et al., 2012; Pepe et al., 2013). Near-surface geophysical methods have recently become an important tool in karst-caves research. The idea behind most of these geophysical methods is a material property of the void that is significantly different from the surrounding host rock and thus makes a material contrast. This material contrast can then be detected using a specific geophysical technique (e.g., Butler, 1984; Gibson et al., 2004; El-Qady et al., 2005; Dobecki and Upchurch, 2006; Nyquist et al., 2007; Mochales et al., 2008; Margiotta et al., 2012; Putiška et al., 2012a). Among some of the most frequently used geophysical techniques, electrical-resistivity tomography and microgravity can be mentioned, but additional methods can provide very useful information as well.

The studied region is located in the northeastern portion of the Malé Karpaty Mts., in the western part of Slovakia, and belongs to the Kuchyňa-Orešany karst. The northeastern part of Kuchyňa-Orešany karst is represented by the Komberek karst, which is a not large, about 1 km^2, but interesting karst plain, where two caves, the Strapek Cave and the Závrtová Priepasť Cave, were discovered. Besides the caves, more than seventy terrain depressions were found in the area (Fig. 1), but some of them are not karst landforms, as they are man-made lime kilns. The lime kilns were created during the fifteenth and sixteenth centuries to produce quicklime through the calcination of limestone. The kilns are up to 3 m in diameter and 1-m deep, which is very similar to some of the smaller natural sinkholes in the area. Therefore, we tried to find a method to reliably distinguish them. Several depressions are filled with mud and water, which makes it difficult to distinguish whether their origin is natural or not. The term mudholes is used for these structures in the following text.

A variety of geophysical techniques can be used to detect the presence of caves and voids below the surface (Cardarelli et al., 2010; Gambetta et al., 2011; Kaufmann et al., 2011; Lačný et al., 2012; Andrej and Uroš, 2012).

[1] Department of Applied and Environmental Geophysics, Faculty of Natural Sciences, Mlynská dolina G, 842 15 Bratislava, Slovak Republic
[2] Department of Geology and Paleontology, Faculty of Natural Sciences, Comenius University, Mlynská dolina G, 842 15 Bratislava, Slovak Republic
* Corresponding Author: putiska@fns.uniba.sk

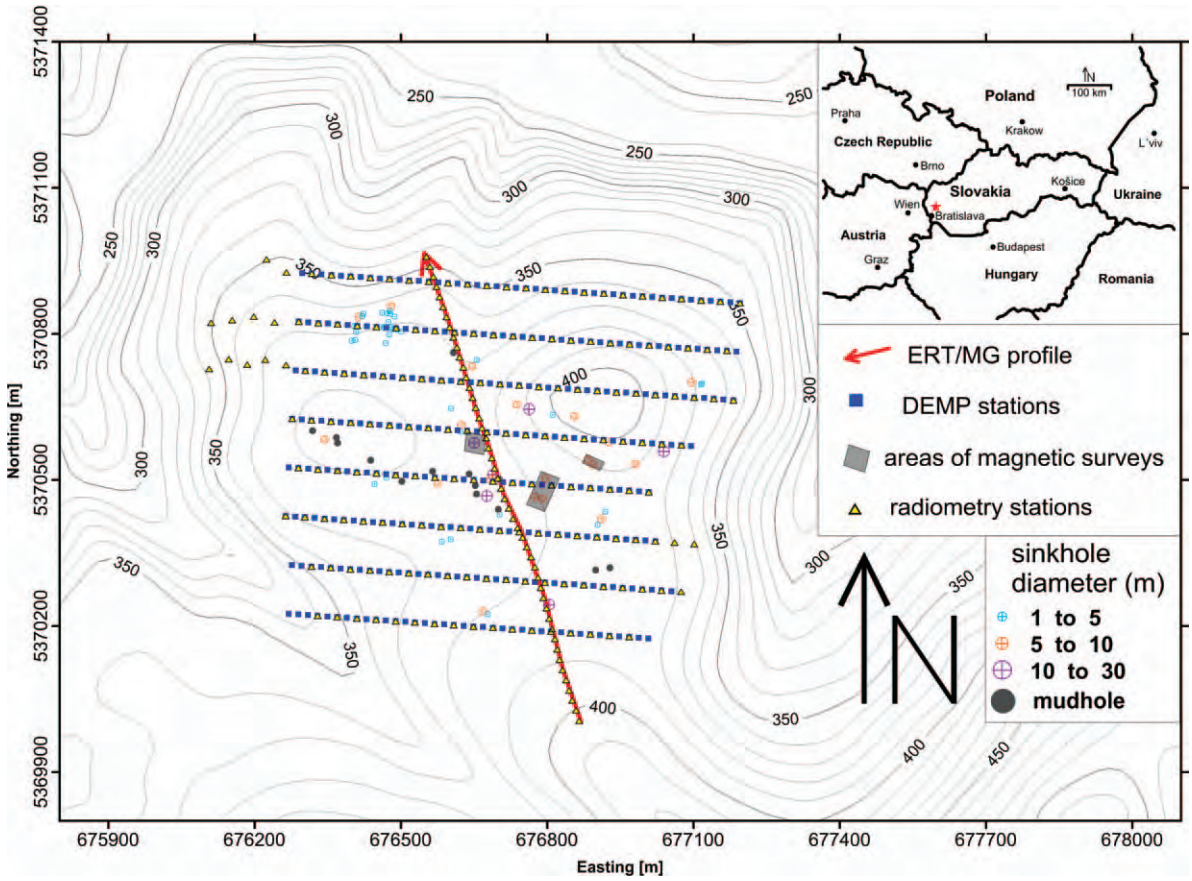

Figure 1. Topographic map of the study area showing the geophysical survey sites and karst structures. ERT is electrical-resistivity tomography, MG is microgravity, and DEMP is surface electromagnetic conductivity. Coordinates in Figures 1–3 are UTM zone 33N.

Each are based on a physical contrast between a cave and the surrounding rocks. Karst features are prevalent throughout the study area. Sinkholes develop by a cluster of inter-related processes, including bedrock dissolution, rock collapse, soil sapping, and soil collapse. Any one or more of these processes can create a sinkhole. The basic classification (Walthman et al., 2005) has six main types of sinkholes, solution, collapse, caprock, dropout, suffusion, and buried, that relate to the dominant process behind the development of the sinkhole. The dominant type of sinkholes within the Komberek karst area is solution, formed where surface water and soil water dissolve bedrock near the surface as it flows towards points where it can sink into fissured or cavernous ground. As mentioned above, the primary focus of our geophysical research was to map the site and to detect geological anomalies. On the basis of these results the plan for deeper investigations was set up. The aim of the survey was to detect karst features like sinkholes or fractured zones that could communicate with the underground network. New caves or extensions of known galleries were expected to be found too. The location of the geophysical survey is shown in Figure 1.

GEOLOGICAL SETTING

The Komberek karst area, as well as the Malé Karpaty Mts., are integral parts of the Western Carpathians orogenic belt. The Malé Karpaty Mts. geological structure consists of several tectonic units (Polák et al., 2011). The Tatricum tectonic unit is the most autochthonous unit comprising the Paleozoic crystalline basement and the Mesozoic sedimentary cover. The Fatricum and Hronicum tectonic units belong to the nappe structures of the Western Carpathians tectonically individualized during the Alpine orogeny during the Cretaceous period. The Tatricum unit in the studied area contains only the uppermost synorogenic flysch member, clayey shales, and turbiditic sandstones of Albian-Cenomanian age. An Upper Cretaceous thrust plane separates underlying Tatric from Fatric unit in its hanging wall. The Komberek area (Fig. 2) is built up almost exclusively by the Fatric unit's Middle to Upper Triassic and Jurassic members. Middle Triassic dark-grey to black thick-bedded Gutenstein type limestone is the prevailing rock type in this area, and it is also the lowermost part of Fatric unit. The tectonic contact between the Tatricum and the flysch sediments of the

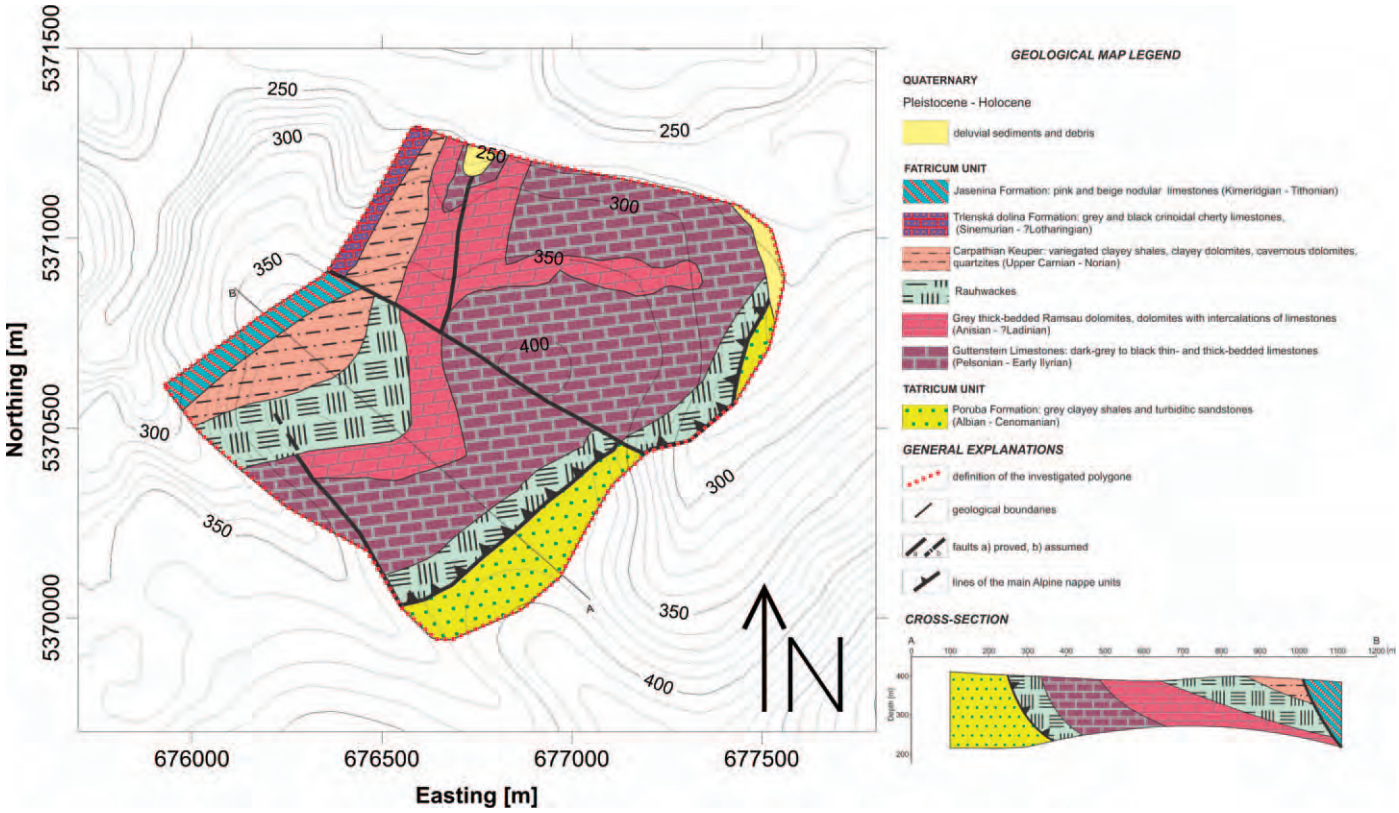

Figure 2. Geological map and cross-section of the Komberek area revised on the basis of the geological and geophysical investigations.

Fatricum units is linked to the rauhwackes. Rauhwackes (cornieules or cargneules) are breccias with a calcareous matrix and mainly dolomitic components that weather to form cavernous rocks. They are very often associated with tectonic contacts. The origin of rauhwackes is still controversial, but has been attributed to the weathering and alteration of dolomite-bearing evaporites, the tectonization of dolomites, or other processes (Krauter, 1971; Schaad, 1995). It is supposed that the rauhwackes are tectonically derived from the Gutenstein limestones. The Gutenstein limestones should be overlayed by Ramsau dolomites, but in this locality grey thick-bedded dolomitized limestones crop out. Variegated clayey shales, quartzy sandstones, and quartzstones, and also cavernous grey dolomites (rauhwackes) of Upper Triassic age belonging to Carpathian Keuper member overlie the Gutenstein and Ramsau carbonatic complex. In the northwestern part of the Komberek area there are Jurassic grey crinoidal cherty and pink nodular limestones. The Komberek area is disrupted by northwest-southeast oriented normal faults active during the Neogene (Polák et al., 2011). The sinkholes are localized along distinct lines situated along the litological and tectonic discontinuites. The main lithological discontinuity is between the Carpathian Keuper Formation and the Guttenstein limestones. The northwest-southeast tectonic line is the reason for the occurrence of the sinkholes array that follows it. An edited geological map is shown in Figure 2; because of the very flat morphology of the studied area and the scarcity of outcrops, geological mapping is very difficult.

Geophysical Methods

A complex of geophysical methods was designed to gather a large amount of geophysical information from the study area. The methods can be divided by purpose into two parts. The first part was an initial field investigation of the whole area. In this case, electromagnetic-conductivity, magnetometry, and gamma-ray spectrometry were used to map the site and to distinguish near-surface geological settings in the area. The information obtained was used to characterize the geological setting of the Komberek area (Fig. 2). The second part of the geophysical fieldwork included electrical-resistivity tomography (ERT) and microgravity survey on a selected profile across the karst area to obtain information about unknown or inaccessible continuations of known caves. The profile was based on the results from the geophysical work done during the first part of the investigation and also covers as many sinkholes and mudholes as possible (Fig. 1). During this stage, a

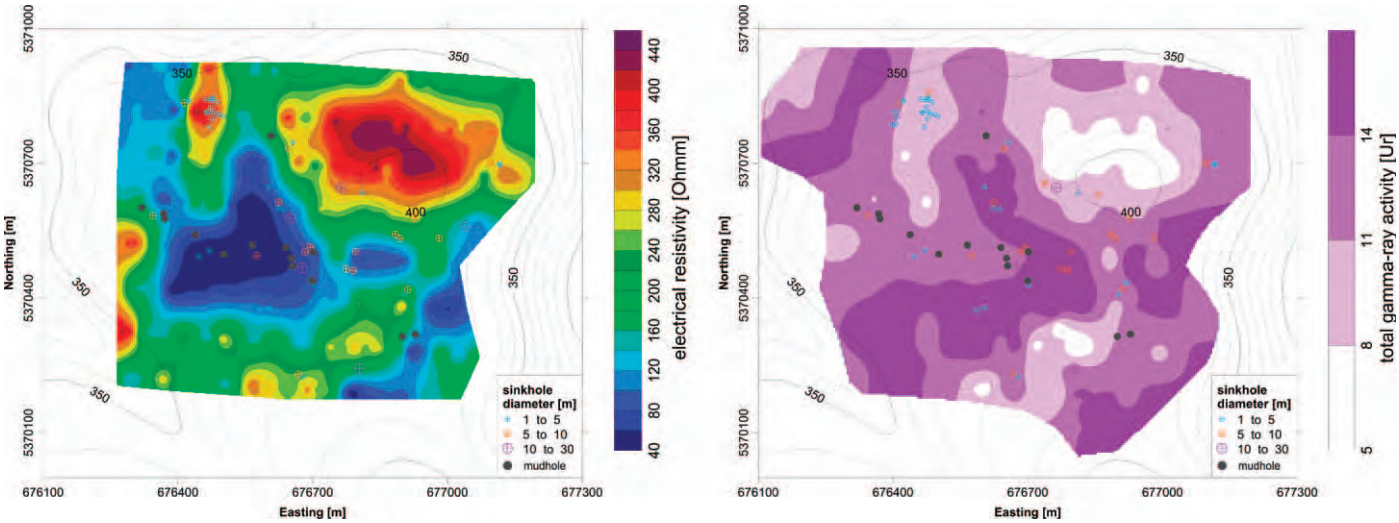

Figure 3. Result of surface electromagnetic conductivity and radiometry mapping. In the left-hand part is the map of apparent resistivity and the right-hand part is the map of total gamma-ray activity (Ur is a unit of radioactivity, 1 Ur ~ 1 ppm eU).

detailed magnetometry survey was performed on selected sinkholes, to distinguish between natural and human-made sinkholes.

All geophysical works were done simultaneously by measuring the coordinates using GPS or a total station. The coordinate system used in the figures is UTM, zone 33N.

A profile survey by the ground gamma-ray spectrometry method was used to study the radioactivity of rocks, soils, and covers in the study area. This method allowed us to determine four measures of gamma-ray activity of near-surface rock and soil horizon at each measured station: total gamma-ray activity eUt [Ur] (Ur is a unit of radioactivity, 1 Ur ~ 1 ppm eU), concentration of ^{40}K [% K], concentration of ^{238}U [ppm eU], and concentration of ^{232}Th [ppm eTh] where the letter "e" represents equivalent. The depth range is relatively shallow, no more than 1 m from the surface, but the method gives useful information mainly for geological mapping purposes. In situ measurements were carried out using a portable 256-channel gamma-ray spectrometer GS-256 (Geofyzika Brno, former Czechoslovakia) with 3′ × 3′ NaI (Tl) scintillation detector using a traditional ground survey procedure: grass, old leaves, and the thin uppermost humus soil layer were removed and ground surface was levelled in a circle area of 1 to 1.5 m in diameter at each measured station. Time of measurement was 2 minutes per station. In total, 226 stations were measured along eight parallel west-east profiles (PF1 – PF8) approximately 100-m apart and one transverse northwest-southeast profile (PF9) (Fig. 1) with a 40-m step between measurements. The other geophysical methods were carried out at the same stations on the profiles, controlled by GPS measurements.

Electromagnetic–conductivity mapping (DEMP, for Dipole ElectroMagnetic Profiling) was performed on the eight parallel profiles with lengths from 900 m to 740 m. The sampling interval of the measurement was 20 m, so the whole dataset covers 289 points. The measurement was done with a CMD-4 instrument manufactured by GF Instruments Inc. (Czech Republic), which has dipole center distance of 3.77 m, so the median depth of the electromagnetic investigation was around 6.0 m. The depth range for most of the points allowed us to reach the bedrock in the area with a negligible effect from the sediments. The most important advantage of electromagnetic conductivity is the possibility of obtaining quick and useful results that match very well with DC resistivity methods.

The 2D electrical-resistivity tomography line (Fig. 1) was collected using an ARES instrument (GF Instruments Inc.). The survey was 1006.5-m long and conducted with a dipole-dipole array with 5.5-m electrode spacing. The 88 electrodes were used simultaneously, with alternation of two current and two potential electrodes and a roll-along survey. For post-processing and data interpretation, the inversion program RES2DINV (Loke and Barker, 1996) was applied. It generates a topographically corrected two-dimensional resistivity model of the subsurface by inverting the data obtained from electrical imaging (Putiška et al., 2012a). A robust inversion (L_1 norm) was used because it is more suitable for detecting caves and sharpening linear features such as faults and contacts within complex geological settings of karst regions.

The same profile from the ERT method has been used for the microgravity survey and the stations were placed next to each electrode. The instrument used for this method was a single Scintrex CG-5 unit with a resolution of 1μGal (10^{-8} m s^{-2}). Due to thick vegetation cover in the area, it was not possible to measure the positions of the stations using differential GPS, therefore the locations of the gravity stations and nearby topography was obtained

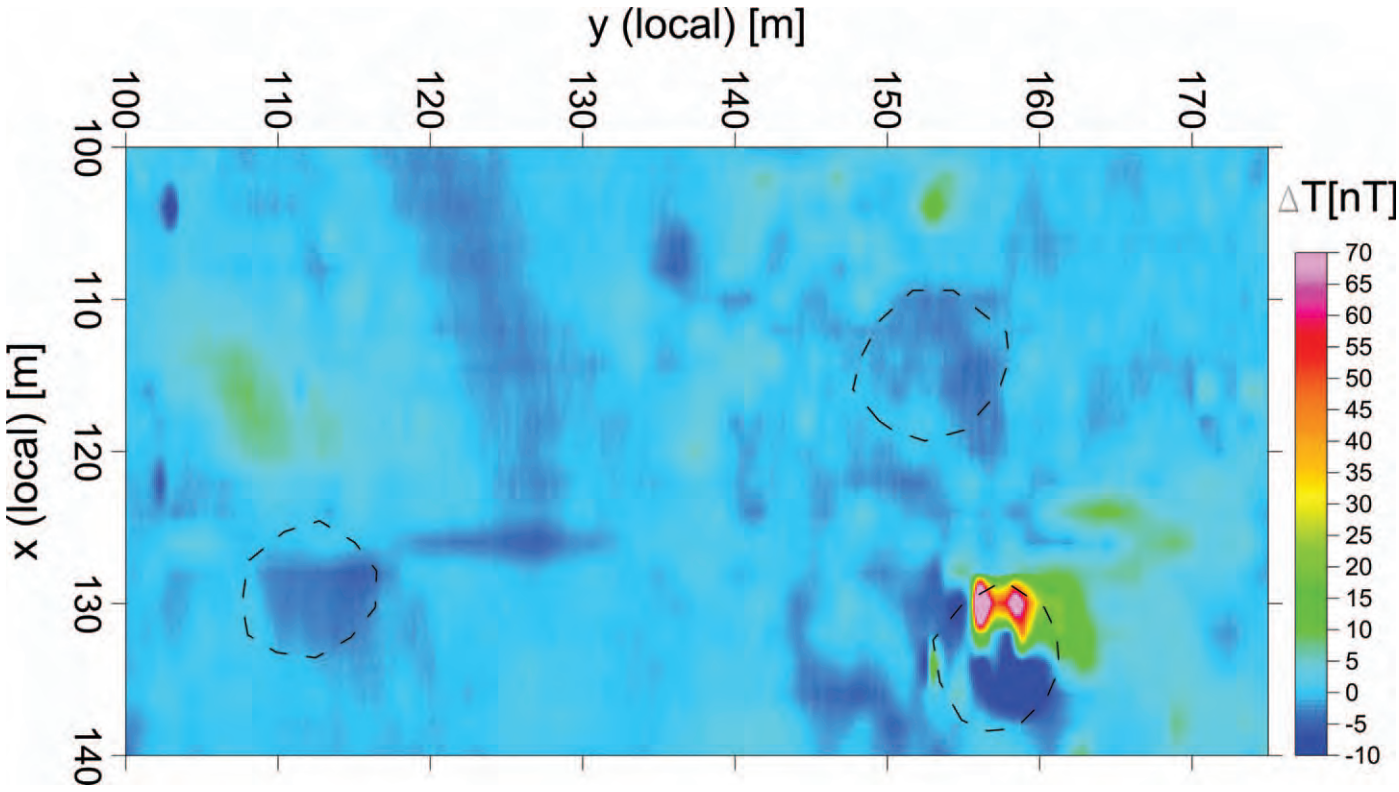

Figure 4. Results from one of the detailed magnetometry surveys. Terrain depression boundaries are shown by dashed lines. The depression in the lower right is shown to be an old lime kiln by the relatively strong dipole anomaly.

using Trimble M3 and Trimble S8 total stations tying to several GPS points in the vicinity of the profile. A total number of 184 gravity readings were processed to remove instrument drift, which was determined by repetitive measurement at the base station located in the center of the profile over a period of 2 hours and afterwards processed into form of complete Bouguer anomaly (Fig. 1).

Detailed high-definition magnetometry using a Cs-vapour magnetometer TM-4 with 0.2-m sampling step on lines 1-m apart was realized at selected sites of the studied region with the aim to distinguish between sinkholes and man-made lime kilns. Selected sinkholes are highlighted in the Figure 1 with grey rectangles that reflect the actual area surveyed by detailed magnetometry. The survey rectangles for detailed magnetometry on three sites were chosen due to practical reasons. The first two sites were placed on the largest sinkhole in the Komberek area and on a known man-made lime kiln identified by the burned lime residuals and ashes inside it. As the last site, a swarm of terrain depressions of uncertain origin, was chosen.

Results and Interpretation

The apparent resistivity map (Fig. 3) was obtained using the electromagnetic conductivity method (DEMP). The results show a good contrast between the high-resistivity areas composed of dolomite and limestone and the low-resistivity ones that are the effect of Quaternary sediments concentrated in the topography depressions. The majority of the largest sinkholes are concentrated on the boundary between low and high resistivity areas. This boundary was chosen for microgravity and ERT surveys. Results from the radiometric mapping are shown as a map of total gamma-ray activity (Fig. 3). The contour map of the total gamma-ray activity eUt distribution shows very good agreement with the picture of the apparent resistivity distribution for rocks and soils in the study area, as obtained by surface electromagnetic conductivity mapping (DEMP) measurement (Fig. 3). Lower-radioactivity areas correspond to higher-resistivity areas in maps and vice versa. Simultaneously both physical fields show good correlation with terrain topography in the study area (Fig. 3). Positive topographic features are mostly characterized by higher electrical resistivity and lower total gamma-ray activity values, whereas negative terrain features mostly show lower resistivity and higher total gamma-ray activity. This relationship is, of course, strictly determined by the geological structure of the area (Fig. 2), since the hard carbonates form topographical elevations characterized by higher electrical resistivity and lower total gamma-ray activity. Weathered rocks and Quaternary sediments fill topographic depressions in the central and southwestern parts of the study area, which are characterized by lower electrical resistivity and higher total

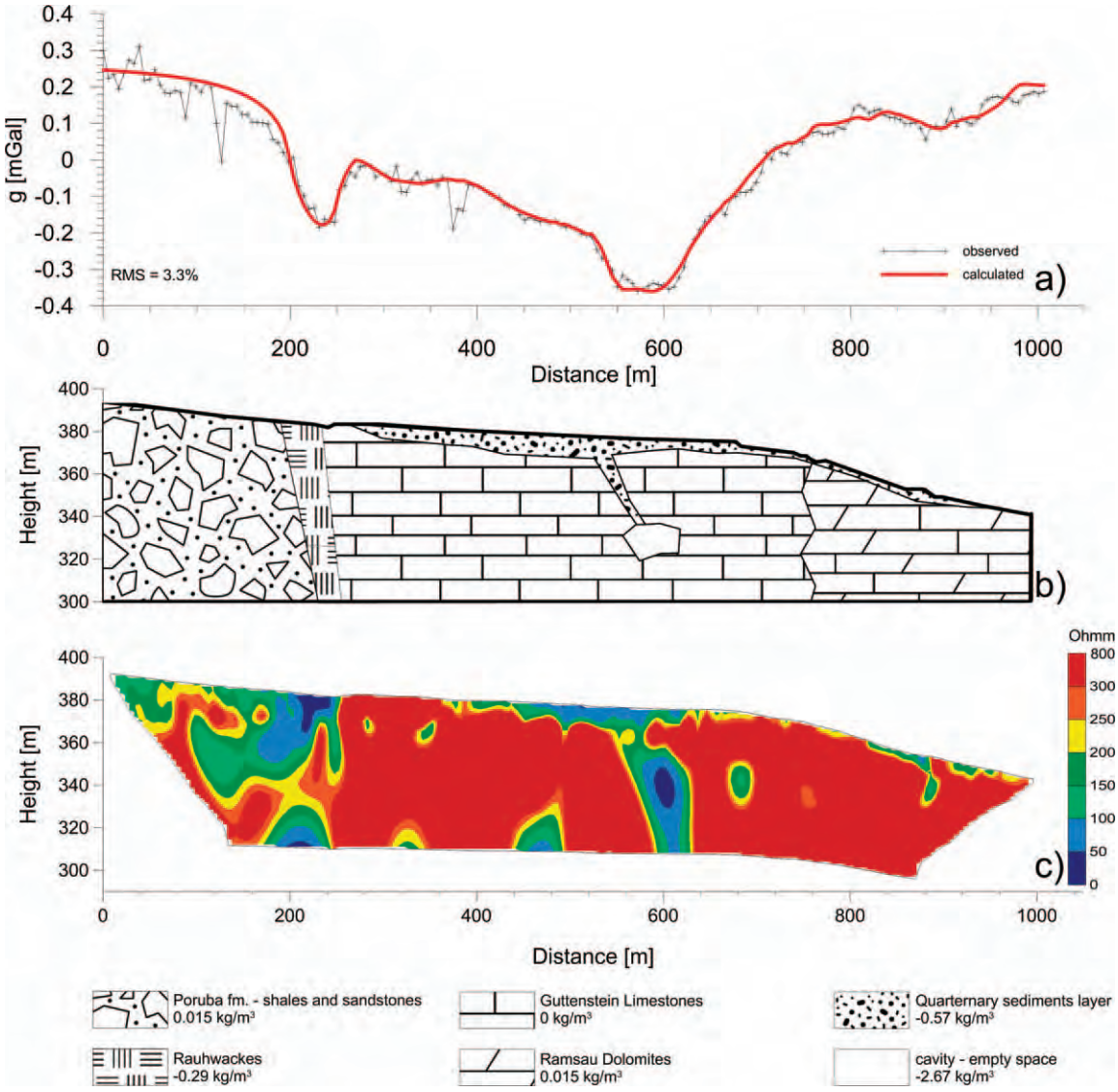

Figure 5. Results of the electrical-resistivity tomography and gravity modeling. The upper part of the figure (a) shows the correlation between the observed residual Bouguer anomaly and the model shown in the middle part (b). The ERT cross-section image is in the lower part of the figure (c).

gamma-ray activity. Generally, the two maps, the resistivity and the radioactivity, are quantitatively opposed to each other. In this way, the electromagnetic and radiometric surveys successfully outlined the boundary between valley fill and the carbonate rocks dolomite and limestone.

The total-field magnetic-anomaly map of the last of the survey rectangles is shown in Figure 4. The aim of the magnetic survey was to reveal contrast between sinkholes and man-made lime kilns. Due to the remnant magnetization produced during the heating processes we were able to easily recognize, based on qualitative interpretation, the lime kilns as having relatively strong dipole anomalies, as in the lower right of Figure 4.

Gravity and electrical-resistivity tomography methods were employed after the resistivity and radioactivity studies to detect possible cavernous structures in the selected profile across the whole area. Such caves can be empty, full, partly water-filled, or filled with a different kind of sediment. Air, water, or sediment-filled voids have a much lower density (air 0 kg m^{-3}, water 1000 kg m^{-3}, or sediment ~2000 kg m^{-3}) than the host rock for which the density of 2670 kg m^{-3} has been assigned. This difference in density is very significant and can be easily traced by gravity survey. Gravity, as an integral method, provides only information about the bulk composition of the subsurface. Therefore additional constraints are needed to model the Bouguer anomaly with appropriate structures. Electrical resistivity tomography is a reasonable choice due to the low cost of the survey and the high resistivity contrast that exists between an air-filled cavity

Figure 6. The sinkhole close to the electrical-resistivity tomography and microgravity line through the Komberek area. Diameter and depth of the sinkhole are ~ 25 m and 9 m, respectively.

and the surrounding formation (Zhou et al., 2002; Andrej and Uroš, 2012). Cavities can be also partially or completely water- or sediment-filled and, depending on the composition of the water, they might show a resulting electrical conductivity ranging from very conductive to relatively resistive compared to the host rock (Putiška et al., 2012b). The results of ERT and geological surveys were used as entries for the gravity modelling (Fig. 5). Gravity modelling was performed using the residual Bouguer anomaly computed for a reference density of 2670 kg m^{-3}. The zero elevation has been used as a lower boundary for the model, with 2-D geometry except the cavity body, which was modelled as a 2.5-D object with a lateral extension of 70 m and its center placed on the profile. To keep the model as simple as possible, only the most important features were taken into consideration, where the main structure of the lithological units was adopted from the geological map of the area. Received differential densities used for the model are shown in Fig. 5. Two important low density and low resistivity structures that can be important for the identification of karst structures were detected.

Figure 5b shows the final model, obtained from the combined interpretation of the microgravity (Fig. 5a) and ERT measurements (Fig. 5c). From microgravity (Fig. 5a) two important low density structures have been detected. The first Bouguer gravity minimum, with its center located on profile length 225 m and amplitude of −0.2 mGal, is associated with the geological setting in the area. The negative anomaly is produced from the lower gravity effect of the rauhwackes, which are porous and therefore have lower density (Fig. 2, Fig. 5b). The second, more significant minimum on the residual Bouguer anomaly curve, with amplitude lower than −0.35 mGal and center located at around 575 m, seems to be more interesting from a speleological point of view, as no gravity anomalies resulting from geology were expected there. Comparing the results with the ERT image, a strong conductive anomaly is visible at the same point on the profile as the main gravity minimum (Fig. 5a, c), where we inserted a

body representing an empty cave in Figure 5b. Empty space usually produces a high-resistivity anomaly in an ERT image, but in some special cases, as when the cave is partly filled with conductive material such as clay, the overall anomaly produced from the empty space can be conductive (Putiška et al., 2012b). The cave body in the final model (Fig. 5b) is connected to the ground by a communication channel, and its presence is also visible from the ground, where one of the largest sinkholes (diameter ~25 m) in the Komberek area was found (Fig. 6). The inverted ERT model (Fig. 5c) shows carbonate rock with a significantly higher resistivity (500 Ohm m) than the loamy material in the sinkhole, because of its considerably smaller primary porosity and fewer interconnected pore spaces. Loamy materials can hold more moisture and have higher concentrations of ions to conduct electricity; therefore, their resistivity values are below 100 Ohmm. The high contrast in resistivity values between carbonate rock and loamy material makes it possible to use electrical resistivity to determine the underground structure.

CONCLUSIONS

A geomorphological analysis of the Komberek area identified more than 70 topographic depressions. However, not all of them are karst landforms, as man-made lime kilns are also present in the area. Detailed high-definition magnetometry was successfully employed to distinguish between natural sinkholes and man-made lime kilns (Fig. 4). Results from the radiometric mapping and dipole electromagnetic profiling, supported by geological mapping, allowed us to refine the geological boundaries of the lithological units within the Komberek karst area (Fig. 2). By means of the resistivity tomography and microgravity methods, the final geological cross-section model of the area was constructed (Fig. 5b). The Bouguer anomaly curve (Fig. 5a) shows two dominant negative anomalies that were interpreted by introducing ERT inverse model and gravity forward modelling. The first negative anomaly, with center located at profile location 225 m and amplitude of −0.2 mGal, is associated with a presence of the porous rauhwackes formation and seems to be unimportant from a speleological point of view. The second major negative anomaly, with amplitude more than −0.35 mGal and center located at ~575 m, correlates with a conductive anomaly in the ERT inverse image at depth of ~60 m, where a cavity was detected. Lateral placement of this anomalous area is linked the presence of the largest sinkhole in the Komberek karst area. According to the results obtained from this study, we can conclude that microgravity together with electrical resistivity tomography have proved to be effective tools for imaging subsurface cavities in limestone at shallow depths. Thus, we believe that the presented methods and evaluation techniques could be successfully applied to other karst areas and potentially help in identifying hidden voids that possibly constitute karst hazards (see Parise and Gunn, 2007; De Waele et al., 2011 and references therein).

ACKNOWLEDGMENTS

The authors would like to thanks to an anonymous reviewer for his helpful comments that improved the final manuscript and to the Slovak Research and Development Agency APVV (Grant Nos. APVV-0194-10, APVV0625-11, APVV-0099-11, APVV-0129-12) and the Slovak Grant Agency VEGA (Grant Nos. 1/0095/12, 2/0067/12, 1/0747/11, 1/0712/11, 1/0131/14) for the support of their research.

REFERENCES

Andrej, M., and Uroš, S., 2012, Electrical resistivity imaging of cave Divaška jama, Slovenia: Journal of Cave and Karst Studies, v. 74, no. 3, p. 235–242. doi:10.4311/2010ES0138R1.

Butler, D.K., 1984, Microgravimetric and gravity gradient techniques for detection of subsurface cavities: Geophysics, v. 49, p. 1084–1096. doi:10.1190/1.1441723.

Cardarelli, E., Cercato, M., Cerreto, A., and Di Filippo, G., 2010, Electrical resistivity and seismic refraction tomography to detect buried cavities: Geophysical Prospecting, v. 58, p. 685–695. doi:10.1111/j.1365-2478.2009.00854.x.

De Waele, J., Gutiérrez, F., Parise, M., and Plan, L., 2011, Geomorphology and natural hazards in karst areas: a review. Geomorphology, v. 134, no. 1–2, p. 1–8. doi:10.1016/j.geomorph.2011.08.001.

Dobecki, T.L., and Upchurch, S.B., 2006, Geophysical applications to detect sinkholes and ground subsidence: The Leading Edge, v. 25, p. 336–341. doi:10.1190/1.2184102.

El-Qady, G., Hafez, M., Abdalla, M.A., and Ushijima, K., 2005, Imaging subsurface cavities using geoelectric tomography and ground-penetrating radar: Journal of Caves and Karst Studies, v. 67, no. 3, p. 174–181.

Ford, D.C., and Williams, P., 2007, Karst Hydrogeology and Geomorphology: Chichester, John Wiley & Sons Inc., 576 p.

Gambetta, M., Armadillo, E., Carmisciano, C., Stefanelli, P., Cocchi, L., and Tontini, F.C., 2011, Determining geophysical properties of a near-surface cave through integrated microgravity vertical gradient and electrical resistivity tomography measurements: Journal of Cave and Karst Studies, v. 73, no. 1, p. 11–15. doi:10.4311/jcks2009ex0091.

Gibson, P.J., Lyle, P., and George, D.M., 2004, Application of resistivity and magnetometry geophysical techniques for near-surface investigations in karstic terranes in Ireland: Journal of Cave and Karst Studies, v. 66, no. 2, p. 35–38.

Kaufmann, G., Romanov, D., and Nielbock, R., 2011, Cave detection using multiple geophysical methods: Unicorn cave, Harz Mountains, Germany: Geophysics, v. 76, no. 3, p. B71–B77. doi:10.1190/1.3560245.

Krauter, E., 1971, Zur Genese rauhwackiger Breccien der alpinen Trias an Beispielen aus der Schweiz und Österreich: Geologisch-Paläontologische Mitteilungen Innsbruck, v. 1, no. 7, 11 p.

Lačný, A., Putiška, R., Dostál, I., and Kušnirák, D., 2012, Využitie metódy ERT pri prieskume jaskýň v Havranej skale (Plavecký kras): Slovenský Kras (Acta Carsologica Slovaca), v. 50, no. 1, p. 41–60.

Loke, M.H., and Barker, R.D., 1996, Rapid least-squares inversion of apparent resistivity pseudosections by a quasi-Newton method: Geophysical Prospecting, v. 44, p. 131–152. doi:10.1111/j.1365-2478.1996.tb00142.x.

Margiotta, S., Negri, S., Parise, M., and Valloni, R., 2012, Mapping the susceptibility to sinkholes in coastal areas, based on stratigraphy, geomorphology and geophysics: Natural Hazards, v. 62, no. 2, p. 657–676. doi:10.1007/s11069-012-0100-1.

Mochales, T., Casas, A.M., Pueyo, E.L., Pueyo, O., Román, M.T., Pocoví, A., Soriano, M.A., and Ansón, D., 2008, Detection of underground cavities by combining gravity, magnetic and ground penetrating radar survey: A case study from the Zaragoza area, NE

Spain: Environmental Geology, v. 53, p. 1067–1077. doi:10.1007/s00254-007-0733-7.

Nyquist, J.E., Peake, J.S., and Roth, M.J.S., 2007, Comparison of an optimized resistivity array with dipole-dipole soundings in karst terrain: Geophysics, v. 72, no. 4, p. F139–F144. doi:10.1190/1.2732994.

Parise, M., and Gunn, J., eds., 2007, Natural and Anthropogenic Hazards in Karst Areas: Recognition, Analysis and Mitigation, London, Geological Society, London, Special Publication no. 279, 202 p.

Parise, M., and Lollino, P., 2011, A preliminary analysis of failure mechanisms in karst and man-made underground caves in Southern Italy: Geomorphology, v. 134, no. 1–2, p. 132–143. doi:10.1016/j.geomorph.2011.06.008.

Pepe, P., Pentimone, N., Garziano, G., Martimucci, V., and Parise, M., 2013, Lessons learned from occurrence of sinkholes related to man-made cavities in a town of southern Italy, *in* Land, L., Doctor, D.H., and Stephenson, J.B., eds., Proceedings of the 13th Multidisciplinary Conference on Sinkholes and the Engineering and Environmental Impacts of Karst, Carlsbad (New Mexico, USA), 6–10 May 2013, Carsbad, National Cave and Karst Research Institute, p. 393–401.

Polák, M., Plašienka, D., Kohút, M., Putiš, M., Bezák, V., Filo, I., Olšavský, M., Havrila, M., Buček, S., Maglay, J., Elečko, M., Fordinál, K., Nagy, A., Hraško, Ľ., Németh, Z., Ivanička, J., and Broska, I., 2011, Geologická mapa regiónu Malých Karpát v M 1:50 000 (Geological map of the Male Karpaty Mts. Region, 1:50 000), Bratislava, MŽP SR, Štátny geologický ústav Dionýza Štúra.

Putiška, R., Dostál, I., Mojzeš, A., Gajdoš, V., Rozimant, K., and Vojtko, R., 2012a, The resistivity image of the Muráň fault zone (Central Western Carpathians) obtained by electrical resistivity tomography: Geologica Carpathica, v. 63, no. 3, p. 233–239. doi:10.2478/v10096-012-0017-3.

Putiška, R., Nikolaj, M., Dostál, I., and Kušnirák, D., 2012b, Determination of cavities using electrical resistivity tomography: Contributions to Geophysics and Geodesy, v. 42, no. 2, p. 201–211.

Schaad, W., 1995, Die Entstehung von Rauhwacken durch die Verkarstung von Gips: Eclogae Geologicae Helvetiae, v. 88, p. 59–90.

Waltham, T., Bell, F.G., and Culshaw, M.G., 2005, Sinkholes and Subsidence: Karst and Cavernous Rocks in Engineering and Construction. Chichester, UK, Praxis, 382 p.

White, W.B., 1990, Surface and near-surface karst landforms, *in* Higgins, C.G., and Coates, D.R., eds., Groundwater Geomorphology: The Role of Subsurface Water in Earth-Surface Processes and Landforms: Geological Society of America Special Paper 252, p. 157–175.

Zhou, W., Beck, B.F., and Adams, A.L., 2002, Effective electrode array in mapping karst hazards in electrical resistivity tomography: Environmental Geology, v. 42, p. 922–928. doi:10.1007/s00254-002-0594-z.

A. Kitamura, C. Tamaki, Y. Miyairi, Y. Yokoyama, and H. Mori – Possible cavern-forming activity at millennial time scales and its impact on variations in submarine cave environments and habitat availability, Okinawa, Japan. *Journal of Cave and Karst Studies,* v. 76, no. 3, p. 164–172. DOI: 10.4311/2013PA0109

POSSIBLE CAVERN-FORMING ACTIVITY AT MILLENNIAL TIME SCALES AND ITS IMPACT ON VARIATIONS IN SUBMARINE CAVE ENVIRONMENTS AND HABITAT AVAILABILITY, OKINAWA, JAPAN

Akihisa Kitamura[1*], Chikako Tamaki[1], Yosuke Miyairi[2], Yusuke Yokoyama[2], and Hideki Mori[3]

Abstract: We examined the spatial distributions and ^{14}C ages of sessile marine organisms in the submarine cave Ginama at Okinawa, Japan. The cave is the northernmost and only known submarine cave with an air chamber in the northwestern Pacific region. The upper limit of living individuals of the coralline sponges *Acanthocaetetes wellsi* and the bivalve *Pycnodonte taniguchii* in the cave is located at a depth of approximately 10 m relative to the surface of the pool in the cave. Low temperatures and low salinities prevent these organisms from colonizing water depths shallower than 10 m. On the other hand, the upper limit of fossil individuals, dated between 5117 and 387 cal yr BP, is at a depth of 2.5 m, implying that at present the influence of fresh water on the cave pool is stronger than it has been at other times in the past 5000 years. This increase in the flux of fresh water may be explained by continuous cavern-forming activities such as dissolution.

Introduction

A number of workers have recently used archival materials from submarine caves to reconstruct environmental changes during the late Quaternary (Antonioli et al., 2001; Kitamura et al., 2007, Yamamoto et al., 2008, 2009a). For example, oxygen-isotopic compositions of coralline sponges and micro-bivalves from submarine caves have been studied as proxies for palaeotemperature (Böhm et al., 2000; Haase-Schramm et al., 2003; Yamamoto et al., 2008, 2009b, 2010; Kitamura et al., 2013). In addition, the history of sea level changes has been examined using both speleothems and changes in faunal assemblages preserved in cave sediments (Dorale et al., 2010; Tuccimei et al., 2010; van Hengstum and Scott, 2011, 2012, van Hengstum et al., 2011).

However, few studies have examined temporal changes in faunal communities in submarine caves. In Mediterranean submarine caves, Chevaldonné and Lejeusne (2003) documented that populations of cold stenothermal species of mysids (Crustacea) were replaced by congeners of warmer affinities during a period of regional warming in the summers of 1997 and 1999. Parravicini et al. (2010) examined changes in sessile communities in a Mediterranean submarine cave using photographs taken in 1986 and 2004, revealing that massive numbers of organisms experienced high rates of mortality due to thermal anomalies during the summer heat waves of 1999 and 2003 and that these groups were replaced by encrusting organisms.

The northward-flowing tropical Kuroshio Current allows coral reefs to form in the Ryukyu Islands of southwestern Japan, northwestern Pacific (Fig. 1a). The islands extend from Tane-ga Island (30°44′N, 131°00′E) in the northeast to Yonaguni Island (24°27′N, 123°00′E) in the southwest. Many submarine limestone caves occur on the islands (Hayami and Kase, 1993). However, previous studies of changes in the communities of submarines caves have only considered millennial-scale variations in the species compositions of bivalves (Kitamura et al., 2007; Yamamoto et al., 2009a) and algal symbiont-bearing large benthic foraminifers (Omori et al., 2010) in Daidokutsu submarine cave (water depth, 29 m) at Ie Island, Okinawa (Fig. 1a). In both studies, the species living in the innermost areas of the cave were seen to have become increasingly dominant over the past 7000 years, while those living near the cave entrances have declined in abundance. The studies concluded that the changes were caused by a decline in food supply and light intensity in the cave associated with the filling of cavities within the reef during at least the past 6500 years. However, temporal changes in the communities of sessile organisms in submarine caves have yet to be examined in the northwestern Pacific.

This study examined millennial-scale variations in the compositions of sessile marine faunal communities in the submarine cave Ginama at Okinawa, Japan (Fig. 1b–d). The cave is unique in being the northernmost and only known submarine cave with an air chamber in the northwestern Pacific region.

Study Area

The submarine cave Ginama occurs in Triassic limestone (Ishibashi, 1974) on the northernmost coast of Okinawa Island (Fig. 1b). The coastline is characterized

[1] Institute of Geosciences, Shizuoka University, Shizuoka, 422-8529, Japan
[2] Atmosphere and Ocean Research Institute, University of Tokyo, Chiba, 277-8564, Japan
[3] Division of Technical Service, Shizuoka University, Shizuoka, 422-8529, Japan
* Corresponding Author: seakita@ipc.shizuoka.ac.jp

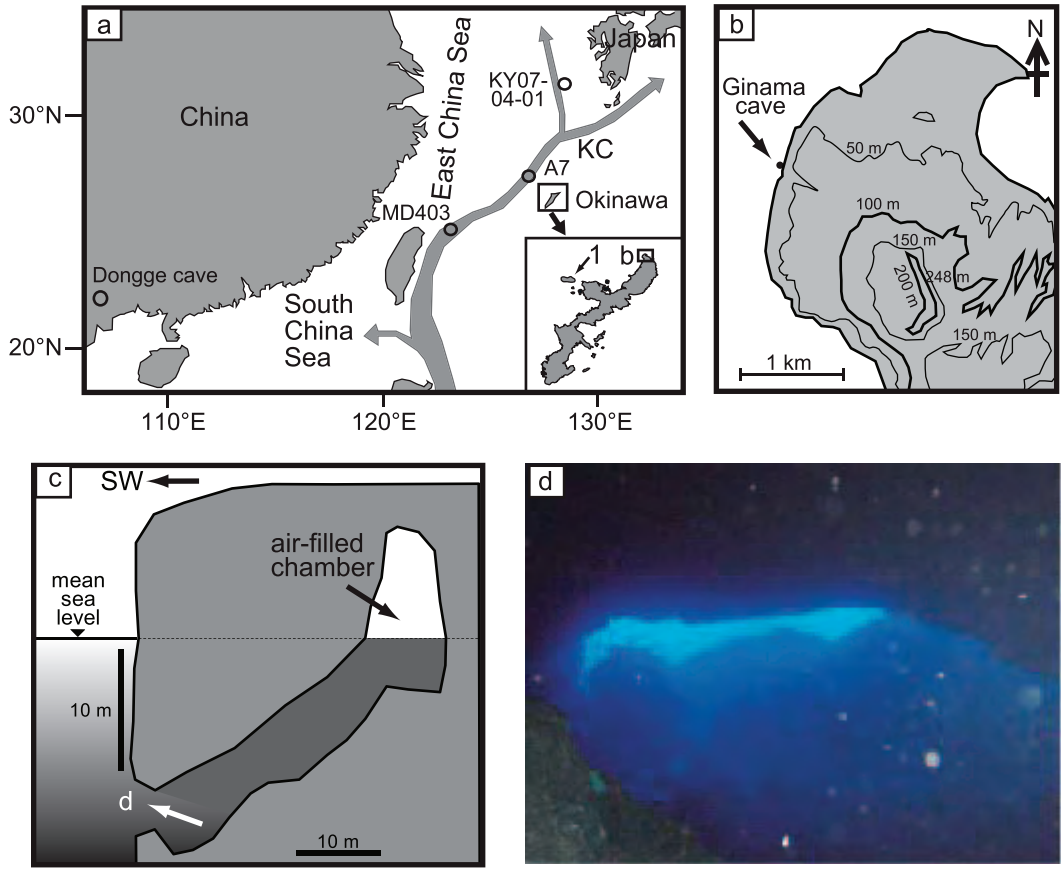

Figure 1. (a) Location map of Okinawa, Japan, showing the locations of drill cores A7 (Sun et al., 2005; Xiang et al., 2007), MD403 (Lin et al., 2006), KY07-04-01 (Kubota et al., 2010), and Dongge Cave (Wang et al., 2005); KC: Kuroshio Current; inset, area of part (b) and 1: Daidokutsu Cave off Ie Island. (b) Location map of submarine cave Ginama on the northern tip of Okinawa. (c) Simplified cross-section of the cave. Note vertical exaggeration. The white arrow shows the direction of the view in (d). (d) Photograph of the cave entrance, looking outward from inside the cave.

by sea cliffs with a height of approximately 10 m. The entrance to the cave, which is approximately 15-m below sea level, is 5 m high and 10 m wide. The cave consists of a narrow 40-m long upward-sloping gallery approximately 2 m high and 2 m wide and a dark, inner air-filled chamber with a height of 15 m (Fig. 1c). Many stalagmites are present both above and below the water surface in the inner chamber.

No emergent coastal landforms are present in the area, suggesting no net uplift of the area during the Holocene. The subsidence rate of the study area is currently 0.04 mm y^{-1}, based on geographic records from 1979 to 2006 (Geographical Survey Institute, 2007). Hongo and Kayanne (2010) reconstructed the Holocene sea level curve based on coral reefs of Ishigaki Island, Ryukyu Islands, which is located approximately 500 km southwest of the present study area. Based on the reconstruction, the entrance to Ginama Cave is thought to have become submerged at approximately 8000 years BP. To the best of our knowledge, no researches have been conducted on local groundwater, and no water wells are present in the area.

Methods

Water temperature and salinity were measured outside Ginama Cave close to the sea surface and in the pool below the chamber at 1 m intervals from the surface of the pool to a depth of 12 m; all measurements were obtained on 10 July 2012. We carefully observed and recorded all mega-fossils of sessile organisms on the rock wall of the cave pool at depths shallower than 10 m on 12–14 October 2011 and again on 10–11 July 2012, at which time we collected fossil shells of three individuals of the coralline sponge *Acanthocaetetes wellsi* and ten individuals of the bivalve *Pycnodonte taniguchii*. Both species are sessile organisms that live in submarine cave or cryptic habitats (Jackson et al., 1971; Jackson and Winston, 1982; Hayami and Kase, 1992). The bivalve *P. taniguchii* attaches to hard substrates with a thickened left valve (Hayami and Kase, 1992). The shells of both *A. wellsi* and *P. taniguchii* are composed of 100% calcite (Hayami and Kase, 1992; Reitner and Gautret, 1996). Many sessile micro-bivalves, most of which are less than 5 mm in length, such as *Cosa*

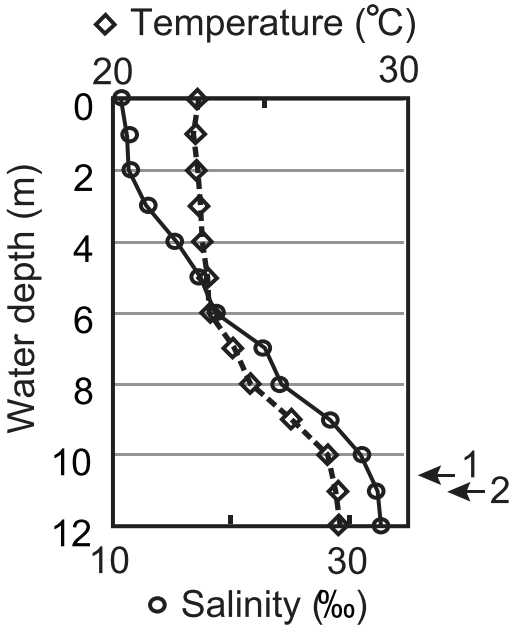

Figure 2. Water temperature and salinity in Ginama Cave, showing the water depth of the upper limit of living individuals of the bivalve *Pycnodonte taniguchii* (1) and of the coralline sponges *Acanthocaetetes wellsi* (2).

waikikia, *Cosa kinjoi*, and *Parvamussium crypticum* are present in the submarine caves of Okinawa (Hayami and Kase, 1992). However, because these species attach to rock surfaces by means of a byssus, the shells drop off immediately after death. In this study, we did not investigate the sessile micro-bivalve species.

Collected fossil specimens were cut along the axis of maximum growth using a low-speed saw. The specimens were checked for diagenetic alteration using thin-section observations with an optical microscope. We determined radiocarbon ages of all thirteen specimens of *A. wellsi* and *P. taniguchii*. The samples were graphitized, and the target graphites were analyzed using accelerator mass spectrometry at the University of Tokyo, Japan. The results were corrected using a reservoir age of 400 years, and the ages were transformed to a calendar timescale using the program OxCal4.1 (Bronk Ramsey 2009), based on comparisons with Marine 13 data (Reimer et al. 2013), after applying a ΔR value for the Okinawa region of 29 ± 18 years (Yoneda et al., 2007).

RESULTS

Water temperatures and salinities in the pool increased with water depth (Fig. 2). At a depth of 12 m, the values of both parameters were nearly equal to those of sea-surface water outside the cave.

A living individual of *Acanthocaetetes wellsi* was found at a water depth of 11.3 m. We also found a young individual *Pycnodonte taniguchii* at a depth of 10.5 m. Three fossil individuals of *A. wellsi* and ten fossil individuals of *P. taniguchii* (left valves only) were distributed at depths of up to 2.5 m within the brackish-water lens (Figs. 3 and 4). Thin-section observations show that these specimens were unaffected by diagenetic alteration, al-

Figure 3. Photograph of a fossil of the bivalve *Pycnodonte taniguchii* (sample Ginama 9) at a water depth of 6.5 m.

Figure 4. Photographs of specimens. 1–3: *Acanthocaetetes wellsi* (sample nos. Ginama 4-3, 6-1, 5-2). 4–13: *Pycnodonte taniguchii* 4-13; (samples Ginama 3, 8, 9, 10, 7-1, 7-2, 7-3, 19-1, 19-2, 19-3).

though a partially calcified filling can be observed on the surface layer of *A. wellsi* (Fig. 5a); this portion was excluded from ^{14}C dating. The radiocarbon ages obtained for the fossil specimens are listed in Table 1 and plotted in Figure 6. All specimens of *A. wellsi* and seven individuals of *P. taniguchii* fall into an older age group, from 5117 ± 243 (2σ) to 3105 ± 232 (2σ) cal years BP. Three individuals of *P. taniguchii* fall into a younger age group, from 566 ± 75 (2σ) to 387 ± 96 (2σ) cal years BP (Fig. 6).

Discussion

The coralline sponge *Acanthocaetetes wellsi* is a component of cryptic sessile communities on modern Indo-Pacific reefs (Reitner and Gautret, 1996). According to Grottoli (2006), the habitats of *A. wellsi* are unaffected by runoff from land. This species has also been collected in submarine caves on the southernmost coast of the Okinawa mainland and on Kume Island, Okinawa (Ohmori et al.,

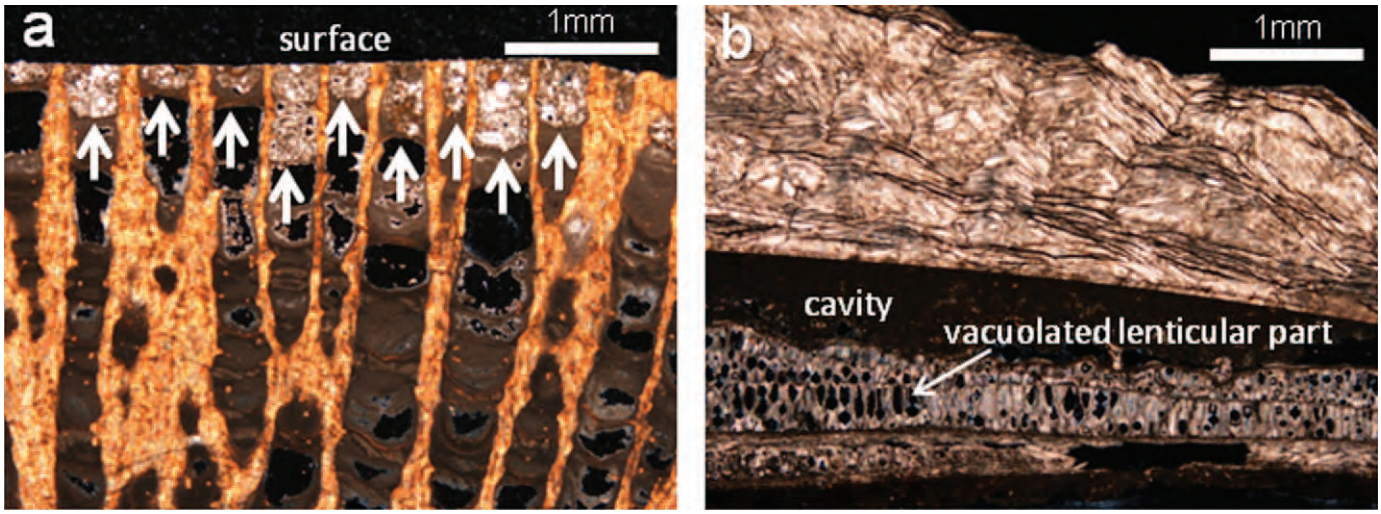

Figure 5. Thin-section photomicrographs (cross-polarized light). (a) Specimen of coralline sponge *Acanthocaetetes wellsi* (sample Ginama 4-3; age, 4623 ± 206 cal years BP); arrows show calcified fillings. (b) Specimen of the bivalve *Pycnodonte taniguchii* (sample Ginama 3; age, 5064 ± 221 cal years BP).

2008; Higa et al., 2010). None of the *A. wellsi* sites are reported to be influenced by runoff from land. We therefore think that *A. wellsi* thrives in conditions of normal salinity. To our knowledge, the Ginama Cave is the northernmost cave in which *A. wellsi* has been found.

Live individuals of the bivalve *P. taniguchii* have been found at many cavernicolous sites of the following islands in the western Pacific and eastern regions of the Indian Ocean: Ryukyu (Miyako, Okinawa, and Yonaguni islands), Bonin, Palau, Philippines (Luzon, Cebu, Bohol islands), Malaysia, Vanuatu, Fiji, Tonga and Thailand (near Phuket) (Hayami and Kase, 1992, 1999). According to Hayami and Kase (1992, 1999), individuals of *P. taniguchii* always grow under conditions of normal salinity and temperature. Ginama Cave and Daidokutsu Cave, located approximately 45 km southwest of the study area off Ie Island (Fig. 1a), are among the northernmost sites at which *P. taniguchii* has been found. According to Yamamoto et al. (2010), seasonal changes in water temperature in Daidokutsu Cave range from 29 °C in August–September to 21 °C in February. Data from the Japan Oceanographic Data Center (2007) show that, at water depths of 20 m, similar to those of the study area, water temperatures range from 28.2 ± 0.6 °C in September to 22.0 ± 0.9 °C in February, which indicates that *P. taniguchii* can survive at temperature of 21 °C during the winter season. No studies have reported on the lower limits of dissolve oxygen for the survival of either *A. wellsi* or *P. taniguchii*.

As noted above, living individuals of *A. wellsi* and *P. taniguchii* were found in Ginama Cave at depths of 11.3 m and 10.5 m, respectively. At depths shallower than 10 m, both water temperature and salinity decrease upward. It is therefore likely that relatively low temperatures and

Table 1. Results of ^{14}C dating; uncertainties are 2σ.

Sample Number	Sample	Depth, m	Conventional ^{14}C Age, BP	Calendar Age Ranges, cal BP
Ginama 4-3	*Acanthocaetetes wellsi*	2.5	4491 ± 83	4623 ± 206
Ginama 6-1	*Acanthocaetetes wellsi*	4.2	4863 ± 85	5117 ± 243
Ginama 5-2	*Acanthocaetetes wellsi*	5.1	3454 ± 83	3279 ± 222
Ginama 3	*Pycnodonte taniguchii*	4.0	4814 ± 86	5064 ± 221
Ginama 8	*Pycnodonte taniguchii*	5.5	3966 ± 85	3932 ± 247
Ginama 9	*Pycnodonte taniguchii*	6.5	4356 ± 86	4474 ± 271
Ginama 10	*Pycnodonte taniguchii*	6.5	4304 ± 82	4394 ± 251
Ginama 7-1	*Pycnodonte taniguchii*	8.3	4622 ± 88	4806 ± 262
Ginama 7-2	*Pycnodonte taniguchii*	8.3	3313 ± 86	3105 ± 232
Ginama 7-3	*Pycnodonte taniguchii*	8.3	4591 ± 158	4779 ± 439
Ginama 19-1	*Pycnodonte taniguchii*	9.7	784 ± 47	387 ± 96
Ginama 19-2	*Pycnodonte taniguchii*	9.7	996 ± 46	566 ± 75
Ginama 19-3	*Pycnodonte taniguchii*	9.7	896 ± 43	489 ± 86

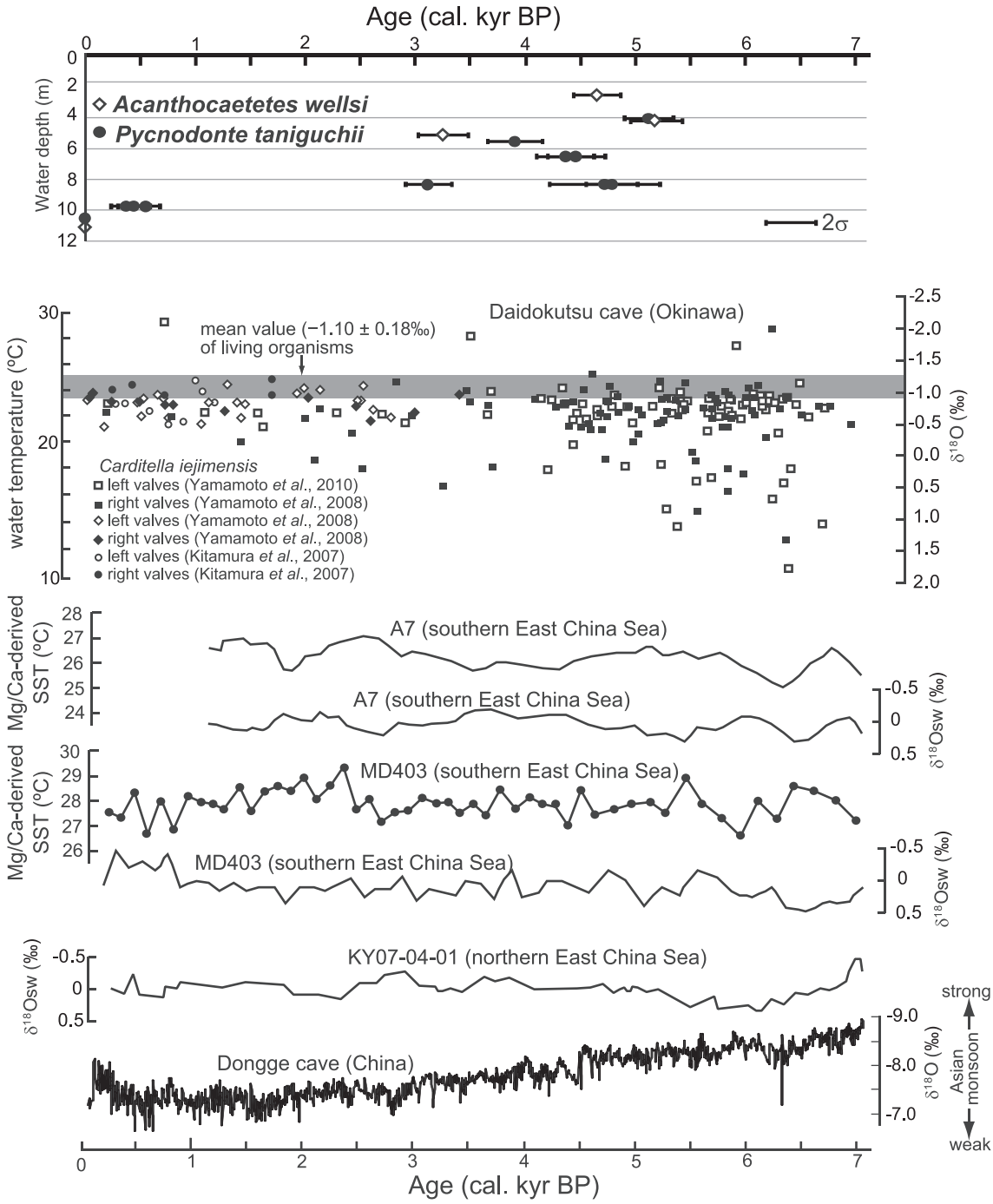

Figure 6. Top: Age data for fossils from this paper. Middle: $\delta^{18}O$ and corresponding temperature values of *Carditella iejimensis* shells from cored samples (Kitamura et al., 2013). Bottom: On common scale Mg/Ca-derived SSTs and $\delta^{18}O_{sw}$ records from cores A7 (Sun et al., 2005), MD403 (Lin et al., 2006), and KY07-04-01 (Kubota et al., 2010) and stalagmite $\delta^{18}O$ records from Dongge Cave, southeast China (Wang et al., 2005). The locations of all sites are shown in Figure 1.

salinities prevented these sessile marine organisms from colonizing surfaces at depths shallower than 10 m. On the other hand, ^{14}C ages obtained in the present study show that fossil specimens of *A. wellsi* and *P. taniguchii* are present at depths shallower than 10 m. According to Hongo and Kayanne (2010), a mid-Holocene highstand occurred at approximately 5000 cal. years BP, at a level of approximately 3 ± 2.5 m above present mean sea level, based on vertical distributions of corals on Ishigaki Island, Okinawa. At approximately 5000 cal. years BP, *A. wellsi* (sample no. Ginama 6-1) and *P. taniguchii* (sample no. Ginama 3) were distributed at depths of 4.0 and 4.2 m,

respectively (Table 1). Assuming that the rate of subsidence during the past 5000 years equals the present day surveyed rate of 0.04 mm/year, the total subsidence during this period is estimated to be 0.2 m. Based on this subsidence rate and sea level at approximately 5000 cal. years BP (3 ± 2.5 m above present mean sea level), the estimated depths of *A. wellsi* and *P. taniguchii* were from 4.3 to 9.5 m, and from 4.5 to 9.7 m, respectively. From 566 ± 75 to 387 ± 96 cal years BP, the upper limit of survival of individuals of *P. taniguchii* (depth, 9.7 m; sample nos Ginama 19-1, -2, and -3) was shallower than that of presently living individuals. We therefore suggest that the influence of fresh water in the Ginama Cave pool at the present day is the strongest it has been in the past 5000 years, although we note that data are missing for the period 3105–566 cal years BP. In addition, changes in the flux of fresh water into the cave cannot be explained by relative sea level changes.

The rainy season in the study area occurs during the summer monsoon. Precisely dated stalagmite oxygen-isotope records from China reveal that a Holocene weakening of the summer monsoon since 7000 years BP corresponds to an orbitally induced reduction in summer-time solar insolation in the Northern Hemisphere (e.g., Dykoski et al., 2005; Wang et al., 2005) (Fig. 2). Such a weakening of the summer monsoon should cause a decrease in the flux of fresh water into the cave.

Many studies have examined Holocene oceanographic changes in the East China Sea, based on geochemical analyses of the planktonic foraminifera *Globigerinoides ruber*, which remains at water depths of 2 to 50 m during its life cycle (e.g., Fairbanks et al., 1982; Hemleben et al., 1989; Lin et al., 2004) and were recovered from deep-sea sedimentary cores (Jian et al., 2000; Ijiri et al., 2005; Sun et al., 2005; Lin et al., 2006; Kubota et al., 2010). Sun et al. (2005), Lin et al. (2006), and Kubota et al. (2010) reported no changes in sea-surface temperatures or sea-surface salinities in the East China Sea during the past 7000 years. Jian et al. (2000) proposed that a decrease in temperatures during the period 4600–2700 cal. years BP was related to an intensification of the winter monsoon, although they reported no changes in temperatures or salinities during the past 2700 years.

Yamamoto et al. (2010) measured $\delta^{18}O$ values of fossils of the micro-bivalve *Carditella iejimensis*, which have height and length <3.5 mm and dwell on the sediment surface (Hayami and Kase, 1993), from core sediments collected from Daidokutsu Cave, Ie Island, Okinawa. The results also show no clear long-term trends in the $\delta^{18}O$ values of bivalves during the past 7000 years. More recently, Kitamura et al. (2013) analyzed $\delta^{18}O$ values of 50 living *C. iejimensis* specimens from Daidokutsu Cave (Fig. 6) and concluded that the $\delta^{18}O$ values represent the mean annual temperature and $\delta^{18}O$ value of seawater. In summary, Kitamura et al. (2013) confirmed that no changes have occurred in either sea-surface temperatures or salinities during the past 7000 years. These results are consistent with the findings of previous studies in the East China Sea (Jian et al., 2000; Ijiri et al., 2005; Sun et al., 2005; Lin et al., 2006; Kubota et al., 2010).

Both oceanographic data and stalagmite oxygen isotope records show that a gradual weakening of the summer monsoon has not been a significant influence on sea-surface temperatures and salinities in the area of Okinawa over the past 7000 years. Thus, the increased flux of fresh water to Ginama Cave cannot be explained by climate variables. Alternatively, we suggest that the development of crevices and passages within the cave caused the increase in the flux of fresh water over time. To test this interpretation, a further study should measure growth rates of stalagmites in the air chamber within the cave.

Our hypothesis is opposite to that proposed for nearby Daidokutsu Cave, which is that continuous filling of cavities within the reef foundation of the cave has influenced submarine cave communities (Yamamoto et al., 2009a; Omori et al., 2010). The difference between the two caves, that is, the possible development of cavities versus filling of cavities, indicates variability of millennia-scale cavern forming processes in submarine caves caused by difference in their vertical position relative to sea level.

ACKNOWLEDGEMENTS

We greatly appreciate the assistance of Koushin Yasumura and Fumio Tamamura in the collection of samples. We thank two anonymous reviewers, whose comments and suggestions improved the original manuscript. We thank A. Stallard for improving the English in the manuscript. This study was funded by the Mitsubishi Foundation.

REFERENCES

Antonioli, F., Silenzi, S., and Frisia, S., 2001, Tyrrhenian Holocene palaeoclimate trends from spelean serpulids: Quaternary Science Reviews, v. 20, p. 1661–1670. doi:10.1016/S0277-3791(01)00012-9.

Böhm, F., Joachimski, M.M., Dullo, W-C., Eisenhauer, A., Lehnert, H., Reitner, J., and Wörheide, G., 2000, Oxygen isotope fractionation in marine aragonite of coralline sponges: Geochimica et Cosmochimica Acta, v. 64, p. 1695–1703. doi:10.1016/S0016-7037(99)00408-1.

Bronk Ramsey, C., 2009, Bayesian analysis of radiocarbon dates: Radiocarbon, v. 51, p. 337–360.

Chevaldonné, P., and Lejeusne, C., 2003, Regional warming-induced species shift in north-west Mediterranean marine caves: Ecology Letters, v. 6, p. 371–379. doi:10.1046/j.1461-0248.2003.00439.x.

Dorale, J.A., Onac, B.P., Fornós, J.J., Ginés, J., Ginés, A., Tuccimei, P., and Peatel, D.W., 2010, Sea-level highstand 81,000 years ago in Mallorca: Science, v. 327, p. 860–863. doi:10.1126/science.1181725.

Dykoski, C.A., Edwards, R.L., Cheng, Hai, Yuan, Daoxian, Cai, Yanjun, Zhang, Meiliang, Lin, Yushi, Qing, Jiaming, An, Zhisheng, and Revenaugh, J., 2005, A high-resolution, absolute-dated Holocene and deglacial Asian monsoon record from Dongge Cave, China: Earth and Planetary Science Letters, v. 233, p. 71–86. doi:10.1016/j.epsl.2005.01.036.

Fairbanks, R.C., Sverdlove, M., Free, R., Wiebe, P.H., and Bé, A.W.H., 1982, Vertical distribution and isotopic fractionation of living planktonic foraminifer from the Panama Basin: *Nature*, v. 298, p. 841–844. doi:10.1038/298841a0.

Geographical Survey Institute, 2007, Crustal Movements in the Kyushu and Okinawa Districts: Report of the Coordinating Committee for Earthquake Prediction, Japan, v. 78, p. 561–567 (in Japanese).

Grottoli, A.G., 2006, Monthly resolved stable oxygen isotope record in a Palauan sclerosponge *Acanthocaetetes wellsi* for the period of 1977–2001, *in* Suzuki, Y., Nakamori, T., Hidaka, M., Kayanne, H., Casareto, B.E., Nadaoka, K., Yamano, H., and Tsuchiya, M., eds., eds., Proceedings of the 10th International Coral Reef Symposium: Tokyo, Japanese Coral Reef Society, p. 572–579.

Haase-Schramm, A., Böhm, F., Eisenhauer, A., Dullo, W-C., Joachimski, M.M., Hansen, B., and Reitner, J., 2003, Sr/Ca ratios and oxygen isotopes from sclerosponges: Temperature history of the Caribbean mixed layer and thermocline during the Little Ice Age: Paleoceanography, v. 18, no. 3, doi:10.1029/2002PA000830.

Hayami, I., and Kase, T., 1992, A new cryptic species of Pycnodonte from Ryukyu Islands: A living fossil oyster: Transactions and Proceedings of the Palaeontological Society of Japan, New Series, No. 165, p. 1070–1089.

Hayami, I., and Kase, T., 1993, Submarine cave bivalvia from the Ryukyu Islands: systematics and evolutionary significance: The University Museum, The University of Tokyo, Bulletin 35, 133 p.

Hayami, I., and Kase, T., 1999, Geographic Distribution of *Pycnodonte taniguchii*: Newsletter of the Malacological Society of Japan, v. 30, p. 5–7 (in Japanese with English Abstract).

Hemleben, C., Spindler, M., and Anderson, O.R., 1989, Modern Planktonic Foraminifera: New York, Springer, 363 p.

Higa, K., Fukuyama, Y., Sekiya, M., West, R.R., Nagai, K., and Sugiyama, T., 2010, Habitat of a living fossil, *Acanthocaetetes* (Class Demospongiae), along the Komesu coast in the southern part of Okinawa Island: Fukuoka University Science Reports, v. 40, p. 233–243 (in Japanese).

Hongo, C., and Kayanne, H., 2010, Holocene sea-level record from corals: reliability of paleodepth indicators at Ishigaki Island, Ryukyu Islands, Japan: Palaeogeography, Palaeoclimatology, Palaeoecology, v. 287, p. 143–151. doi:10.1016/j.palaeo.2010.01.033.

Ijiri, A., Wang, Luejiang, Oba, T., Kawahata, H., Huang, Chen-Yue, and Huang, Chi-Yue, 2005, Paleoenvironmental changes in the northern area of the East China Sea during the past 42,000 years: Palaeogeography, Palaeoclimatology, Palaeoecology, v. 219, p. 239–261. doi:10.1016/j.palaeo.2004.12.028.

Ishibashi, T., 1974, On the Triassic Formation at Hedo-misaki in Okinawa-jima: The Journal of the Geological Society of Japan, v. 80, p. 329–330. (in Japanese).

Jackson, J.B.C., Goreau, T.F., and Hartman, W.D., 1971, Recent brachiopod-coralline sponge communities and their paleoecological significance: Science, v. 173, p. 623–625. doi:10.1126/science.173.3997.623

Jackson, J.B.C., and Winston, J.E., 1982, Ecology of cryptic coral reef communities. I. Distribution and abundance of major groups of encrusting organisms: Journal of Experimental Marine Biology and Ecology, v. 57, p. 135–147. doi:10.1016/0022-0981(82)90188-5.

Japan Oceanographic Data Center, Online Data, 2007, http://jdoss1.jodc.go.jp/cgi-bin/1997/bts.jp. [Accessed October 10, 2013]

Jian, Zhimin, Wang, Pinxian, Saito, Y., Wang, Jiliang, Pflaumann, U., Oba, T., and Cheng, Xinrong, 2000, Holocene variability of the Kuroshio Current in the Okinawa Trough, northwestern Pacific Ocean: Earth and Planetary Science Letters, v. 184, p. 305–319. doi:10.1016/S0012-821X(00)00321-6.

Kitamura, A., Kobayashi, K., Tamaki, C., Yamamoto, N., Irino, T., Miyairi, Y., and Yokoyama, Y., 2013, Evidence of recent warming in the Okinawa region, subtropical northwestern Pacific, from an oxygen isotope record of a cave-dwelling marine micro-bivalve: Paleontological Research, v. 17, p. 58–68. doi:10.2517/1342-8144-17.1.58

Kitamura, A., Yamamoto, N., Kase, T., Ohashi, S., Hiramoto, M., Fukusawa, H., Watanabe, T., Irino, T., Kojitani, H., Shimamura, M., and Kawakami, I., 2007, Potential of submarine-cave sediments and oxygen isotope composition of cavernicolous micro-bivalve as a late Holocene paleoenvironmental record: Global and Planetary Change, v. 55, p. 301–316. doi:10.1016/j.gloplacha.2006.09.002.

Kubota, Y., Kimoto, K., Tada, R., Oda, H., Yokoyama, Y., and Matsuzaki, H., 2010, Variations of East Asian summer monsoon since the last deglaciation based on Mg/Ca and oxygen isotope of planktic foraminifera in the northern East China Sea: Paleoceanography, v. 25, PA4205, doi:10.1029/2009PA001891.

Lin, Hui-Ling., Wang, Wei-Chial, and Hung, Gwo-Wei, 2004, Seasonal variation of planktonic foraminiferal isotopic composition from sediment traps in the South China Sea: Marine Micropaleontology, v. 53, p. 447–460. doi:10.1016/j.marmicro.2004.08.004.

Lin, Yu-Shih, Wei, Kuo-Yen, Lin, In-Tian, Yu, Psi-Sen, Chiang, Hong-Wei, Chen, Chen-Yin., Shen, Chaun-Chou, Mii, Homg-Sheng, and Chen, Yue-Gau., 2006, The Holocene *Pulleniatina* Minimum Event revisited: geochemical and faunal evidence from the Okinawa Trough and upper reaches of the Kuroshio current: Marine Micropaleontology, v. 59, p. 153–170. doi:10.1016/j.marmicro.2006.02.003.

Ohmori, K., Watanabe, T., Shirai, K., and Kan, H., 2008, Skeletal microstructures and the variety of trace elements in Pacific sclerosponges: Chikyu Monthly, v. 30, p. 322–328 (in Japanese).

Omori, A., Kitamura, A., Fujita, K., Honda, K., and Yamamoto, N., 2010, Reconstruction of light conditions within a submarine cave during the past 7,000 years based on the temporal and spatial distribution of algal symbiont-bearing large benthic foraminifers: Palaeogeography, Palaeoclimatology, Palaeoecology, v. 292, p. 443–452. doi:10.1016/j.palaeo.2010.04.004.

Parravicini, V., Guidetti, P., Morri, C., Montefalcone, M., Donato, M., and Bianchia, C.N., 2010, Consequences of sea water temperature anomalies on a Mediterranean submarine cave ecosystem: Estuarine, Coastal and Shelf Science, v. 86, p. 276–282. doi:10.1016/j.ecss.2009.11.004.

Reimer, P.J., Bard, E., Bayliss, A., Beck, J.W., Blackwell, P.G., Bronk Ramsey, C., Buck, C.E., Cheng, Hai, Edwards, R.L., Friedrich, M., Grootes, P.M., Guilderson, T.P., Haflidason, H., Hajdas, I., Hatté, C., Heaton, T.J., Hoffmann, D.L., Hogg, A.G., Hughen, K.A., Kaiser, K.F., Kromer, B., Manning, S.W., Niu, M., Reimer, R.W., Richards, D.A., Scott, E.M., Southon, J.R., Staff, R.A., Turney, C.S.M., and van der Plicht, J., 2013, IntCal13 and Marine13 radiocarbon age calibration curves, 0–50,000 years cal BP: Radiocarbon, v. 55, no. 4, p. 1869–1887. doi:10.2458/azu_js_rc.55.16947.

Reitner, J., and Gautret, P.P., 1996, Skeletal formation in the modern but ultraconservative chaeteid sponge *Spirastrella* (*Acanthochaetetes*) *wellsi* (Demospongiae, Porifera): Facies, v. 34, p. 193–207. doi:10.1007/BF02546164.

Sun, Youbin, Oppo, D.W., Xiang, Rong, Liu, Weiguo, and Gao, Shu, 2005, Last deglaciation in the Okinawa Trough: subtropical northwest Pacific link to Northern Hemisphere and tropical climate: Paleoceanography, v. 20, PA4005, doi:10.1029/2004PA001061.

Tuccimei, P., Soligo, M., Ginés, J., Ginés, A., Fornós, J., Kramers, J., and Villa, I.G., 2010, Constraining Holocene sea levels using U/Th ages of phreatic overgrowths on speleothems from coastal caves in Mallorca (Western Mediterranean): Earth Surface Processes and Landforms, v. 35, p. 782–790. doi:10.1002/esp.1955.

van Hengstum, P.J., and Scott, D.B., 2011, Ecology of foraminifera and habitat variability in an underwater cave: distinguishing anchialine versus submarine cave environments: Journal of Foraminiferal Research, v. 41, p. 201–229. doi:10.2113/gsjfr.41.3.201.

van Hengstum, P.J., and Scott, D.B., 2012, Sea-level rise and coastal circulation controlled Holocene groundwater development in Bermuda and caused a meteoric lens to collapse 1600 years ago: Marine Micropaleontology, v. 90–91, p. 29–43. doi:10.1016/j.marmicro.2012.02.007.

van Hengstum, P.J., Scott, D.B., Gröcke, D.R., and Charette, M.A., 2011, Sea level controls sedimentation and environments in coastal caves and sinkholes: Marine Geology, v. 286, p. 35–50. doi:10.1016/j.margeo.2011.05.004.

Wang, Yongjin, Cheng, Hai, Edwards, R.L., He, Yaoqi, Kong, Xinggong, An, Zhisheng, Wu, Jiangying, Kelly, M.J., Dykoski, C.A., and Li, Xiangdong, 2005, The Holocene Asian monsoon: links to solar changes and North Atlantic climate: Science, v. 308, p. 854–857. doi:10.1126/science.1106296.

Xiang, R., Sun, Y., Li, T., Oppo, D.W., Chen, M., and Zheng, F., 2007, Paleoenvironmental change in the middle Okinawa Trough since the last deglaciation: Evidence from the sedimentation rate and planktonic foraminiferal record. Palaeogeography, Palaeoclimatology, Palaeoecology 243, p. 378–393. doi:10.1016/j.palaeo.2006.08.016.

Yamamoto, N., Kitamura, A., Irino, T., Kase, T., and Ohashi, S., 2008, Reconstruction of paleotemperatures in Northwest Pacific over the past 3,000 years from $\delta^{18}O$ values of the micro-bivalvia *Carditella iejimensis* found in a submarine cave: Global and Planetary Change, v. 62, p. 97–106. doi:10.1016/j.gloplacha.2007.12.001.

Yamamoto, N., Kitamura, A., Irino, T., Kase, T., and Ohashi, S., 2010, Climatic and hydrologic variability in the East China Sea during the last 7,000 years based on oxygen isotope records of the submarine cavernicolous micro-bivalve *Carditella iejimensis*: Global and Planetary Change, v. 72, p. 131–140. doi:10.1016/j.gloplacha.2010.01.025.

Yamamoto, N., Kitamura, A., Ohmori, A., Morishima, Y., Toyofuku, T., and Ohashi, S., 2009a, Long-term changes in sediment type and cavernicolous bivalve assemblages in Daidokutsu submarine cave, Okinawa Islands: evidence from a new core extending over the past 7,000 years: Coral Reefs, v. 28, p. 967–976. doi:10.1007/s00338-009-0536-2.

Yamamoto, N., Sakai, S., and Kitamura, A., 2009b, Evaluation of the $\delta^{18}O$ value of the submarine cavernicolous micro-bivalve *Carditella iejimensis* as a proxy for palaeotemperature: Paleontological Research, v. 13, p. 279–284. doi:10.2517/1342-8144-13.3.279.

Yoneda, M., Uno, H., Shibata, Y., Suzuki, R., Kumamoto, Y., Yoshida, K., Sasaki, T., Suzuki, A., and Kawahata, H., 2007, Radiocarbon marine reservoir ages in the western pacific estimated by prebomb molluscan shells: Nuclear Instruments and Methods in Physics Research B: Beam Interactions with Materials and Atoms, v. 259, p. 432–437. doi:10.1016/j.nimb.2007.01.184.

S.K. Basumatary and S.K. Bera – Modern pollen record on bat guano deposit from Siju Cave and its implication to palaeoecological study in South Garo Hills of Meghalaya, India. *Journal of Cave and Karst Studies,* v. 76, no. 3, p. 173–183. DOI: 10.4311/2013PA0119

MODERN POLLEN RECORD ON BAT GUANO DEPOSIT FROM SIJU CAVE AND ITS IMPLICATION TO PALAEOECOLOGICAL STUDY IN SOUTH GARO HILLS OF MEGHALAYA, INDIA

SADHAN K. BASUMATARY* AND SAMIR K. BERA
Birbal Sahni Institute of Palaeobotany, Quaternary Palynology Division, 53, University Road, Lucknow-226007, Uttar Pradesh, India

Abstract: Meghalaya is well known for its rich tropical biodiversity and numerous natural caves. The Siju Cave of Meghalaya, also known as cave of the bat, is among the longest caves on the Indian subcontinent. The palynological study of fifty bat-guano samples from Siju Cave and of thirty surface soil and moss cushion from the area immediate surrounding the cave reflects the close similarity between the modern pollen and vegetation in the region in the two areas sampled. The resulting palynodata comprise mainly the native flora, dominated by riparian taxa like *Duabanga*, *Syzygium*, *Careya*, and *Ficus,* along with evergreen and deciduous elements in the region. The evergreen taxa *Mesua*, *Elaeocarpus*, and *Garcinia*, along with *Impatiens*, reflect the high precipitation in the region. The climate of the region and the vegetation are strongly influenced by the Simsang River, and the heavy rainfall results in the dominance of riparian taxa and other high-rainfall indicator taxa. The occurrence of pollen from *Nepenthes khasiana*, an endemic and endangered plant of Meghalaya, in bat guano is significant and may be due to its insectivorous and entomophilous nature. However, medicinal plants like *Swertia chirata*, *Cinchona*, and *Rauvolfia* are not encountered in the bat-guano sediments, despite their luxuriant growth around the cave, and these species could be avoided by the insects due to their alkaloid contain and bitter taste. The presence of highland taxa such as *Pinus*, *Abies*, *Picea*, and *Larix* in the bat guano deposit is significant and suggestive of high winds from higher altitudes, or the pollen may be introduced by the return of migratory Siberian birds during winter to the nearby Siju wildlife and bird sanctuary. The recovery of cerealia along with *Areca catechu* and *Citrus* pollen indicate the human activity in the region. The abundance of fungal remains, namely *Meliola*, *Glomus*, and Microthyriaceae along with degraded palynomorphs are suggestive of strong microbial activity under warm and humid conditions during sedimentation in the region. The main objective of this study is to identify the potential of bat guano for palaeoecological research and as supportive data for surface and sedimentary soil profiles in the South Garo Hills of Meghalaya. The palynodata from the bat guano of the Siju Cave provides a useful source for palaeoecological information for the South Garo Hills, where intensive natural and human-caused forest fires, heavy rainfall, and soil erosion occur every year and there is a relative scarcity of the lake, wetland, and swamp habitats that normally preserve pollen.

INTRODUCTION

The state of Meghalaya includes a significant portion of both Himalaya and Indo-Burma biodiversity hotspots (Mittermeier et al., 2005) and is globally known for Cherrapunjee, with the highest rainfall on earth and the endemic and endangered plant *Nepenthes khasiana* Hk. f., the symbolic plant of Meghalaya. The flora of Meghalaya is the richest in India and probably in the whole of Asia, with a close similarity to the flora of southeast Asia and southern China (Hooker, 1905). This region of the world is considered by botanists and geographers as one of the nuclear areas of early plant domestication (Vivilov, 1951; Sauer, 1952; Harris, 1972). The whole of the Garo Hills, especially the South Garo Hills, is also known as the ecological canvas of Meghalaya because of its unique biodiversity and numerous beautiful natural caves (Anonymous, 2006). The quantity and length of caves in Meghalaya far exceeds that of any other known karst region of India. Until recently only a few caves had been explored, but recent exploration has resulted in over 320 kilometers of cave passage mapped and over a thousand cave entrances documented in Meghalaya (Harries et al., 2008). As caves are natural open cavities in the earth, they function as natural sediment traps

* Corresponding author, sbasumatary2005@yahoo.co.in

(White, 2007). In caves with large bat populations, guano (bat excreta) is present in sufficient quantities to be classified as a clastic sediment and serves as a source of useful climatic records (Leroy and Simms, 2006; White, 2007). In general, there are mainly three mechanisms for the incorporation of pollen into bat guano: bats can consume large numbers of flying insects, may consume pollen themselves, and may fly through a pollen-laden environment so that pollen and other dust particles often adheres to their body (Pendleton et al., 1996). Pollen in fragments of bat skin and hair may be lost during grooming, and dust containing pollen may be brought into the cave and deposited onto guano by air currents (Coles and Gilbertson, 1994). Where there are large colonies of bats their excrement accumulates on the cave floor below (Maher, 2006).

Many palaeoecological-research studies have been carried out on palynology of cave sediments, including bat guano and coprolites from other taxa and surface soil in different part of the globe, such as in Romania (Pop and Ciobanu, 1950; Boscaiu and Lupsa, 1967a,b; Feurdean et al., 2011; Geanta et al., 2012), the United States (Sears and Roosma, 1961; Davis, 1990; Nieves-Rivera 2003; Maher, 2006; Batina and Reese, 2011), Switzerland (Groner, 2004), Austria (Kral, 1968; Draxler, 1972), the UK (Coles et al., 1989; McGarry and Caseldine, 2004), Spain (Carrión, 1992; Carrión et al., 1999, 2006; Navarro Camacho et al., 2000, 2001), Belgium (Bastin, 1978; Bastin et al., 1986), Nepal (Denniston, et al., 2000), China (Qin et al., 1999; Zhang et al., 2004), and other parts of Asia (Hunt and Rushworth, 2005). In India, no previous studies have addressed the use of bat guano in cave sediments for palaeoecological study. We have discovered the Siju Cave to be one of the best sites to study bat guano for palynological research in the South Garo Hills of Meghalaya. In the Garo Hills, intensive natural and human-caused forest fires every year burn several centimeters of soil in the region (Fig. 2F). In addition, other factors like the high rainfall and tremendous soil erosion, along with the hilly terrain, make difficult the proper investigation and interpretation of modern pollen and vegetation relationships in the Garo Hills. The relatively scarcity of lake, wetland, and swamps has limited attempts to recover sediment cores from the Garo Hills for palaeoecological research. Although there are some scattered small lakes like Napak Lake in the South Garo Hills, these are not suitable for proper coring for palynological study. Previously, only a few preliminary palynological studies have been carried out in Meghalaya (Gupta and Sharma, 1985; Basumatary and Bera, 2007, 2010, 2012, Basumatary et al., 2013). Considering these previous limits to pollen studies in the region, we initiated the present palynological study on bat guano in Siju Cave in the South Garo Hills. The main objective of the study, as the first to be undertaken as a new innovation in pollen studies in India, was to identify the potential of bat guano as a reliable source to document modern pollen and vegetation in relation to climate in the South Garo hills.

Physiography and Soil

The South Garo Hills of Meghalaya are a unique feature of physiography where the Tura and Arabella Ranges run parallel in an east-west direction. The Tura Range runs from Siju to Tura, and the Arabella Range is to the north of the Tura range and gradually increases in height, eventually joining the Tura, which starts in the West Garo Hills to the south. The Garo Hills of Meghalaya are drained by many rivers and streamlets. The soil of the region is generally red-loamy, but sometimes varies from clay to sandy loam, and is rich in organic carbon with high nitrogen-supplying potential but is deficient in phosphorus and potassium. The soil pH ranges from acidic (pH 5.0 to 6.0) to strongly acidic (pH 4.5 to 5.0) (Directorate of Agriculture, Meghalaya, 2012).

Climate

The climate of the region is controlled by south-west and north-eastern monsoons. It is warm and humid in summer and cold and dry in winter. The maximum temperature during summer is 36°C and the minimum in winter is 4°C. The relative humidity ranges from 70 to 98%. Rainfall of the region ranges from 3900 to 6800 $mmyr^{-1}$ (Directorate of Agriculture, Meghalaya, 2012).

Study Site and Vegetation

The study site, Siju Cave in the South Garo Hills, is locally known as Dobakol, cave of the bat, as it is the home for thousands of bats. According to field observation and previous records (Sinha, 1994, 1999; Bates and Harrison, 1997) in Siju Cave, the dominant bat species are *Rhinolophus subbadius*, *R. pusillus*, *R. pearsoni*, and *Miniopterus schreibersii*; these are mainly insectivorous. The Siju Cave is situated at lat. 25°21′16.17″ N and long. 90°41′08.09″ E at 95 m asl (Fig. 1). It was first explored by the British Geologic Survey in 1920. This cave is one of the longest caves in the Indian subcontinent and contains some of the finest river passages to be found anywhere in the world. The cave has many unexplored chambers and labyrinths (Fig. 2A). The majestic formations inside the cave, especially in Princess Di's Chamber, are among the special attractions of the cave. In the northeast direction of Siju Cave, Simsang River (Fig. 2B), originates from the Tura peak area and supports luxuriant growth of marshy and aquatic plants. Naphak Lake and the Siju wildlife and bird sanctuary are located close to Siju Cave. During winter, Siberian ducks migrate to the bird sanctuary. Previous studies on the Siju Cave fauna are listed in Table 1, but this is the first attempt of a palynological study on bat guano in relation to modern pollen,

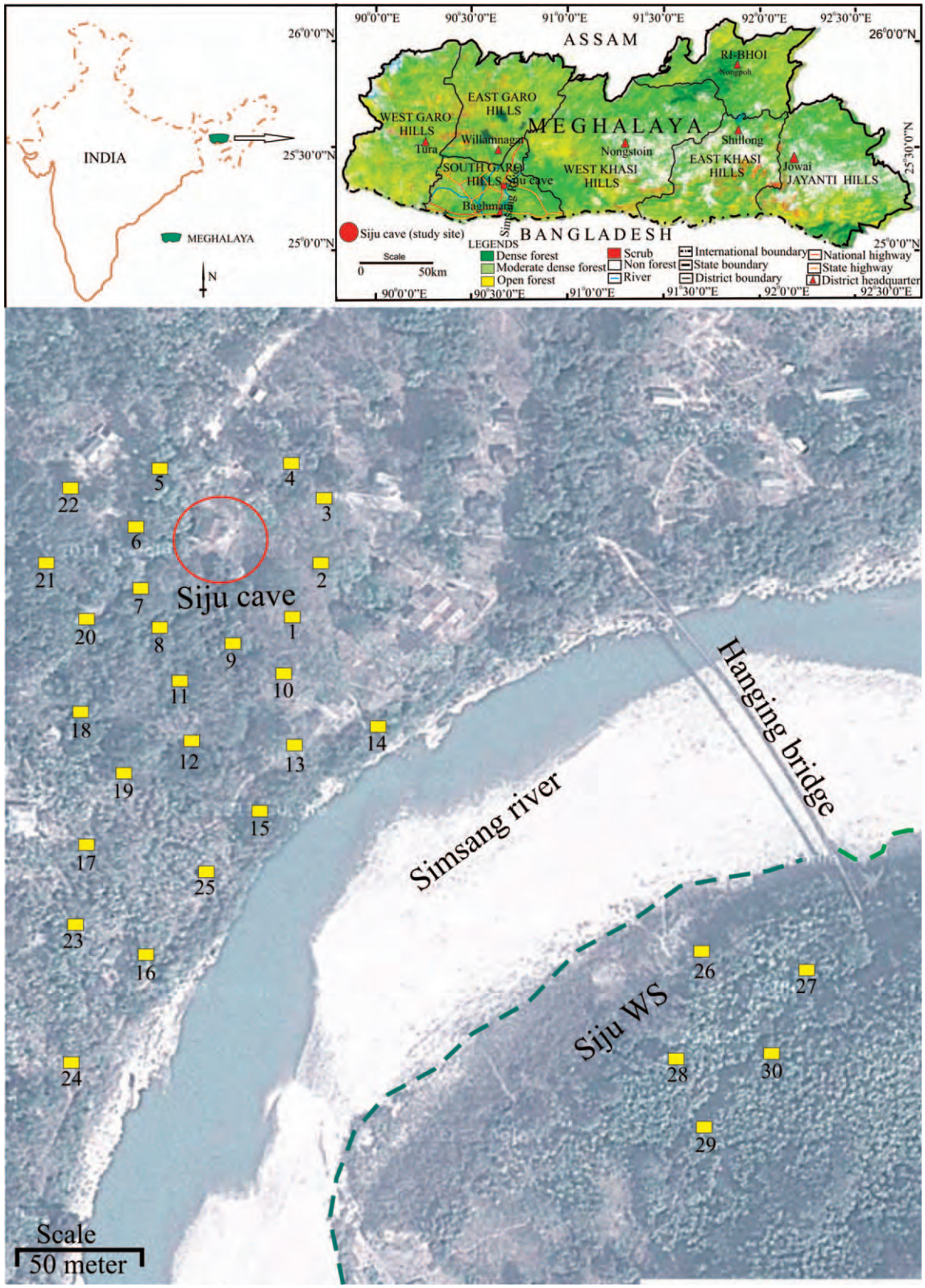

Figure 1. Map showing the location of Siju Cave in the South Garo Hills, Maghalaya. The numbers show the locations of the thirty surface samples.

Figure 2. A. The entrance of Siju Cave, South Garo Hills, Meghalaya. B. The hanging bridge over the Simsang River connecting the Siju Cave area and the Siju wildlife and bird sanctuary, Meghalaya. C. A view of *Nepenthes khasiana* growing luxuriantly, intermixed with *Gleichenia dichotoma*, in the entrance of Siju Cave. D. A view of the bat colony in their resting chamber inside Siju Cave. E. Bat guano collection inside Siju Cave. F. A view of the forest floor burning during winter in South Garo Hills.

Table 1. List of the recorded faunal taxa from Siju Cave, South Garo Hills, Meghalaya, with references.

Recorded Taxa	Reference
Coleoptera	Andrewes (1924)
Molluscas	Annandale and Chopra (1924)
Coleoptera	Blair (1924)
Diptera	Brunetti (1924)
Coleoptera	Cameron (1924)
Collembola	Carpenter (1924)
Diptera	Edwards (1924)
Araneids	Fage (1924)
Lepidoptera	Fletcher (1924)
Coleoptera	Fleutiaux (1924)
Tartarides	Gravely (1924)
Pisces	Hora (1924)
Rhynchota	Kemp and China (1924)
Diptera	Lamb (1924)
Lepidoptera	Meyrick (1924)
Gyrinidae	Ochs (1925)
Diptera	Patton (1924)
Hymenoptera	Rohwer (1924)
Myriapoda	Silvestri (1924)
Oligochaeta	Stephenson (1924)
Hymenoptera	Wheeler (1924)
Chiroptera	Bates and Harrison 1997
Chiroptera	Sinha (1999)
Teleostei	Kottelat et al. (2007)
Arachnida, Brachyura, Palaemonidae, Isopoda, Diplopoda, Orthoptera, Dictyoptera, Coleopteran, Diptera and Pisces	Harries et al. (2008)
Diptera	Disney (2009)

vegetation, and climate, and it will be greatly helpful to further palaeoecological research in the South Garo Hills of Meghalaya and to place this region within a global context.

The vegetation of the region is dominated by riparian taxa, including *Duabanga grandiflora*, *Syzygium polypetalum*, *Terminalia bellirica*, *Schima wallichii*, *Careya arborea*, and *Ficus pyriformis*, intermixed with evergreen and deciduous elements such as *Mesua ferrea*, *Elaeocarpus rugosus*, *Garcinia paniculata*, *Dillenia pentagyna*, *Emblica officinalis*, *Artocarpus chaplasha*, and *Adhatoda vasica*. The endemic pitcher plant *Nepenthes khasiana,* locally known as memang-kokshi by the Garo people, grows intermixed with the pteridophytic flora (Fig. 2C). The pteridophytes are dominated by *Lycopodium clavatum*, *Selaginella selaginoides*, *Dryopteris filixmas*, *Gleichenia dichotoma*, *Adiuntum caudatum*, *Cyathea gigantea*, *Angiopteris evecta*, and *Blechnum occidentale*. The forest floor is formed by dense humus, is litter-laden, and is often covered by grasses such as *Saccharum spontaneum*, *S. arundinaceum*, *Cynodon dactylon*, and *Neyraudia reynaudiana* associated with sedges like *Mariscus sumatrensis*, *Kyllinga monocephale*, *Fimbristylis dichotoma*, *Cyperus zollingeri*, and *Scleria terrestris*. During the rainy season, Zingiberaceae like *Curcuma aromatica* and other dicotyledonous herbs such as *Justicia simplex*, *Rungia pectinata*, *Amaranthus aspera*, *Evolvulus nummularius*, and *Polygonum orientale* are present in large numbers.

Materials and Methods

The location of Siju Cave was recorded by GPS with coordinates based on WGS1984. The cave was surveyed in detail, and fifty samples of approximately 50 g of bat guano were collected randomly from the floor of the bats' resting chamber inside the cave (Figs. 2D, E). A total of thirty surface samples of both soil and moss cushion were collected randomly from the area immediately outside Siju Cave. We also collected polliniferous plant materials for proper identification of taxa in the region by their pollen morphology. The specimens were placed in the Birbal Sahni Institute of Palaeobotany (BSIP) Herbarium.

The bat guano and surface samples were processed employing the standard acetolysis method (Erdtman, 1953). The samples were treated with 10% aqueous KOH solution to deflocculate the pollen and spores from the sediments followed by 40% HF treatment to dissolve silica content. Then the conventional procedure of acetolysis was followed using the acetolysis mixture 9:1 anhydrous acetic acid and concentrated H_2SO_4. Finally the material was kept in a 50% glycerin solution with a drop of phenol. Between 450 and 600 pollen and spores per sample were counted to produce the pollen spectra. Plant elements in the study were categorized into arboreals (trees, shrubs, and epiphytes), nonarboreals (terrestrial herbs and marshy taxa), highland taxa, ferns, and fungal remains with degraded palynomorphs. For the precise identification of fossil palynomorphs in the sediments, we consulted the reference pollen slides available at Birbal Sahni Institute of Palaeobotany (BSIP) herbarium of India, as well as the pollen photographs in the published literature (Chauhan and Bera, 1990; Nayar, 1990; Bera et al., 2009). Photodocumentation of the palynomorphs was made using an Olympus BX-61 microscope with DP25 digital camera under 40× magnification (Fig. 3). The pollen spectra were made using Microsoft Excel program and modified in Corel Draw-12 software. The frequency percentage of the recovered palynomorphs has been calculated in terms of the total palynomorphs.

Results

The modern pollen spectra of bat guano from Siju Cave and from the surface soil and moss cushion from its immediate surroundings are discussed below and provide an overview of modern pollen in relation to vegetation and climate in the region. The total of fifty modern bat

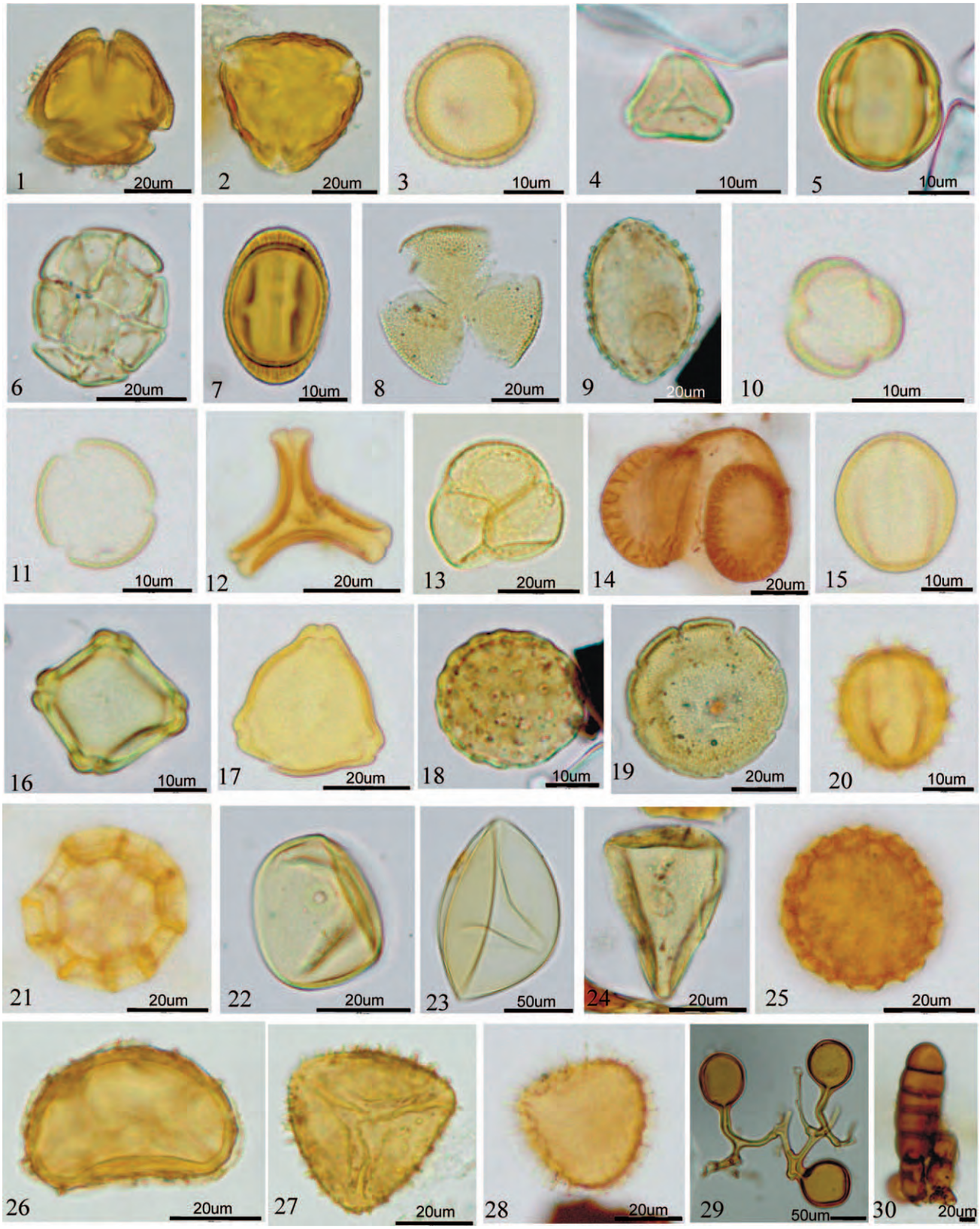

Figure 3. Palynoassemblage recovered from the bat guano and surface sample from South Garo Hills, Meghalaya. 1. *Mesua*, 2. *Schima*, 3. *Emblica*, 4. *Syzygium*, 5. *Terminalia*, 6. *Albizia*, 7. *Duabanga*, 8. Dipterocarpaceae, 9. *Areca*, 10. *Elaeocarpus*, 11. *Dillenia*, 12. *Dendropthoe*, 13. *Nepenthes*, 14. *Pinus*, 15. *Quercus*, 16. *Alnus*, 17. *Betula*,

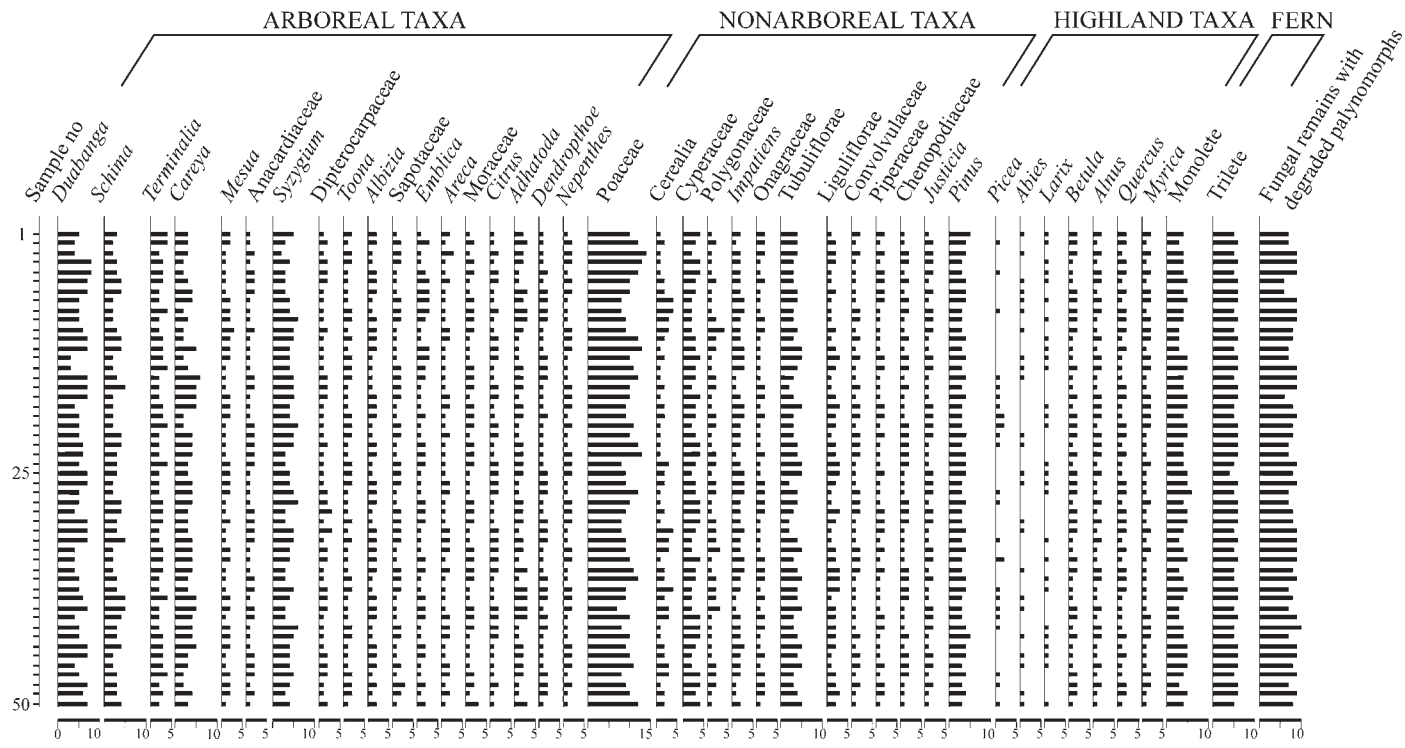

Figure 4. Pollen spectra of bat guano samples from Siju Cave, South Garo Hills, Meghalaya.

guano samples collected randomly from inside the cave are dominated by arboreals (42%), followed by nonarboreals (35%), fungal remains with degraded palynomorphs (10%), ferns (6%), and highland taxa (5%) (Fig. 4). The major arboreals include *Duabanga*, *Schima*, *Syzygium*, and *Careya* and are represented by maximum values up to 10%. Other associated taxa, such as *Schima*, *Semecarpus*, *Albizia*, *Adhatoda*, and *Nepenthes* have values of 1 to 6%. Nonarboreals like Poaceae, Cyperaceae, and Tubuliflorae have values of 1 to 15%. Ferns, both monolete and trilete, exhibit an average value of 4% and 5% respectively. Fungal remains like Microthyriaceae, *Glomus*, *Diplodia*, and *Meliola* are represented by maximum values up to 6%. Among the highland taxa, *Pinus* is recorded at values of 2%, whereas its associated taxa like *Abies* and *Picea* are only encountered in trace amounts (Fig. 4).

The thirty surface soil and moss cushions samples collected randomly from the immediate vicinity of the cave are dominated by arboreals (40%), followed by nonarboreals (37%), ferns (12%), fungal remains with degraded palynomorphs (7%), and highland taxa (4%) (Fig. 5). The major arboreals include *Duabanga*, *Syzygium*, Anacardiaceae, Moraceae, and *Careya* and are represented by maximum values up to 8%. The other associated taxa such as *Mesua*, *Elaeocarpus*, *Schima*, *Dillenia*, *Terminalia*, *Adhatoda*, and *Nepenthes* have values of 1 to 5%. Among nonarboreals like Poaceae, Tubuliflorae, Onagraceae and *Impatiens* the values range between 1 to 18%. Ferns, both monolete and trilete, have an average value of 5% and 6% respectively. Fungal remains like Microthyriaceae, *Cookeina*, *Tetraploa,* and *Glomus* are represented by a maximum value of 5%. The highland taxa *Pinus* is recorded at the value of 3%, whereas associated taxa *Abies* and *Picea* are represented by variable values.

Discussion

There are some difference between pollen percentages preserved in the bat guano and the surface samples from the vicinity of Siju Cave, although, in general, the palynodata reflect a close similarity between the bat guano and surface samples: (i) the pollen diversity from bat guano is higher than the surface samples, (ii) the number of arboreal taxa is higher in the bat guano samples, (iii) the Dipterocarpaceae pollen is markedly present in the bat guano, but is not found in the samples collected from the immediate vicinity of the cave, (iv) the fern spores are

←

18. Chenopodiaceae, 19. Convolvulaceae, 20. Tubuliflorae, 21. Liguliflorae, 22. Poaceae, 23. Cerealia, 24. Cyperaceae, 25. Polygonaceae, 26. Monolete, 27. Trilete, 28. *Lycopodium*, 29. *Glomus*, 30. *Meliola*.

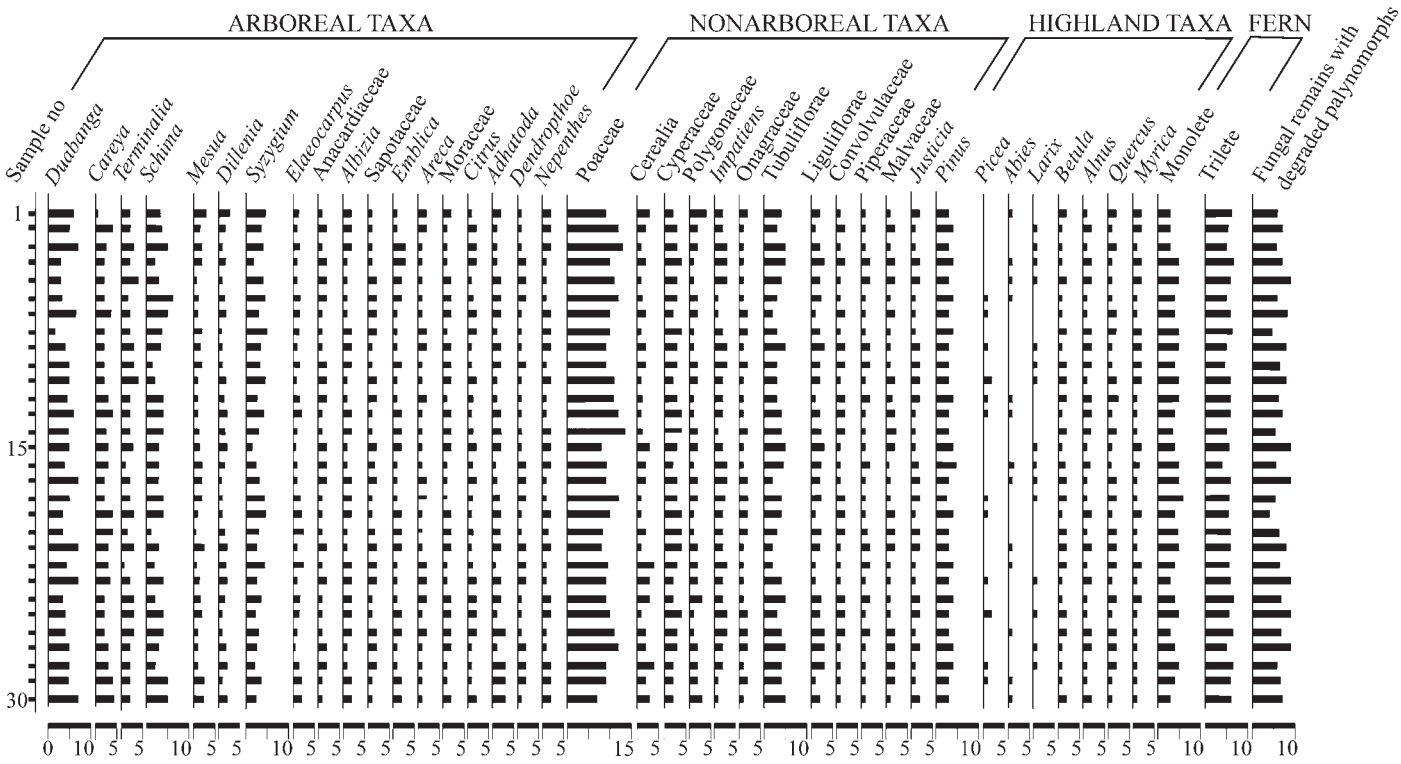

Figure 5. Pollen spectra of surface samples from the immediate vicinity of Siju Cave, South Garo Hills, Meghalaya.

comparatively few in the bat guano samples, and (v) the fungal remains, along with degraded palynomorphs, are comparatively higher in the bat guano samples.

Relationship of Palynoassemblage, Vegetation, and Climate

The bat guano from Siju Cave and the forest surface samples of moss cushion and soil collected from the immediate vicinity both contain pollen indicative of the tropical riparian forest intermixed with evergreen and deciduous elements under warm and humid climatic condition. Among the arboreals, the samples principally reflect the proximity of riparian taxa like *Duabanga*, *Syzygium*, *Careya*, and *Ficus* in the palynoassemblage that grows along the edge of the river Simsang. The associated evergreen and deciduous elements like *Mesua*, *Elaeocarpus*, *Garcinia*, *Schima*, *Dillenia*, *Albizia*, and Sapotaceae also exhibit 30 to 42% totals indicative of the heavy rainfall in the region. The presence of evergreen taxa, along with Piperaceae and Euphorbiaceae, suggests heavy rainfall in the region (Nair et al., 2010), which is reflected by the observed palynoassemblage in the sediments from both inside and outside of the cave. The occurrence of *Dendrophthoe* (epiphytic plants) pollen in the palynoassemblage is significant and reflects the existence of a primary forest that receives heavy rainfall in the region. The presence of *Areca* (betel nut) pollen along with cerealia and *Citrus* (orange) are strongly indicative of the human activity in the area. The presence of the highland taxa *Pinus*, *Betula*, *Abies*, *Picea*, and *Larix* in the bat guano deposit is significant and suggestive of strong winds from higher altitudes, or they may have been introduced by the migration of Siberian birds to the nearby Siju wildlife and bird sanctuary during winter. The palynodata of the surface samples from the immediate vicinity of the cave also reflect the riparian forest and are an exact match with the cave sample of bat guano. That both the vegetation and climate of the region are strongly governed by the Simsang River, along with the heavy rainfall, is indicated by the dominance of the riparian taxa *Duabanga*, *Ficus*, and *Careya* and other heavy-rainfall indicator taxa like *Mesua*, *Syzygium*, and *Elaeocarpus*. The samples from inside the cave also reflect local and regional floras quite well (Burney and Burney, 1993; Carrión et al., 2006), and the pollen contained in the bat guano matches well that in the surface sediments of lake and peat (Maher, 2006) that supports our palynodata. The abundance of *Nepenthes khasiana* in bat guano is significant and suggests the presence of insectivorous and riparian habitat growing in very limited pockets in and around the area. The presence of *Nepenthes* pollen is strongly suggestive of heavy rainfall and a perennial water system in the region, because *Nepenthes khasiana* generally grows in the shade along rivers and streamlets in Meghalaya (Haridasan and Rao, 1985). The preservation of Dipterocarpaceae pollen in the bat guano is informative with regard to the size of the areas sampled by the bats, as it does not grow near the Siju Cave and the closest plants are several kilometers distance from the study area. Leroy

and Simms (2006) noted that bats can migrate hundreds of kilometers from their shelter and is supported by our pollen data, which strongly suggest that the bats fly several kilometers for their food. The fern spores, especially *Cyathea*, *Dryopteris*, and *Pteris*, in the bat guano are local in origin and grew in the immediate vicinity of the cave. Their presence may also be due to the influence of wind activity. Caves with a large entrance and strong air circulation are likely to have higher pollen presence resulting from wind than caves with smaller entrances and minimal air circulation (Burney and Burney, 1993). However, the occurrence of terrestrial ferns, especially *Gleichenia*, *Dryopteri*s, and *Lycopodium*, signifies high rainfall and humid climatic conditions in the area (Basumatary et al., 2013), which is exactly reflected in the palynoassemblage of the studied samples. The abundance of fungal remains such as *Meliola*, *Cookeina*, Microthyriaceae, and *Diplodia,* along with degraded palynomorphs, is strongly indicative of warm and humid climatic condition during sedimentation in the region. The presence of *Glomus* with hyphae in surface-soil and moss-cushion samples is strongly indicative of high soil erosion in the region. Medicinal plants like *Swertia chirata* and *Rauvolfia serpentina* are not encountered in the bat guano, although they are present in the luxuriant growth in the vicinity of the cave. Their absence may be due to their bitter in taste and avoidance by insects that might in turn be eaten by the bats.

Conclusions

The palynological study on bat guano from Siju Cave is the first to be conducted in India. The palynodata from both the modern bat guano and surface samples from the immediate vicinity of the cave are very similar and indicate the existence of mainly riparian forest intermixed with both evergreen and deciduous taxa that exactly coincides with the extant vegetation. The bat guano deposit in Siju Cave can be considered as a reliable source of palaeoecological data that can be used to support data from surface and sedimentary soil profiles and to substitute for the scarcity of lakes, swamps, and wetlands in Meghalaya, with the caveat that bats can forage long distances from their roost site in the cave and may accumulate pollen from plants not found in the immediate vicinity of the cave. Lastly, multidisciplinary studies that integrate pollen data from caves with paleontological, archaeological, zoological, and geological data could play an important role in any palaeoecological study of the South Garo Hills of Meghalaya and at the global level.

Acknowledgements

Authors thank to the Director, Birbal Sahni Institute of Palaeobotany (BSIP), Lucknow, India, for infrastructure facility and permission to publish the paper. We also thank a number of forest officials for their help during field work.

References

Andrewes, H.E., 1924, Coleoptera of the Siju cave, Garo Hills, Assam: I Carabidae: Records of the Indian Museum, v. 26, p. 115–117.

Annandale, N., and Chopra, B., 1924, Molluscas of the Siju cave, Garo Hills, Assam: Records of the Indian Museum, v. 26, p. 33–40.

Anonymous, 2006, Meghalaya resource F\BIOSPHERE_RESERVES. http://meghalaya.nic.in/tourism/cave.htm [accessed 20 November 2006].

Bastin, B., 1978, L'analyse pollinique des stalagmites: une nouvelle possibilité d'approach des fluctuations climatiques du Quaternaire: Annales de la Société Géologique de Belgique, v. 101, p. 13–19.

Bastin, B., Cordy, J.-M., Gewelt, M., and Otte, M., 1986, Fluctuations climatique enregistrées depuis 125 000 ans dans les couches de remplissage de la GrotteScladina (Provence de Namur, Belgique): Bulletin de l'Association Française pour l'étude du Quaternaire, v. 23, no. 2–3, p. 168–177. doi:10.3406/quate.1986.1808.

Basumatary, S.K., and Bera, S.K., 2007, Modern pollen-spore assemblage from sediment of tropical moist deciduous forest, East Garo Hills, Meghalaya: Journal of Palynology, v. 43, p. 111–118.

Basumatary, S.K., and Bera, S.K., 2010, Development of vegetation and climate change in West Garo Hills since late Holocene: pollen sequence and anthropogenic impact: Journal of the Indian Botanical Society, v. 89, p. 143–148.

Basumatary, S.K., and Bera, S.K., 2012, Vegetation succession and climate change in western Garo Hills, Meghalaya, India since 11,643 years BP: a palynological record: International Journal of Earth Science and Engineering, v. 5, no. 4, p. 749–758.

Basumatary, S.K., Dixit, S., Bera, S.K., and Mehrotra, R.C., 2013, Modern pollen assemblages of surface samples from Cherrapunjee and its adjoining areas, Meghalaya, northeast India: Quaternary International, v. 298, p. 68–79.

Bera, S.K., Basumatary, S.K., and Dixit, S., 2009, Studies on pollen morphology and phenological characteristics of some economically important arborescent taxa of tropical forest lower Brahmaputra Valley, Assam, North East India: Journal of Palynology, v. 43, p. 1–9.

Blair, K.G., 1924, Coleoptera of the Siju Cave, Garo Hills, Assam: IV Histeridae, Hydrophilidae, Erotylidae, Lathridiidae, Tenebrionidae and Hylophilidae: Records of the Indian Museum, v. 26, p. 120–122.

Brunetti, E., 1924, Diptera of the Siju Cave, Garo Hills, Assam: I. Tipulidae, Tabanidae, Anthomyidae, Acalyptrate Muscidae and Phoridae: Records of the Indian Museum, v. 26, p. 99–106.

Bates, P.J.J., and Harrison, D.L., 1997, Bats of the Indian Subcontinent, Kent, Harrison Zoological Museum, 268 p.

Batina, M.C., and Reese, C.A., 2011, A Holocene pollen record recovered from a guano deposit: Round Spring Cavern, Missouri, USA: Boreas, v. 40, no. 2, p. 332–341. doi:10.1111/j.1502-3885.2010.00186.x.

Boscaiu, N., and Lupsa, V., 1967a, Palynological research in the "Grota Haiducilor" Cave near the Herculaneumspa (Romania): Revue Roumaine de Biologie, Série de Botanique, v. 12, p. 137–140.

Boscaiu, N., and Lupsa, V., 1967b, Cercetări palinologice în Pestera-Veterani din Defileul Dunării, Contributii Botanice, p. 39–46.

Burney, D.A., and Burney, L.P., 1993, Modern pollen deposition in cave sites: experimental results from New York State: New Phytologist, v. 124, p. 523–535. doi:10.1111/j.1469-8137.1993.tb03844.x.

Cameron, M., 1924, Coleoptera of the Siju Cave, Garo Hills, Assam: II. New species of Staphylinidae: Records of the Indian Museum, v. 26, p. 118–119.

Carpenter, G.H., 1924, Collembola of the Siju Cave, Garo Hills, Assam: Records of the Indian Museum, v. 26, p. 285–289.

Carrión, J.S., 1992, Late Quaternary pollen sequence from Carihuela Cave, southeastern Spain: Review of Palaeobotany and Palynology, v. 71, p. 37–77. doi:10.1016/0034-6667(92)90157-C.

Carrión, J.S., Munuera, M., Navarro, C., Burjachs, F., Dupré, M., and Walker, M.J., 1999, The palaeoecological potential of pollen records in caves: the case of Mediterranean Spain: Quaternary Science Reviews, v. 18, p. 1061–1073. doi:10.1016/S0277-3791(98)00002-X.

Carrión, J.S., Scott, L., and Marais, E., 2006, Environmental implications of pollen spectra in bat droppings from southeastern Spain and potential for palaeoenvironmental reconstructions: Review of Palaeo-

botany and Palynology, v. 140, p. 175–186. doi:10.1016/j.revpalbo.2006.03.007.

Chauhan, M.S., and Bera, S.K., 1990, Pollen morphology of some important plants of tropical deciduous sal (*Shorearobusta*) forests, district Sidhi, Madhya Pradesh: Geophytology, v. 20, no. 1, p. 30–36.

Coles, G.M., and Gilbertson, D.D., 1994, The airfall-pollen budget of archaeologically important caves: Creswell Crags, England: Journal of Archaeological Science, v. 21, p. 735–755. doi:10.1006/jasc.1994.1073.

Coles, G.G., Gilberton, D.D., Hunt, C.O., and Jenkinson, R.D.S., 1989, Taphonomy and the palynology of cave deposits: Cave Science, v. 16, p. 83–89.

Denniston, R.F., Gonza'lez, L.A., Asmerom, Y., Sharma, R.H., and Reagan, M.K., 2000, Speleothem Evidence for Changes in Indian Summer Monsoon Precipitation over the Last; 2300 Years. Quaternary Research, v. 53, p. 196–202.

Davis, O.K., 1990, Caves as sources of biotic remains in arid western North America: Palaeogeography, Palaeoclimatology, Palaeoecology, v. 76, p. 331–348. doi:10.1016/0031-0182(90)90119-R.

Disney, R.H.L., 2009, Scuttle flies (Diptera: Phoridae) from caves in Meghalaya, India: Journal of Cave and Karst Studies, v. 71, no. 1, p. 81–85.

Draxler, I., 1972, Palynologische Untersuchungen an Sedimenten aus der Salzofen-höhleim Toten Gebirge: Annalen des Naturhistorischen Museums in Wien, v. 76, p. 161–186.

Edwards, F.W., 1924, Diptera of the Siju cave, Garo Hills, Assam: II. Chironomidae: Records of the Indian Museum, v. 26, p. 107–108.

Erdtman, G., 1953, An Introduction to Pollen Analysis, New York, Ronald Press, 239 p.

Fage, L., 1924, Araneids from the Siju Cave, Garo Hills, Assam: Records of the Indian Museum, v. 26, p. 63–67.

Feurdean, A., Persoiu, A., Pazdur, A., and Onac, B.P., 2011, Evaluating the palaeoecological potential of pollen recovered from ice in caves: A case study from Scărisoara Ice Cave, Romania: Review of Palaeobotany and Palynology, v. 165, p. 1–10. doi:10.1016/j.revpalbo.2011.01.007.

Fletcher, T.B., 1924, Lepidoptera of the Siju cave, Garo Hills, Assam I Pyralidae: Records of the Indian Museum, v. 26, 113 p.

Fleutiaux, E., 1924, Coleoptera of the Siju cave, Garo Hills, Assam III Elateridae: Records of the Indian Museum, v. 26, 119 p.

Geantă, A., Tantău, I., Tămas, T., and Johnston, V.E., 2012, Palaeoenvironmental information from the palynology of an 800 year old bat guano deposit from Măgurici Cave, NW Transylvania (Romania): Review of Palaeobotany and Palynology, v. 174, p. 57–66. doi:10.1016/j.revpalbo.2011.12.009.

Gravely, F.H., 1924, Tartarides from the Siju cave, Garo Hills, Assam: Records of the Indian Museum, v. 26, p. 61–62.

Groner, U., 2004, Palynology and sediment data from the high alpine karst cave on Jungfraujoch, Switzerland: Eclogae Geologicae Helveticae, v. 97, p. 237–243. doi:10.1007/s00015-004-1122-9.

Gupta, H.P., and Sharma, C., 1985, Pollen analysis of modern sediments from Khasi and Jaintia hills, Meghalaya, India: Journal of Palynology, v. 21, p. 167–173.

Haridasan, K., and Rao, R.R., 1985, Forest Flora of Meghalaya, vol I, Dehradun, India, Bishen Singh Mahendra Pal Singh, p. 1–451.

Harris, D.R., 1972, The origin of agriculture in the tropics: American Scientist, v. 60, p. 180–193.

Harries, D.B., Ware, F.J., Fischer, C.W., Biswas, J., and Kharpran-Daly, B.D., 2008, A review of the biospeleology of Meghalaya, India: Journal of Cave and Karst Studies, v. 70, no. 3, p. 163–176.

Hooker, J.D., 1905, Himalayan Journals: Notes of a Naturalist in Bengal, the Sikkim and Nepal Himalayas, the Khasia Mountains &c, London, Ward, Lock, Bowden and Co., 639 p.

Hora, S.L., 1924, Fish of the Siju cave, Garo Hills, Assam: Records of the Indian Museum, v. 26, p. 27–31.

Hunt, C.O., and Rushworth, G., 2005, Pollen taphonomy and airfall sedimentation in a tropical cave: the West Mouth of The Great Cave of Niah in Sarawak, Malaysian Borneo: Journal of Archaeological Science, v. 32, p. 465–473. doi:10.1016/j.jas.2004.11.005.

Kemp, S., and China, W.E., 1924, Rhynchota of the Siju cave, Garo Hills, Assam: Records of the Indian Museum, v. 26, p. 93–97.

Kottelat, M., Harries, D.R., and Proudlove, G.S., 2007, *Schistura papalifera*, a new species of cave loach from Meghalaya, India (Teleostei: Balitoridae): Zootaxa, no. 1393, p. 35–44.

Kral, F., 1968, Pollenanlytische Untersuchungen zur Frage des Alters der Eisbildungen in der Dachstein-Rieseneishohle: Die Höhle, v. 19, p. 41–51.

Lamb, C.G., 1924, Diptera of the Siju cave, Garo Hills, Assam III Dolichopodidae: Records of the Indian Museum, v. 26, p. 108–112.

Leroy, S.A.G., and Simms, M.J., 2006, Iron age to medieval entomogamous vegetation and *Rhinolophus hipposideros* roost in South-Eastern Wales (UK). Palaeogeography, Palaeoclimatology, Palaeoecology, v. 237, p. 4–18. doi:10.1016/j.palaeo.2005.11.025.

Maher, L.J., Jr., 2006, Environmental information from guano palynology of insectivorous bats of the central part of the United States of America: Palaeogeography, Palaeoclimatology, Palaeoecology, v. 237, p. 19–31. doi:10.1016/j.palaeo.2005.11.026.

McGarry, S.F., and Caseldine, C., 2004, Speleothem Palynology: an undervalued tool in Quaternary studies: Quaternary Science Review, v. 23, p. 2389–2404. doi:10.1016/j.quascirev.2004.06.007.

Meyrick, E., 1924, Lepidoptera of the Siju cave, Garo Hills, Assam II Tineidae: Records of the Indian Museum, v. 26, 114 p.

Mittermeier, R.A., Gil, P.R., Hoffmann, M., Pilgrim, J., Brooks, T., Mittermeier, C.G., Lamoreux, J., and da Fonseca, G.A.B., 2005, Hotspots revisited: Earth's Biologically Richest and Most Endangered Terrestial Ecosystems, Arlington, Virginia, Conservation International, 392 p.

Nair, K.M., Padmalal, D., Kumaran, K.P.N., Sreeja, R., Limaye, R.B., and Srinivas, R., 2010, Late Quaternary evolution of Ashtamudie-Sasthamkotta lake systems of Kerala, south west India: Journal of Asian Earth Science, v. 37, p. 361–372. doi:10.1016/j.jseaes.2009.09.004.

Navarro Camacho, C., Carrión, J.S., Navaro, J., Munuera, M., and Prieto, A.R., 2000, An experimental approach to the palynology of cave deposits: Journal of Quaternary Science, v. 15, p. 603–619. doi:10.1002/1099-1417(200009)15:6<587::AID-JQS533>3.0.CO;2-2.

Navarro, C., Carrión, J.S., Munuera, M., and Prieto, A.R., 2001, Cave surface pollen and the palynological potential of karstic cave sediments in palaeoecology: Review of Paleobotany and Palynology, v. 117, p. 245–265. doi:10.1016/S0034-6667(01)00095-1.

Nayar, T.S., 1990, Pollen Flora of Maharashtra State, India, New Delhi, Today and Tomorrow's Printers & Publishers, 157 p.

Nieves-Rivera, Á.M., 2003, Mycological Survey of Río Camuy Caves Park, Puerto Rico: Journal of Cave and Karst Studies, v. 65, no. 1, p. 23–28.

Ochs, G., 1925, Descriptions of new Asiatic Gyrinidae: Records of the Indian Museum, v. 27, p. 193–204.

Patton, W.S., 1924, Diptera of the Siju cave, Garo Hills, Assam IV Nycteribiidae: Records of the Indian Museum, v. 26, 112 p.

Pendleton, M., Bryant, V.M., and Pendleton, B.B., 1996, Entomopalynology, *in* Jansonius, J., and McGregor, D.C., eds., Palynology: Principles and Applications, Dallas, American Association of Stratigraphic Palynologists Foundation, Contributions Series, v. 3, p. 939–943.

Pop, E., and Ciobanu, I., 1950, Analize de polen în ghiata dela Scarisoara, Analele Academiei Republicii Populare Romane, seria Geologie, Geografie, Biologie, Stiin Tehnice si Agricole, III, p. 23–50.

Qin, Xiaoguang, Tan, Ming, Liu, Tungsheng, Wang, Xianfeng, Li, Tieying, and Lu, Jinpo, 1999, Spectral analysis of a 1000-year stalagmite lamina-thickness record from Shihua Cavern, Beijing, China, and its climatic significance: The Holocene, v. 9, p. 689–694. doi:10.1191/095968399671019413.

Rohwer, S.A., 1924, Hymenoptera of the Siju cave, Garo Hills, Assam II Description of a new Braconid: Records of the Indian Museum, v. 26, p. 124–125.

Sauer Carl, O., 1952, Agricultural Origin and Dispersals, New York, American Geographical Society, Bowman Memorial Lectures series 2, 131 p.

Sears, P.B., and Roosma, A., 1961, A climatic sequence from two Neveda caves: American Journal of Science, v. 259, p. 669–678. doi:10.2475/ajs.259.9.669.

Silvestri, F., 1924, Myriapoda from the Siju cave, Garo Hills, Assam: Records of the Indian Museum, v. 26, p. 71–79.

Sinha, Y.P., 1994, Occurrence of Kashmir Cave Bat *Myotis longipes* (Dobson, 1873) in Meghalaya, India. Geobios New Reports, v. 13, p. 72–73. Sinha, Y.P., 1999, Bats of the Siju Cave, South Garo Hills District, Meghalaya, India: taxonomy and bionomics: Records of the Zoological Survey of India, v. 97, p. 101–122.

Stephenson, J., 1924, Oligochaeta of the Siju cave, Garo Hills, Assam: Records of the Indian Museum, v. 26, p. 127–135.

Vivilov, N.I., 1951, The Origin, Variation, Immunity and Breeding of Cultivated Plants, Waltham, Massachusetts, Chronica Botanica, 364 p.

Wheeler, W.M., 1924, Hymenoptera of the Siju cave, Garo Hills, Assam I *Triglyphothrix striatidens* Emery as a cave ant: Records of the Indian Museum, v. 26, p. 123–124.

White, W.B., 2007, Cave sediments and paleoclimate. Journal of Cave and Karst Studies, v. 69, p. 76–93. Zhang, Meiliang, Yuan, DaoXian, Lin, Yushi, Qin, Jiaming, Bin, Li, Cheng, Hai, and Edwards, R.L., 2004, A 6000-year high-resolution climatic record from a stalagmite in Xiangshui Cave, Guilin, China: The Holocene, v. 14, p. 697–702. doi:10.1191/0959683604hl748rp.

M. Łyskowski, E. Mazurek, and J. Ziętek – Ground Penerating Radar investigation of limestone karst at the Odstrzelona Cave in Kowala, Świętokrzyskie Mountains, Poland. *Journal of Cave and Karst Studies,* v. 76, no. 3, p. 184–190. DOI: 10.4311/2014EX0001

GROUND PENERATING RADAR INVESTIGATION OF LIMESTONE KARST AT THE ODSTRZELONA CAVE IN KOWALA, ŚWIĘTOKRZYSKIE MOUNTAINS, POLAND

Mikołaj Łyskowski, Ewelina Mazurek, and Jerzy Ziętek
AGH University of Science and Technology, Faculty of Geology, Geophysics and Environmental Protection, A. Mickiewicza 30 Ave., 30-059 Krakow, Poland, lyskowski@geol.agh.edu.pl

Abstract: Ground Penetrating Radar (GPR) is one of the most effective and rapid types of geophysical surveys methods. The variety of its uses is limited only by the availability of components such as antennas with different frequencies of emitted radio waves. The application of GPR ranges from engineering applications and geological investigations to assessing the condition of old trees. The authors tested GPR measurements in a geological exploration of a newly discovered limestone cave in the Świętokrzyskie Mountains region, the Odstrzelona Cave in Kowala, near the village of that name. Investigations were ordered by the municipality of Sitkówka-Nowiny, in the Świętokrzyskie district in Poland. GPR surveys were conducted in the vicinity of a known cave entrance to see if information could be gained on nearby karst features. GPR investigations documented two additional chambers and a few more openings in the limestone. Unfortunately, they are probably too small to explore.

Introduction

Ground Penetrating Radar (GPR) is a fast geophysical method that allows precise and effective recognition of geological formations below the surface. Dry or moderately wet solid rocks are the best medium for such a survey. Review of the available literature shows that the GPR method is a good geophysical tool for detecting karst phenomena and caves. Doolittle and Collins (1998) compared the electromagnetic induction method to GPR results and obtained very good results. Chamberlain et al. (2000) gave examples of cave detection in limestones. Their surveys gave good results and thanks to a grid of parallel profiles, it was possible to present them in different ways, as both classical profiles and time slices. Another example of the application of the GPR method in detecting caves is presented by Beres et al. (2001), in which the GPR method was compared to microgravimetric measurements. The obtained results are good examples of GPR profiles. Anomalies in GPR echograms were confirmed by the gravity measurement results.

Investigations carried out by the authors and presented in this paper were focused on a cave newly rediscovered in 2008 near the city of Kielce, central Poland, and on detecting karst phenomena. The cave was probably discovered many years before during exploration work performed by the workers of the quarry Stara Trzuskawica, who shot away the ceiling in the entrance tunnel of the cave. For safety reasons, in the 1970s the cave was drilled and filled with limestone rubble made from surrounding rocks (Grzelak, 2012). As a result, the cave was unavailable for many years following the closure of the quarry. Speleologists who investigated the quarry named it Odstrzelona Cave in Kowala (Polish word *odstrzelona* means shoot away; *Kowala* is the village where the cave is located). After the discovery of the entrance, they wanted to seek karst areas adjacent to the cave. Speleologists proposed GPR measurements, because of previous experience with that method. Before the survey, researchers analyzed available geological information and made a local inspection to determine if use of GPR was feasible. The survey was done in November 2010. The data from the GPR measurements were processed and interpreted very carefully to provide a basis for future speleological investigations, as well as for evaluating risk to public safety. We have obtained results of a very good quality that allowed us to precisely locate karst objects in the limestone and the location of unknown chambers, voids, and cracks.

Study Area

In terms of Polish geographical regions presented by Kondracki (2011), the area where the Odstrzelona Cave in Kowala is located belongs to the Kielce Upland macro-region located in central Poland. More precisely, it is the Świętokrzyskie (Holy Cross) Mountains mezzo-region and the Chęcińskie Hills micro-region. This area is composed of limestone and dolomite of the Middle Devonian period.

The cave is located in the closed quarry Stara Trzuskawica north of the village of Kowala in the municipality of Sitkówka-Nowiny. Rocks forming the walls of the cave are Devonian limestones. The origin of the cave is associated with a typical karst processes. The entrance is artificial, created during exploration work in the quarry. Only a small part of the cave is accessible. Access to the rest of the cave is not possible because of the collapse of ceiling and walls, which took place after the blasting at the quarry. The collapsed tunnels are filled with

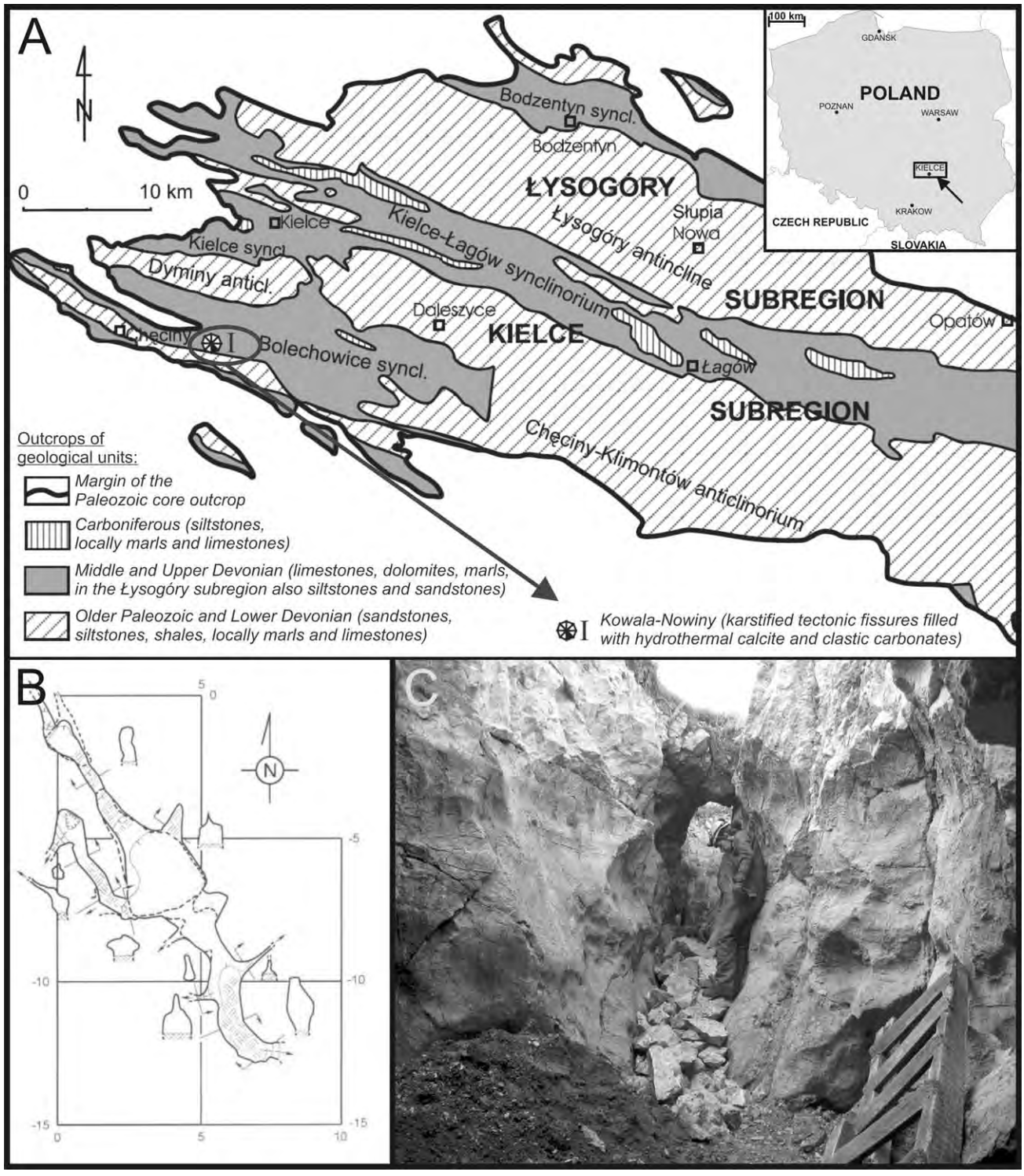

Figure 1. A—Geological map of the Świętokrzyskie (Holy Cross) Mountains mezzo-region, with inset showing its location in Poland (modified from Urban, 2007). B—A surface geological map of the Odstrzelona Cave in Kowala (Grzelak, 2012). C—Photo from inside of the cave taken by Mr. Maciej Grzelak.

limestone rubble. The open part has been explored and has a length of 28.8 m and a height reaching 3.8 m (Grzelak, 2012). Figure 1 shows the location of the cave and the surrounding geology.

Because of terrain topography typical of an opencast quarry, it was not possible to conduct measurements in a parallel grid. Surveys had to be carried out along specially cut paths in the vegetation surrounding the area. Additional

problems were caused by the multiple levels of the closed quarry. The direction and location of GPR profiles was determined by the local speleologists who had rediscovered the cave. Cut paths were made in places interesting for them and where they predicted continuation of the karst cave. The GPR profiles are shown in Figure 2.

Basics of GPR Survey

A GPR system includes central processing unit, signal generator, transmitter, transmitting and receiving antennas, receiver, and measuring gear. Today's systems have an onboard laptop computer that facilitates data acquisition and pre-processing in the field (Reynolds, 1997). The modern system uses the bistatic type of antennas in which two separate antennas are used, with one serving as a transmitter and the other as a receiver (Annan, 2001). The GPR systems produced today use antennas with frequencies from 10 MHz to 6000 MHz (British custom GPR system Groundvue 5C). Based on their structure, bistatic antennas can be divided into the two most commonly used types, shielded and unshielded. In the case of the first type, transmitting and receiving antennas are encased in an electromagnetic shield. The housing makes them less prone to external interference, such as reflections from trees, and is also designed for aiming the electromagnetic (EM) wave directly into the medium. Unshielded antennas are not shielded from the interference and are not physically integrated. Separation of transmitting and receiving antennas makes it possible to carry out investigations with different spacing distances between the dipoles and with different polarizations of the dipoles in relation to the profile line. Unshielded antennas also allow the special kind of survey called WARR profiling (Wide-Angle Reflection and Refraction, the final result of which is an echogram that is used for determination of the EM wave propagation velocity in the medium (Łyskowski and Mazurek, 2013)).

The GPR system is based on a transmitter generating a pulse of radio waves at a frequency determined by the characteristics of the antennas. EM waves are emitted from a source to detect an object at a distance and determine the direction to the object as well as the distance to the object. In order for an object to reflect radio waves it must have different dielectric properties from the surrounding material, referred to as the medium (Annan, 2001). Emitted radio waves travel at a speed that depends on the material in which they propagate. Each scan lasts as long as the total two-way travel time range. This value, defined as the time window, can be set by the operator from a few tens to several thousands of nanoseconds (Reynolds, 1997).

The electromagnetic characteristics of materials are related to their composition and water saturation. Due to the high frequency of radar waves, they are sensitive to both changes in conductivity and dielectric properties of materials, which affect the speed of radio-wave propagation and the attenuation of electromagnetic waves in the medium (Reynolds, 1997).

Wave attenuation determines the depth range of GPR method. Wave attenuation means the gradual reduction of an electromagnetic pulse's amplitude along the travel path. It depends on four basic factors, the geometrical divergence of the wave front from the point source of the wave, scattering related to nonhomogeneity of the medium, propagation dispersion of the waves, which depends on frequency, and the electrical conductivity of the medium, usually mainly due to pore fluids (Annan, 2001).

The frequency of the signal emitted by the antennas also defines the depth range and the resolution. The lower the frequency of emitted EM wave, the greater the depth penetration, but the lower resolution of the survey. On the other hand, with increasing frequency, the resolution is higher, but the range decreases.

For the GPR method, the concept of resolution is important, but quite complex. We can define vertical and horizontal resolutions. The simplest definition of both resolutions says that it is the minimum distance between two objects with the same cross section that are visible on the echogram as separate anomalies (Annan, 2001).

Methods

The GPR surveys presented in this paper were obtained using a ProEx GPR unit (MALA Geoscience, Sweden) with a 250 MHz shielded antenna. This equipment allowed the acquisition of information to a theoretical depth range of about 13 m. Test measurements with a 100 MHz unshielded antenna were done along a single profile, profile 16, that was located above the cave. The obtained depth penetration reached about 18 m. The whole case study consists of sixteen profiles. Their courses and locations are presented in Figure 2 on a schematic map of the survey site, along with sample echograms.

The echogram is a final result of the GPR survey. It is composed of the traces that register the reflected EM wave amplitudes as a function of time. The traces are arranged one by one along the X-axis. The length of the profile is calculated by the computer by revolving the measuring gear connected to the antennas. These mechanisms can generate small errors in determining the profile length. Despite the fact that the measurement is done in steps declared in centimeters, it is called continuous.

Raw data collected from the GPR surveys were recorded in nanoseconds. To obtain the vertical axis of the echograms as a depth scale in meters, it was necessary to do a time-to-depth conversion. This process needs the value of EM wave velocity in the medium, which can be obtained from WARR profiling. The velocity can be also calculated from the relative dielectric constant (ε_r) taken from published data (e.g. Reynolds, 1997, p. 682–749; OYO, 1988; MALÅ, 2009). To do so, the EM wave velocity is given by the speed of light in vacuum, 0.3 m ns^{-1},

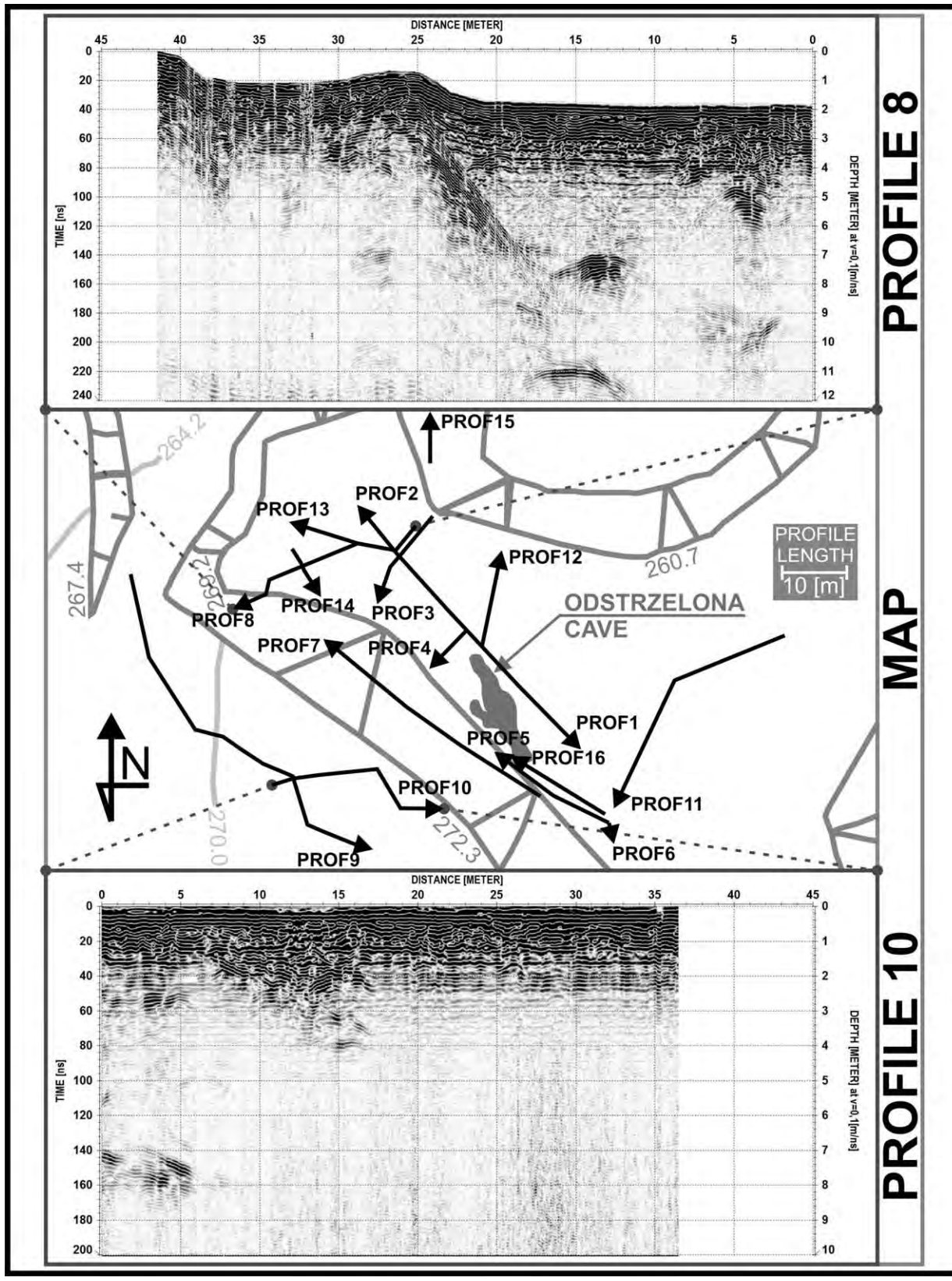

Figure 2. Schematic geographical map of survey site containing position and course of GPR profiles (black lines with arrows) and the location of Odstrzelona Cave in Kowala (center); Two echograms, from profiles 8 and 10, with visible anomalies from karst features. Note that the distance scale along the profiles in the top echogram is backwards. Light gray lines are isolines (elevation), and dark gray lines are contours of the excavation in the quarry Stara Trzuskawica.

divided by the square root of the relative dielectric constant of the medium (Karczewski et al., 2011). Due to the topography of the terrain and the vegetation, the authors determined the velocity by using an estimation from a table.

DATA PROCESSING AND RESULTS

The raw data were processed using the software ReflexW (Sandmeier Scientific Software). Data-processing work-flow included noise removal, frequency filtering, gaining, and smoothing. It is also possible to apply an approximate topographic shape of the area (profile 8 in Figure 2). The data presented in this paper were processed as follows, using the procedure names in the program (ReflexW, 2009): ''move starttime'' accepts a fixed value in nanoseconds that is the time of the first signal in the echogram. ''subtract-DC-shift'' calculates the mean value of the trace (the ''DC value'') for the given time range and subtracts this value from all data. ''substract-mean (dewow)'' creates a moving time window along the Z axis, subtracting the mean values from the actual data. ''bandpassbutterworth'' performs bandbass frequency filtering in the time domain of each trace. ''time cut'' removes trace values below a specified time value. ''gain function'' strengthens reflections with a time-dependent multiplier. ''average xy-filter'' is a smoothing filter that calculates the average for a specified data range. And ''static correction,'' applied only to profile 8 in Figure 2, applies surface topography to the echogram.

The data-processing work-flow presented above was chosen as the most effective from several that have been tried. Time-depth conversion of the GPR data was done with the use of published data for the relative dielectric constant of limestone. The assumed value $\varepsilon_r = 9$ corresponds to electrical conductivity of medium-wet limestone (OYO, 1988). It gives an EM wave velocity calculated as $v = 0.1$ m ns^{-1}. The conversion from nanoseconds to meters depth is then a factor of 20, since the echo has traveled both ways.

Profile 8 shown in Figure 2 contains information about the topography. Please notice that the horizontal axis in this plot is in inverse order. The visible dipping reflections, which start from 25 m along the profile (below abbreviated r-m, for running meters), can be assigned to the geological layers of limestones or karst fissures. Between 11 and 17 r-m there are two anomalies at the depth of 7 and 10.5 m that could originate from karst voids. At about 4 r-m at the depth of 4 m, the anomaly of a void is clearly visible, and another one that could be induced by deep cracks in the limestone, is visible at a depth of 9 m.

At the beginning of profile 10 there is a visible anomaly for a karst cave, which corresponds to the one visible on profile 9 in Figure 3 at 30 r-m. Between 10 and 17 r-m at the depth of about 1 to 4 m we can see an anomaly from loose rock.

Profile 2, shown in Figure 3, is the closest one to the Odstrzelona Cave in Kowala and shows a crack located near the opened fragment of the cave. The whole series of small hyperbolas between 5 and 35 r-m of the profile, starting at the depth of 1 m, are the result of karst processes. The anomaly at 45 r-m at the depth of 6 m and thickness of about 1 m can be assigned to a karst void, as can be the anomaly less visible at a depth about 8.5 m.

A distinct anomaly from a karst void appears on profile 3 (Fig. 3) at 10 r-m and a depth of 6.5 m. Underneath we can see poorly visible anomalies from cracks in the old quarry. Near 5 r-m at the depth of 2 m a small anomaly can be seen, which probably is also associated with karst processes. At 14 r-m of the profile one more anomaly, elongated in time with height of about 8 m, can be observed. We suggest that it originated from a karst chimney.

Profile 12 (Fig. 3) was designed in order to see if Odstrzelona Cave in Kowala continues to the north. In the first 10 r-m of the profile there are many anomalies related to cracks near the opened fragment of cave. From about 12 r-m at about 1 to 3.5 m depth, an anomaly with a similar origin appears.

The very interesting profile 9 (Fig. 3) shows without doubt four big and clearly visible anomalies. They are pictures of a karst cave with two chambers. The first one starts at 23 r-m of profile and continues for the next 11 r-m, until 34 r-m. The second one can be found at 52 r-m and is visible for 10 m. Their ceilings start at depths 3.5 m for the first one and 3 m for the second one. Measured thickness reaches up to 2.5 m. Bright anomalies below these two, at a depth of about 7.5 to 8 m and located at 25–40 r-m and 52–62 r-m, respectively, and thickness reaching up to 1.5 m are probably floors of these chambers. At the end of the profile we can see a similar anomaly to the one in profile 12. The reflector, about 8-m high, is a karst chimney.

DISCUSSION AND CONCLUSION

Comparing the quality of obtained results to echograms from a study performed by Beres et al. (2001) shows our surveys to be equally satisfactory and precise.

Due to the limitations of GPR, there are several problems with conducting measurements and their interpretation. The survey has considerable space requirements. For carrying out GPR measurements, antennas need close or even direct contact with the bedrock surface. Trees and bushes, and even cut brush, are a great obstacle. Another limitation is the depth range and resolution. Those parameters are directly connected. For greater depth penetration, the resolution is lower and the size and weight of antennas grows; for example, an 800 MHz shielded antenna has size approximately 0.4 × 0.2 m and weighs 2.6 kg, and a 250 MHz shielded antenna is about 0.8 × 0.5 m and 8 kg. If you consider an ideal bedrock for GPR measurements, such as dry limestone, for reaching deeper it

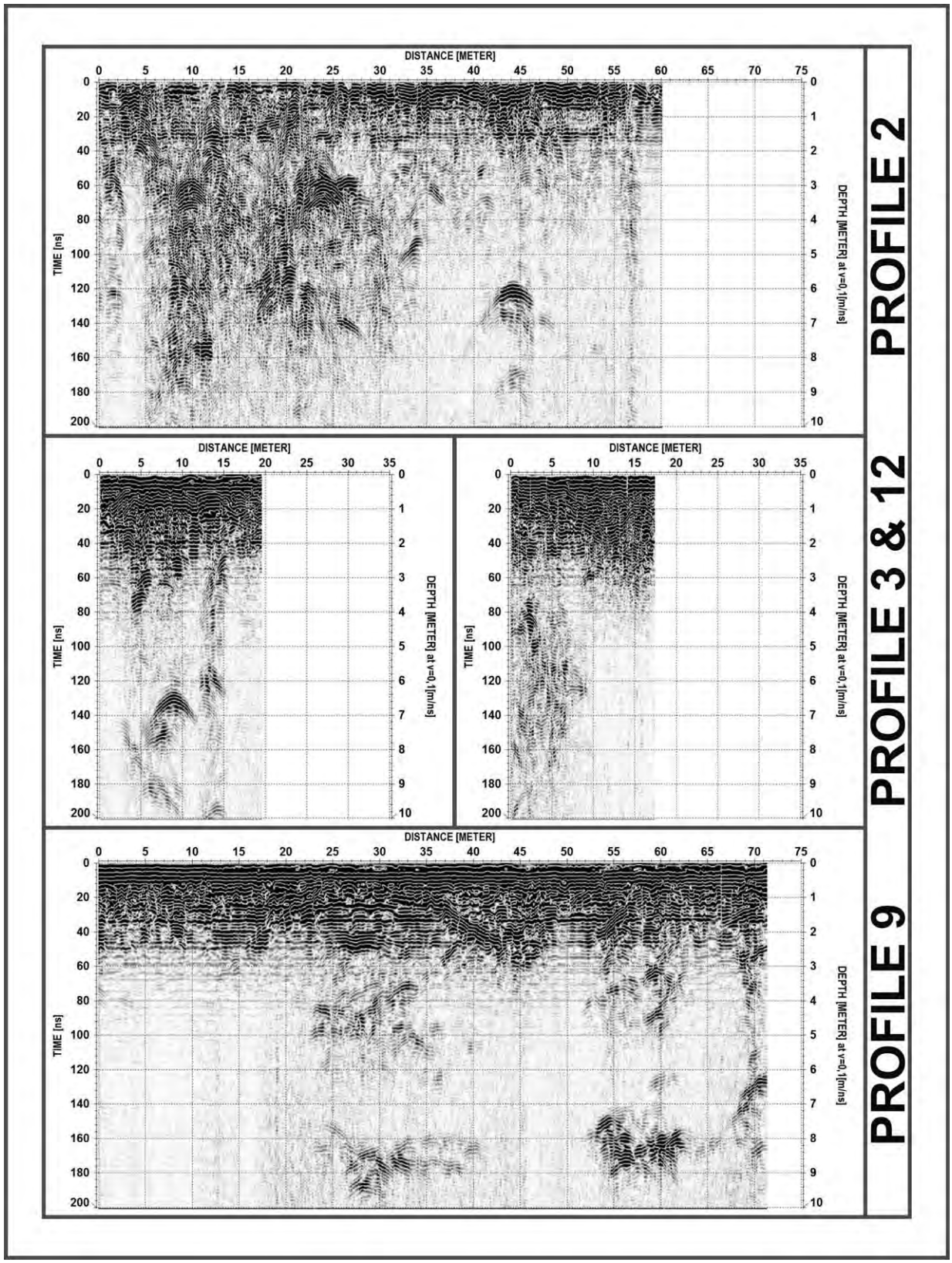

Figure 3. Echograms from profiles 2, 3, 9, and 12 containing clearly visible anomalies from karst process effects: disruption of the bedrock, as in profile 2 between 5 and 35 m, or voids, as in profile 9, which has four large anomalies, two between 23 and 34 r-w and two between 52 and 62 r-m, each pair interpreted as the ceiling and floor of a void.

is necessary to use a lower frequency, requiring a larger antenna and providing lower resolution. Use of a 250 MHz antenna gave good-quality data and proved to be the right choice. The resolution and usable depth penetration range obtained, up to 10 m, were satisfactory. The terrain covered with trees where the surveys were carried out also made that the choice of antenna frequency, size, and weight optimal. Usage of the shielded type antennas also reduced the noise, a source of which can be trees, so-called reflections in air. Before analyzing the results the authors repeatedly processed the raw data. The optimal sequence of processing was applied to all profiles. Processing all data in the same way guarantees confidence of interpretation. Only profile number 16, because of the use of an unshielded 100 MHz antenna, was processed individually. The procedures used removed unwanted noise and kept the interference in the raw data at a minimum.

Satisfactory detection of voids and cracks (e.g., Xu et al., 2010), caves, or karst objects is possible by using only GPR. There are many published examples of such exploratory works (e.g., Chamberlain et al., 2000). For the purposes of a full inventory of a cave it is necessary to perform a comprehensive study, including the use of other geophysical methods and a precise geodetic grid. Unfortunately, the topography and the dense forest of the old quarry made it impossible to conduct such a survey. Complementary use of other methods such as microgravity (Beres et. al, 2001) or a high-resolution engineering seismic survey would give more precise data about the depth and size of the cave. Unfortunately, these methods are much more expensive and time-consuming. Despite the use of only one geophysical method, information about voids and karst that affect the investigated limestones gave a more comprehensive picture for further exploration of the area of the closed quarry. Use of only one method always provides ambiguous results. However, precise measurements and thought-out profiles lines, good acquisition parameters, and optimal processing of raw data minimize the impact of the lack of a second method.

ACKNOWLEDGEMENTS

We express a special thanks to the mayor of municipality Sitkówka-Nowiny, Mr. Stanisław Barycki, who gave permission for the publication of the results of the surveys. We would like to thank the Assoc. Prof. Sally Sutton from Colorado State University, United States, and our colleague from AGH University of Science and Technology in Krakow, Poland, Ph.D. Eng. Kamila Wawrzyniak-Guz for support during the writing of this paper. Additional thanks are expressed to the reviewers for their comments that helped improve the manuscript and to Mr. Maciej Grzelak for access to the photo.

Measurements were conducted by M.Sc. Eng. Mikołaj Łyskowski under the supervision of Ph.D. Eng. Jerzy Ziętek. Presentation and analysis of the surveys results were made by M.Sc. Eng. Mikołaj Łyskowski and M.Sc. Eng. Ewelina Mazurek, who are Ph.D. students at AGH University of Science and Technology in Krakow in the Department of Geophysics.

REFERENCES

Annan, A.P., 2001, Ground Penetrating Radar Workshop Notes: Mississauga, Ontario, Sensors & Software Inc.

Beres, M., Luetscher, M., and Olivier, R., 2001, Integration of ground-penetrating radar and microgravimetric methods to map shallow caves: Journal of Applied Geophysics, v. 46, p. 249–262. doi:10.1016/S0926-9851(01)00042-8.

Chamberlain, A.T., Sellers, W., Proctor, C., and Coard, R., 2000, Cave detection in limestone using ground penetrating radar: Journal of Archaeological Science, v. 27, p. 957–964. doi:10.1006/jasc.1999.0525.

Doolittle, J.A., and Collins, M.E., 1998, A comparison of EM induction and GPR methods in areas of karst, Geoderma, v. 85, p. 83–102. doi:10.1016/S0016-7061(98)00012-3.

Grzelak, M., 2012, Jaskinie w regionie świętokrzyskim: Jaskinie, v. 1, no. 66, p. 25–28.

Karczewski, J., Ortyl, Ł., and Pasternak, M., 2011, Zarys metody georadarowej, Wydanie drugie poprawione i rozszerzone: Krakow, AGH University of Science and Technology Press, 346 p.

Kondracki, J., 2011, Geografia regionalna Polski: Warsaw, Wydawnictwo Naukowe PWN 468 p.

Łyskowski, M., and Mazurek, E., 2013. Analiza konsekwencji doboru nieodpowiedniej prędkości propagacji fali elektromagnetycznej w trakcie interpretacji inżynierskich pomiarów metodą georadarową (English abstract): Logistyka 2013 nr 4, suplement: CD Logistyka – nauka, p. 330–336.

MALÅ Geoscience, 2009, ProEx – Professional Explorer Control Unit. Operating Manual V. 2.0.

OYO, 1988, OYO Georadar I Manual: Tsukuba, Japan, Oyo Corporation, 50 p.

Reynolds, J.M., 1997, An Introduction to Applied and Environmental Geophysics: West Sussex, England, John Wiley & Sons, 796 p.

SSS, 2009, Reflexw Manual, User Guide: Karlsruhe, Germany, Sandmeier Scientific Software.

Urban, J., 2007, Permian to Triassic paleokarst of the Świętokrzyskie (Holy Cross) Mts., Central Poland: Geologia (Krakow), v. 33, no. 1, p. 5–50.

Xu, Xingxin, Zeng, Qiaosong, Li, Dong, Wu, Jin, Wu, Xiangan, and Shen, Jinyin, 2010, GPR detection of several common subsurface voids inside dikes and dams: Engineering Geology, v. 111, p. 31–42. doi:10.1016/j.enggeo.2009.12.001.

R. Zlot and M. Bosse – Three-dimensional mobile mapping of caves. *Journal of Cave and Karst Studies,* v. 76, no. 3, p. 191–206. DOI: 10.4311/2012EX0287

THREE-DIMENSIONAL MOBILE MAPPING OF CAVES

ROBERT ZLOT* AND MICHAEL BOSSE
Autonomous Systems, CSIRO, Brisbane, Australia

Abstract: Existing methods of cave survey are time consuming and require significantly more time than naturally moving through the cave. The efficiency of these methods, even in the case of state-of-the-art laser-scanning technology, is fundamentally limited by the requirement that measurements be taken at static locations. We present a mobile approach to cave mapping, in which a lightweight 3D laser scanner is carried by a single operator while walking, climbing, or crawling through a cave at a natural pace. The mobility of the system means that it is straightforward and efficient to generate a high-resolution 3D map consisting of millions of points in almost any environment a human can reach. We present results demonstrating the technology in two cave systems located in different parts of Australia, what we believe are the first instances of mobile LiDAR mapping being utilized in natural caves.

INTRODUCTION

Traditional methods of cave mapping involve manual measurements of range and bearing between a sequence of stations typically spaced up to a few tens of meters apart (Warild, 2007, chap. 10; Kershaw, 2012). The most common instruments for measuring bearing are compass and clinometer, while for range, a fiberglass tape measure or topofil are commonly used. Detail is obtained through hand-drawn sketches of the local cave passage rendered at some or all of the stations, as well as left-right-up-down distance measurements to the walls, roof, and floor. The data are later merged into a cave map based on the registered survey station locations, often using computer software packages. These mapping techniques are not only highly time consuming, but rely on manual acquisition and recording of the measurements and sketches, which are prone to human errors including instrument-sighting error, station errors, and transcription errors (Hunter, 2010). Integrated systems such as DistoX (Heeb, 2008) can eliminate some of the manual sources of error by logging measurements directly from electronic instruments to a handheld mobile device, rather than paper. Recently, handheld laser distance meters have been increasingly employed instead of tape to acquire range measurements between survey stations (Dryjanskii, 2010). Theodolite systems have long been utilized in some instances (Middleton, 1991; Davis and Land, 2006; Rüther et al., 2009), but are considered too cumbersome or impractical for many cave survey applications due to their size, fragility, and weight (Warild, 2007; Slavova, 2012).

One of the most compelling recent examples of traditional cave surveying is the Jenolan Caves Survey Project (James et al., 2009). This project produced a tremendously comprehensive 3D model of the caves using data primarily acquired with total station and laser distance measurements. To improve the resolution of the model in areas with large voids, distance measurements were taken in twelve-point cross sections spaced at 10 m intervals. While the resulting model is highly detailed and accurate, an extraordinary amount of surveying and data processing effort was invested in the multi-year project, which was carried out between 1987 and 2005.

In recent years, terrestrial laser scanning, or LiDAR, technology has been used to create high-resolution 3D maps of a number of caves (e.g., Rüther et al., 2009; McIntire, 2010; Sadier et al., 2012). Terrestrial scanners are typically mounted on a stationary tripod and acquire millions of precise range measurements of the surfaces surrounding the station over a period of a few minutes. Data from multiple stations can be combined if there is sufficient overlap between the scanned surfaces, though in practice it is more common to measure the station position and orientation using standard surveying techniques, or to place known targets into the scans (Rüther et al., 2009). Despite the high quality of the data resulting from terrestrial LiDAR, the technique has seen relatively limited use in caves, most likely due to the high cost of the scanners, as well as the size, weight, and fragility of the equipment making it difficult to transport through difficult terrain and tight squeezes. In addition, the often complex geometry of caves may prescribe that a large number of scans be acquired to achieve sufficient coverage and avoid shadows due to occlusion. McIntire (2010) reports, "the most time-consuming part of the scan was moving from station to station and shooting in the targets. ... Every setup was a challenge to determine where the previous and upcoming scans' shadows would occur and locating the best combination of scan coverage and setup efficiency."

Mobile mapping is a technique whereby measurements of the environment are acquired while moving continuously through it. Commercial solutions exist that acquire LiDAR scans from moving aircraft, watercraft, or street vehicles (Petrie, 2010); however, these systems typically rely on expensive, bulky equipment and on global navigation satellite systems (GNSS) such as GPS for positioning. Mining applications have provided a market for transitioning mobile mapping technology underground. Due to the

* Corresponding Author: Robert.Zlot@csiro.au

difficulty of operating without GNSS coverage, underground mine mapping has largely remained a research problem (Nüchter et al., 2004; Morris et al., 2006; Fairfield et al., 2010), and, with the exception of other recent work we have done based on technology similar to what is presented in this paper (Zlot and Bosse, 2014), no systems of which we are aware have been demonstrated to be capable of efficiently mapping a large-scale mine in 3D. In any case, the platforms that have been fielded have been mounted on wheeled vehicles that rely on the existence of roadways in the mine and would be unsuitable for most natural caves. Indoor mobile mapping technology could also be considered relevant to mapping caves, but existing systems involve wheeled platforms (e.g., Canter and Stott, 2011) or require planar structures in the environment such as walls, floors, and ceilings (Liu et al., 2010).

To address some of the limitations of existing mobile mapping systems, we have developed portable LiDAR-based mobile mapping technology that does not require external positioning or artificial infrastructure, is relatively inexpensive, and can easily be carried by hand by a single operator through the challenging environments presented by natural caves (Fig. 1). The raw data acquired are converted by software into globally consistent and metrically accurate 3D point clouds or surface models consisting of millions of points or triangles, as well as an estimate of the sensor trajectory through the cave. The combination of mobility and maneuverability facilitates efficient data acquisition, because a cave can be mapped in the time it takes to walk, crawl, squeeze, or climb through it; a high degree of coverage, because shadows due to occlusion are avoided by virtue of the motion; and versatility, because most terrains through which a human can traverse can be mapped. In addition, the system is fully automated, eliminating the human errors inherent to manual surveying techniques, despite requiring nearly zero training time. Easy acquisition of dense and accurate point cloud data can provide models useful not only for navigation, but also for a variety of scientific applications previously not possible or economical.

Our handheld mobile mapping system has been deployed in several cave and underground mine sites around the world. To our knowledge, our body of work represents the first instance of mobile mapping in non-submerged caves (Stone et al. (2000) and Gary et al. (2008) describe mapping underwater voids using sonar), and a significantly more efficient and complete method of surveying caves compared to the state-of-the-art. After describing the equipment and its use, we present results obtained from extensive scanning of significant parts of the Jenolan Caves and Koonalda Cave in Australia.

EQUIPMENT AND METHODS

The key enablers of our mobile cave mapping technology are a lightweight handheld laser-scanning device coupled with data processing software capable of accurately estimating the position and orientation of the scanner over time as it is moved through the environment. The scanner measures tens of thousands of ranges per second from the sensor origin to points on various physical surfaces using narrow infrared laser pulses. Given an accurate estimate of the scanner's motion, the set of range measurements can be projected into (x,y,z) points in a common coordinate frame, thereby generating a consistent point cloud model of the cave and surrounds.

THE ZEBEDEE MOBILE MAPPING SYSTEM

Zebedee (Fig. 1) is a handheld 3D mobile mapping system consisting of a 2D laser scanner mounted on a spring (Bosse et al., 2012). The infrared laser scanner is a Hokuyo UTM-30LX, which, at 370 g, is light enough to be carried by hand. The UTM-30LX emits 905 nm laser pulses at a high frequency that reflect off surfaces in the environment and return to the sensor. The scanner internally converts the signal to a range measurement based on the time of flight. Within the scanner, the laser pulses are spread across a plane by a spinning mirror rotating at 40 Hz (100 Hz in the newest Zebedee hardware). Measurements are acquired within a field of view of 270° at quarter-degree angular resolution, resulting in 43,200 points per second. The maximum range of the scanner is approximately 35 m in the cave environment and surfaces beyond that range are not registered as measurements. The range precision is typically 1 to 3 cm, depending on the distance and incidence angle to the surface, as well as surface reflectivity.

A unique design feature of Zebedee is the spring on which the laser scanner is mounted. The purpose of the spring is to passively convert the natural motion of the operator carrying the device into rotational motion of the scanner. The non-deterministic, loosely swaying motion of the scanner typically results in a 150 to 180° out-of-scan-plane field of view. Sweeping the device in this manner effectively extends the inherent two-dimensional field of view of the Hokuyo scanner into a three-dimensional view of the environment acquired roughly every second.

A MicroStrain 3DM-GX3 industrial-grade microelectromechanical (MEMS) inertial measurement unit (IMU) is mounted beneath the scanner, and provides measurements of angular velocities and linear accelerations. The inertial measurements are used by the processing software, along with the LiDAR data, to estimate the scanner trajectory. The IMU also contains a three-axis magnetometer that can further aid the solution by constraining the absolute heading in environments with minimal magnetic interference, which is often the case in caves.

In addition to the handheld device, the Zebedee hardware system includes a small laptop for operating the sensors and logging data. A lithium-ion battery pack powers both the sensors and laptop. Batteries of various capacities are available; a 1 kg battery provides more than ten hours of operation. The laptop, power pack, and spare

Figure 1. (a) Mapping Koonalda Cave with the Zebedee 3D mapping system. The scanning device is held in the operator's right hand, with a battery pack and small laptop for recording data carried in a backpack. (b) The components of the Zebedee system.

batteries are typically carried in a backpack, which can easily accommodate other tools and supplies. Operation can also be fully controlled and monitored via a smartphone interface, eliminating the need to access the laptop between datasets. To extend the operator's reach, a camera monopod can be connected to the bottom of the Zebedee handle via a standard ¼-inch tripod screw socket.

Data Acquisition

Data collection with Zebedee is a continuous procedure, but can be broken down into a number of manageable datasets, which are typically in the range of 10 to 90 minutes in duration. Acquiring data for an individual dataset involves powering up the equipment, starting the logging software using a web browser on a laptop or mobile device, picking up the scanning device, following a desired path, then putting down the device and terminating the logging process. If the objective is to merge multiple datasets into a global model, some repeated coverage is required between the scanned areas in order for the processing software to automatically detect the matching areas and align the point clouds. Typically a

few meters of overlapping trajectory is sufficient. If multiple Zebedee units are available, multiple operators can simultaneously collect data in different areas to be combined later into a common map. The data acquisition software uses the open-source Robot Operating System (ROS) middleware platform, and stores the raw data in ROS-native .bag files at a rate of approximately 100 MB every 7.5 minutes. The data processing software is run post-acquisition and outputs the 3D maps and trajectory followed in standard point cloud file formats, including .laz (compressed .las) and .ply. The size of a point-cloud file stored in .laz format is approximately 1 MB for every 325,000 points, or about 7.75 MB per minute of data, so a typical cave model is expected to be anywhere in the range of tens of megabytes to a gigabyte in size.

DATA PROCESSING

The very nature of mobile mapping involves a sensor platform that is continuously in motion as measurements are acquired. However, in order to generate a consistent map, all of the point measurements are required to be transformed into a common coordinate frame. Therefore, a mapping solution must be able to accurately estimate the trajectory of the laser scanner, a continuous function specifying the scanner's 3D position and orientation at all times during acquisition. Although there is no external positioning system available, the trajectory can be estimated based entirely on the LiDAR and inertial measurements. The challenge of concurrently estimating the trajectory of a sensor and a map of the environment is a fundamental problem known in the robotics literature as simultaneous localization and mapping, or SLAM (Durrant-Whyte and Bailey, 2006).

An essential requirement of SLAM solutions is the observation of features in the environment multiple times. As a simplified example of how motion can be estimated through external observations, imagine taking a single-point measurement of the distance to a wall. An initial measurement of 5 m is recorded, followed by a measurement of 3 m taken at a slightly later time. Assuming that the two measurements can be associated with the same physical surface, one can infer from these observations that in this time the sensor has moved 2 m in the direction perpendicular to the wall. By aggregating thousands of similar measurements of matched surfaces with various orientations in the observed environment, the 3D motion of the sensor can be estimated to a high degree of precision.

The algorithmic framework underlying the Zebedee trajectory estimation solution is based on a generalization of the above principle (Bosse et al., 2012). As the laser scanner swings about on the spring, it sweeps through its field of view, capturing a 3D scan of the local environment roughly once per second. Within a time window of a few seconds, there is a considerable amount of overlap between the parts of the environment scanned in each sensor sweep. Surface elements, which contain a position and normal direction, are extracted from local patches of scan points from within these sweeps. By matching pairs of surface elements acquired at distinct times, the trajectory between those samples is determined by the relation between the surface geometries. The inertial and magnetometer measurements are used to generate further constraints on the scanner trajectory over these short time windows. An optimization routine solves for the trajectory that minimizes the differences among the various constraints starting from an initial estimate derived from the inertial measurements. By shifting the time window at each time step, the trajectory of the scanner is incrementally generated as more data are captured.

As the trajectory length increases, small errors can build up, resulting in a drift of the solution over time. While these errors tend to be small, not addressing them would not only result in global inaccuracies, but also in point clouds with apparent fuzziness or doubling of surfaces due to multiple images of a surface observed at different times. There are also situations where there is a higher risk that large local errors could be introduced into the solution, such as very tight squeezes where the scanner has a limited view of the environment. The SLAM algorithm used for estimating the initial scanner trajectory can also be used to apply corrections to the trajectory by optimizing all of the data over an entire dataset rather than over a few-second time window. This non-rigid global optimization step applies small corrections along the trajectory that result in consistent, registered surfaces throughout the map. This process is somewhat analogous to applying loop closure constraints in a traditional survey. However, a key difference in this solution is that the loop closures do not occur at discrete stations (as there are no stations), but rather are detected automatically and continuously as parts of the environment are rescanned.

If the buildup of errors is relatively large (for example, in a large dataset), a place recognition algorithm can improve the input trajectory provided to the global optimization by identifying locations in the environment that have been scanned multiple times (Bosse and Zlot, 2013). Place recognition also provides the facility to automatically align multiple maps together, provided there is sufficient overlap, typically a few meters, among them. This capability is useful for merging data collected at different times or when multiple operators are scanning a cave system simultaneously.

The entire data processing pipeline is run automatically: The raw LiDAR and inertial measurement streams are taken as input, and a trajectory and 3D point cloud are generated as output. The processing time required to compute a solution is less than the time spent collecting the data; therefore it is possible to build a map in real-time during acquisition. More detailed technical descriptions of the algorithms are available in previous publications (Bosse et al., 2012; Bosse and Zlot, 2013; Zlot and Bosse, 2014).

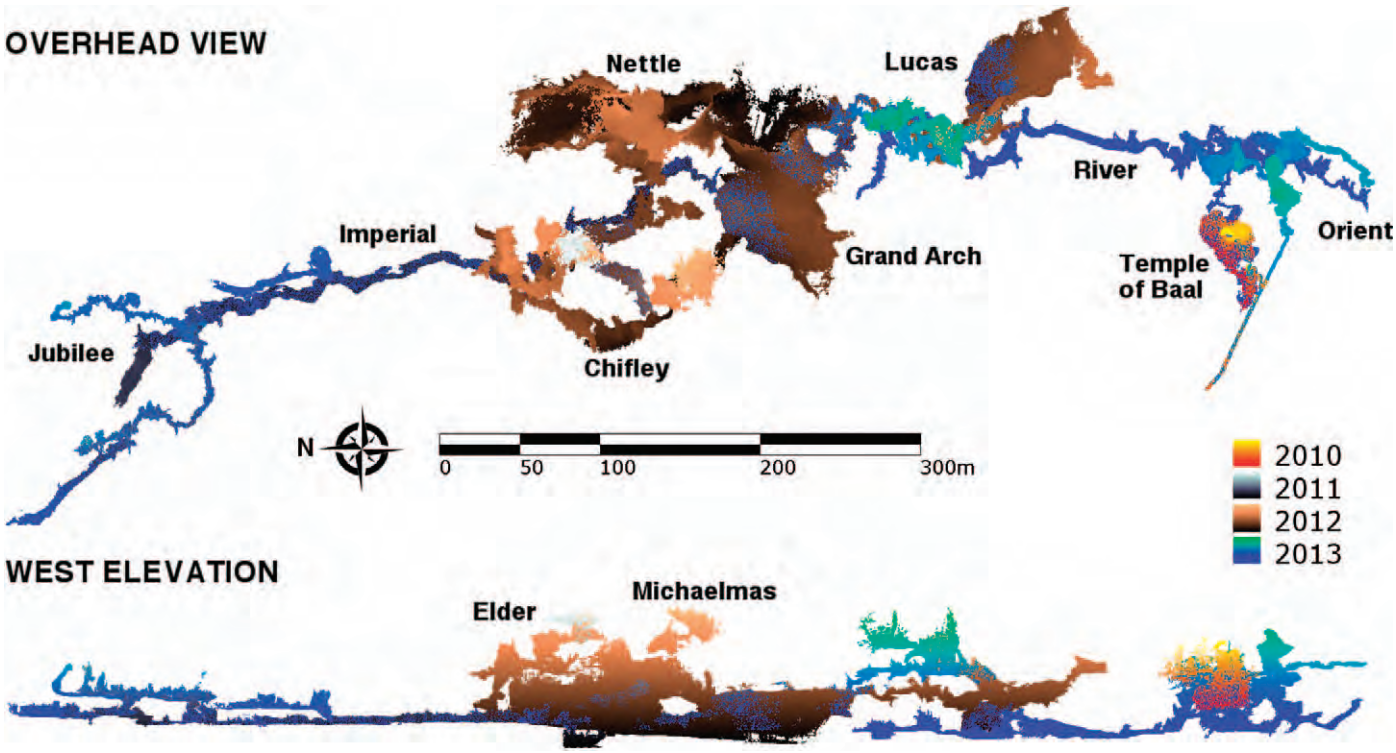

Figure 2. Three-dimensional point cloud map of the Jenolan Caves projected as overhead and elevation views. The map is generated from 15.5 hours of LiDAR data collected over four visits in 2010 (with Hannibal device), 2011 (Zebedee device), 2012 (Zebedee), and 2013 (Zebedee). A different colormap is used to color data from each trip according to elevation as indicated on the right side of the image. The full resolution point cloud from these datasets consists of over 2.7 billion points. Significant caves are labeled.

Results

We have deployed our 3D mapping systems in several caves around the world. Here we describe the most significant undertakings and results from the Jenolan Caves and Koonalda Cave in Australia.

Jenolan Caves

The Jenolan Caves are located in New South Wales, approximately 110 km west of Sydney. A recent study has dated some areas of the caves to be 340 million years old, making Jenolan the oldest complex cave system accessible to humans (Osborne et al., 2006). The Jenolan system consists of a number of interconnected caves generally running in a north–south direction and at various levels vertically (Fig. 2), with several of the entrances located at the Grand Arch. The caves extending a kilometer to the south of the Grand Arch contain several large chambers connected by a series of passages, the longest of which includes an underground river flowing through a passage below Lucas, Temple of Baal, and Orient Caves. To the north of the Grand Arch, the caves are generally contsist of long passages and relatively narrower local voids. A wide variety of attractive speleothems are present throughout many of the caves. The Jenolan Caves are a popular tourist attraction, and a number of the caves have been converted into show caves with paved pathways, stairs, handrails, and lighting. Other caves have generally been left in their natural state, containing rugged terrain and tight squeezes.

Our initial involvement in mapping the caves was to support research being conducted by researchers at the Australian Nuclear Science and Technology Organization (ANSTO). ANSTO is investigating the use of speleothem composition and growth patterns for interpreting the palaeo-climatic record through measurement and analysis of isotopes (Waring et al., 2009). Various sensors have been placed in several of the caves to monitor the composition of gases, drip water, and air flow. Large-scale, high-resolution 3D volumetric models are necessary to more accurately model air flow and growth patterns through the cave system.

Our first mapping trip to the Jenolan Caves took place over two days in September 2010. At the time, the Zebedee system was in a very early stage of development and was not ready for deployment. However, the initial requirements specifically involved mapping several of the tourist show caves, which contain paved pathways and stairs. Therefore, we constructed a wheeled mobile-mapping platform, called Hannibal, consisting of hardware that

Figure 3. The Hannibal mapping cart in operation in Lucas Cave, Jenolan.

had previously been developed for use on vehicles. This system used a motorized platform to spin a 2D laser scanner at a constant rate (Bosse and Zlot, 2009). The scanner, a SICK LMS291, measures ranges in a plane, similar to the Hokuyo, with several key differences in the specification, most notably a significantly increased mass at 4.5 kg. In addition, the LMS291 scans at 75 Hz, producing 180 points per scan within a 180° angular range, and has with an 80 m maximum range. By continuously rotating the scanner about the center scan ray at 30 rpm, a hemispherical 3D field of view containing 13,500 points is obtained once per second. The spinning LiDAR system is mounted to an upright, two-wheeled furniture cart 1.3 m in height and 54 cm wide (Fig. 3). A MicroStrain 3DM-GX2 IMU is rigidly mounted to the cart, providing measurements of angular velocity and linear acceleration at 100 Hz used to provide additional reliability as well as stabilization of pitch and roll angles with respect to gravity. At the bottom end of the cart are three racks storing sealed lead-acid batteries, electronics, and a small netbook for controlling the sensors and data logging. As the system's overall mass is approximately 60 kg, a considerable physical effort is required, often by two people, to move the cart up and down long stairways. Data acquired from Hannibal are processed with the same core software used for Zebedee data.

Over the course of two days, we collected data over a path length of more than 9 km within Chifley, Imperial, Lucas, Temple of Baal, and Orient Caves, as well as several areas of the surface above and between the entrances of the caves. The total acquisition time was just under ten hours at an average speed of 0.7 km/h inside the caves. In a very small number of areas the footpaths or stairways became too narrow, and Hannibal was briefly raised and carried by two or more people for a few meters.

A number of stations from previous surveys (James et al., 2009) are marked in the ground surface of the caves using stainless steel disks. We therefore elected to incorporate the station coordinates into our solution for added reliability and georeferencing. To do so, we simply

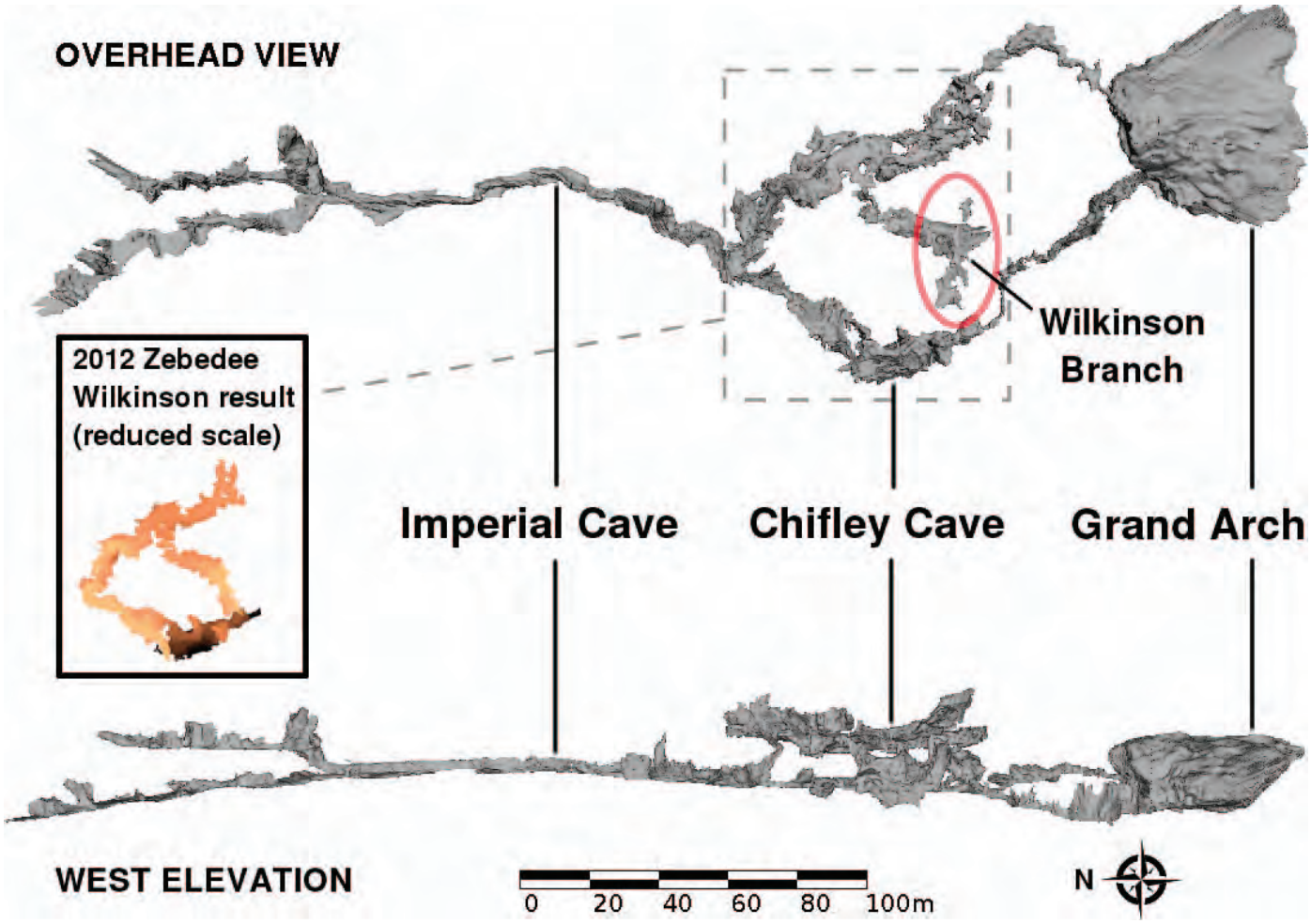

Figure 4. Detailed 3D watertight surface model of Chifley and Imperial Caves generated from LiDAR data acquired from the Hannibal platform. Chifley is a C-shaped passage at a level approximately 10 m above Imperial. While scanning the Wilkinson Branch, data were lost for about 30 seconds due to a USB cable becoming unplugged. The data loss resulted in a kink in the trajectory, indicated by the red circle. Rescanning of this section with Zebedee in the 2012 visit has produced a corrected model of this area (see callout box).

stopped the cart directly above any survey markers seen on the ground, leaving the equipment stationary for approximately ten seconds. These events are then straightforward to identify later in the data stream as stationary points in the trajectory. A matching step found a geometric transformation between the trajectory and the ground control points, which were then used as loose constraints within the non-rigid optimization algorithm. Due to its continuous motion, it is not as straightforward to stop Zebedee at survey stations. We are currently experimenting with methods to allow us to automatically detect when we are at one of these points to enable georeferencing of Zebedee data in a similar manner.

In addition to the point cloud models produced, watertight surface models were required for use in the researchers' air flow analysis. Software for generating 3D surface models from the point clouds was developed for this purpose (Holenstein et al., 2011). One reality of mapping with this equipment in confined spaces is that it is inevitable that members of the mapping team will occasionally need to enter the scanner's field of view, thereby introducing spurious points into the point cloud. These spurious points can be removed during surface reconstruction by modeling each measurement as a space-carving ray. If a ray successfully passes through the location of a point at other times, then the point can be disregarded as coming from a moving object. One disadvantage of converting the point cloud data to a smooth surface in this manner is that much of the fine structure of the cave features is lost in the surface model. An example surface reconstruction from Chifley and Imperial caves is illustrated in Figure 4. Detailed watertight surface models can be fabricated into physical scale models using 3D printing technology (Baselgia et al., 2014).

Although successful, clearly the size, weight, and wheeled base of Hannibal suggest that it is unlikely to be

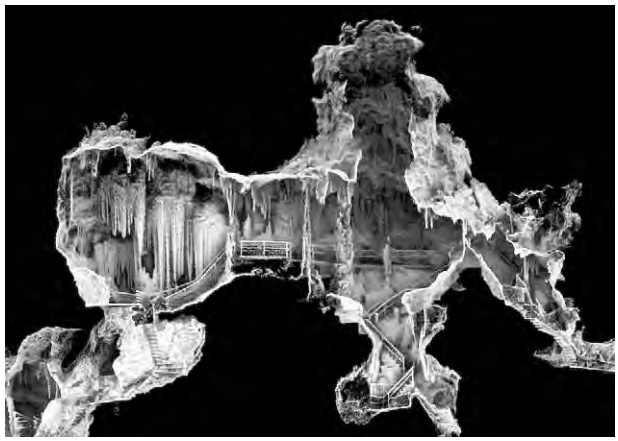

Figure 5. Point cloud of a section of Orient Cave. Some of the wall surfaces have been cut away to reveal natural formations, platforms, staircases, and handrails.

appropriate for the vast majority of natural caves. However, this initial deployment only required access to paved pathways and stairs in show caves, which, with some physical effort, is achievable. The platform also served as a proof-of-concept for LiDAR-based mobile mapping in natural caves and further motivated the development of the more practical Zebedee system.

Subsequent trips to the Jenolan Caves, with Zebedee systems, occurred in August 2011, November 2012, and May 2013. In 2011, several caves were scanned, including Orient, River, Pool of Cerberus, Lucas, Imperial, Jubilee, and Elder caves. In 2012, Chifley, Imperial, Nettle, Elder, and Michaelmas caves were mapped, as well as several kilometers of paths on the surface outside and above the caves. In 2013, Orient, Baal, Lucas, River, and Jubilee caves were scanned. On the latter two trips, multiple Zebedee units were available, allowing different areas to be mapped simultaneously and later automatically combined by the processing software. Figure 2 shows a combined map merging a subset of the data from the 2011–2013 scans of Jenolan; some of older, redundant data and a few areas on the surface have been excluded. Data from the Temple of Baal cave scanned with the Hannibal cart system in 2010 are also included in the figure, as the height of the main chamber is beyond the maximum range of Zebedee's laser scanner. The result illustrated is based only on the LiDAR data and does not incorporate any ground control points from previous surveys. A close-up of a section of the Orient Cave point cloud generated with the Zebedee system is presented in Figure 5.

Key data collection statistics for the model presented in Figure 2 are presented in Table 1. Overall, the map includes about 15.5 hours of cave scanning, collected over 17.1 km of traverse. It should also be noted that there was a higher than required degree of overlap between the datasets, so the total scanning time and trajectory length could be significantly reduced while still achieving the same coverage. We estimate that two operators familiar with the cave layout could cover the same area in a single day. Within the show caves, the average rate of traverse using Zebedee was 1.7 km/h, approximately 2.5 times the average speed achievable with Hannibal.

The Zebedee system is not limited to tourist show caves containing pathways, platforms, and stairs. Even in the case of the show caves, many sections could not have been navigated with Hannibal due to steep stairs, ladders, narrow passageways, and rough or muddy terrain. In addition, the terrain in other caves that were covered is more natural. For example, Elder and Michaelmas Caves primarily consist of small chambers connected by narrow passages and squeezes. A detailed view of the 3D model of Elder Cave is presented in Figure 6. The terrain in Elder Cave is relatively rugged, requiring scrambling, squeezing, and climbing to traverse it. The cave generally runs vertically from a sinkhole opening at the surface down to a connection with Imperial Cave. Our 2011 traverse followed this route, including scanning while abseiling down the sinkhole. In 2012, the route started from below, ascending to the sinkhole, and then back down to Imperial along a slightly different path, taking about two hours in total. At a few of the most challenging squeezes and climbs, the Zebedee unit was passed through the opening to a second person to allow the primary operator use of both hands. These hand-offs could be completed without interrupting the datastream, thus there are no breaks in the map. The point cloud model of Elder Cave can also been seen as part of the overall model of the Jenolan Caves in Figure 2, where it matches with Imperial Cave at the bottom and the sinkhole area as scanned from the surface above. The results from Elder Cave highlight the versatility

Table 1. Key statistics from Jenolan Caves datasets included in the model shown in Figure 2.

Trip Year	Total Path[a], km	Cave Path[b], km	Cave Time[b], h:min
2010	0.4	0.4	0:49
2011	2.2	2.2	1:33
2012	11.4	5.3	4:56
2013	11.4	9.1	8:08
Total	25.5	17.1	15:26

[a] Total Path indicates trajectory length combining both cave and exterior datasets.
[b] Cave Path and Cave Time refer to the trajectory length and scanning duration within the caves (excluding exterior datasets).

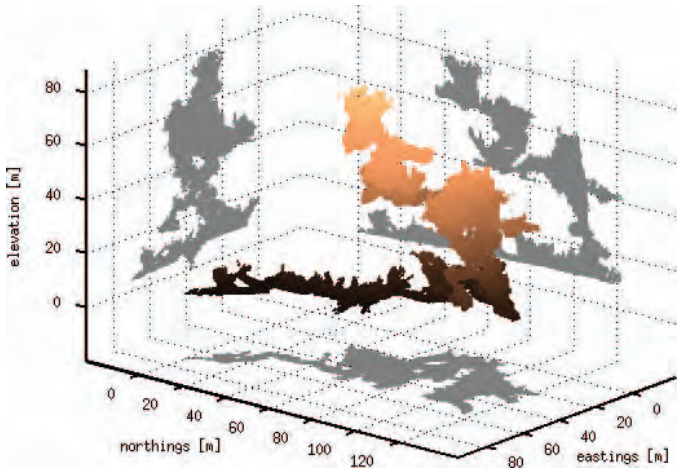

Figure 6. Point cloud map of Elder Cave generated from the 2012 data. The 3D representation at center is colored by height. Projections onto the axis-aligned planes are shown in grey. At the uppermost region of the model is the sinkhole opening to the surface. The long passage at the bottom is part of Imperial Cave. The actual resolution of the data is higher than the resolution of this display.

and robustness of the system in mapping more challenging cave environments.

The Jenolan Caves had previously been the subject of extensive surveys using more traditional methods. In Figure 7, the Zebedee-generated model is compared to a map completed in 1925 by Oliver Trickett (Middleton, 1991) and with 59 survey stations from the more recent Jenolan Caves Survey Project (James et al., 2009). The layout of the caves is generally in agreement with the previous surveys, though there are some clear misalignments between the outlines. The most obvious discrepancy can be seen on the left side of the image, where accumulating yaw drift along a 500 m branch of Imperial and Jubilee Caves has introduced a large error. In this case, one of the datasets covering this section of Imperial was collected in 2011, using an older version of the acquisition software in which no magnetometer data was recorded and timing information was less accurate. As a result, there is increased drift error, and without an opportunity to close the traverse, there are no constraints to correct the error. We plan to rescan this section in an upcoming trip, which we expect would improve this area of the model. Elsewhere in the cave system, the differences are of a much smaller magnitude, and the fact that the majority of the survey station markers fall within the Zebedee map outline show that the models agree to within a few meters. In general, the Zebedee maps are locally accurate, and it is primarily over large open traverses that the relative error can become significant. Although the absolute accuracy of the traditional surveys appear to be superior, the advantages of the Zebedee system are that the results can be produced much more efficiently, within a day or two for Jenolan; automatically, as the required operator expertise is minimal; and at a much higher resolution, billions of measurements rather than hundreds or thousands.

The drift error apparent in the branch through Imperial to Jubilee Cave in Figure 7 is indicative of potential system performance in situations where the only way to survey a cave or passage is by following a long, open traverse (i.e., where it is not possible to close a loop). We can quantify the drift by comparing the open-loop trajectory from the first phase of processing to the trajectory from the final optimized model in places where there are loops available. The analysis is carried out by calculating the difference between fixed-length segments of the open and closed trajectories of the Zebedee handle (which reflects the distance the operator has walked rather than the distance the laser has moved), by first aligning the segments at the start and then recording the positional error accumulated by the end. The root-mean-square (RMS) errors are plotted as a function of traverse length in Figure 8. The observed RMS errors grow linearly with distance, at a rate of 2 to 5 percent of distance traveled. Inaccuracy in heading is the largest contributing source of error. Two of the datasets, Lucas and Mons Meg, exhibit relatively larger error growth rates, possibly due to the nature of the environments. Note that the same analysis carried out for the laser scanner trajectory rather than the handle trajectory results in drift rates of around two-thirds of a percent of distance traveled. The performance of the SLAM algorithm depends largely on the amount and type of 3D structure present. This behavior is somewhat different than in the case of traditional survey methods, where the accuracy depends more heavily on the equipment used and the surveyor's skill.

Koonalda Cave

Koonalda Cave is an archaeologically significant cave in the remote Nullarbor Plain in South Australia. The cave consists of two large interconnected chambers on two different levels (Fig. 9). The upper chamber is a fairly linear passage about 250 m in length and 15 to 30 m wide. The ceiling is domed, with a typical height ranging between 4 and 20 m, and the floor contains many rockpiles primarily due to ceiling collapse. The lower chamber is T-shaped, with one major section running north–south and another east–west, and it contains several small lakes. The ceilings are generally higher than in the upper chamber, typically ranging between 10 and 30 m. At their main junction, the lower chamber's floor is only a few meters below the upper chamber's, but ceiling collapse in the upper chamber has resulted in much of its floor being raised nearly 20-m higher. The western end of the lower chamber contains a lake with a 23 m high roof, near the top of which a small balcony connects to the upper chamber through a narrow squeeze. The entry to Koonalda Cave is at the bottom of a 20 m deep sinkhole, which has an opening to the surface of approximately 60 m by 35 m.

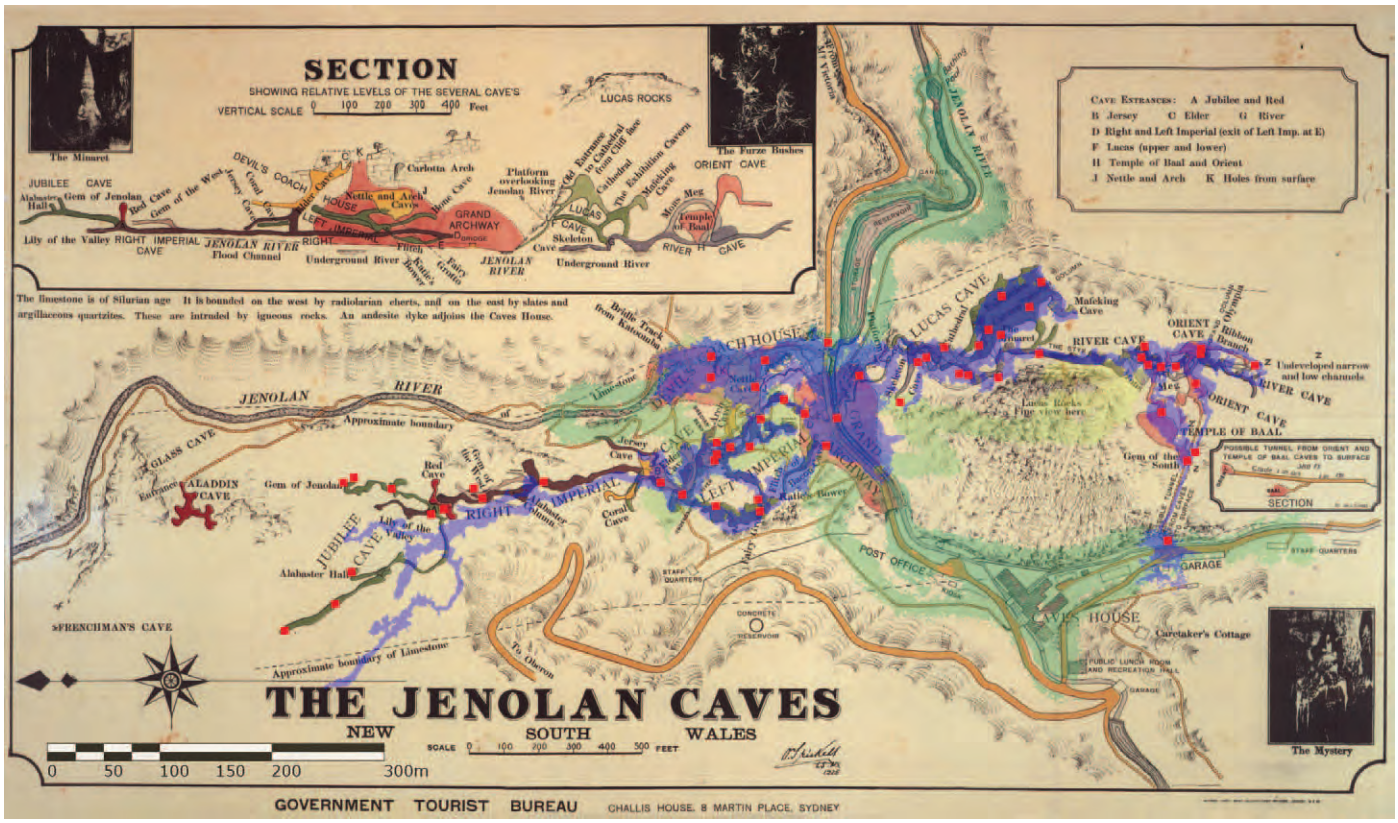

Figure 7. Comparison of Jenolan results with previous surveys. The Zebedee model is shaded in blue (caves) and green (exterior) and overlaid on the map produced by Trickett (1925). The red spots denote 59 survey stations from the Jenolan Caves Survey Project (1987–2005). The Zebedee trajectory has been rigidly aligned with the survey stations using a robust Iterative Closest Point algorithm, and the survey stations have been aligned to the Trickett map manually. The registration between the survey stations and the Zebedee trajectory has been applied using a rigid model to ensure that the presented Zebedee map is based on independent measurements only.

Unlike many of the caves at Jenolan, Koonalda Cave does not contain any significant speleothem formations, and typically it is fairly dry, with the notable exception of the lakes in the lower level.

Koonalda Cave has been the subject of archaeological and speleological study for several decades. We are working in collaboration with archaeologists from the South Australian Museum and Flinders University who are studying the cave and surrounding region. The cave contains evidence of human presence, including flint mining, believed to have occurred between 30,000 and 10,000 years ago. These visitors also left markings on some of the soft rock surfaces using fingers and other tools. The finger flutings form grooves about 3 to 5 mm deep that cover hundreds of square meters of the wall surfaces, which are in many places made up of a soft, powdery calcite material. It is expected that high-resolution 3D models of the cave will be valuable in providing data for remote archaeological and geomorphological study, as well as providing a virtual model that can be interactively explored, as the cave is not accessible to the public.

Our initial mapping expedition to Koonalda took place in November 2011, during which a single early Zebedee system was available and only the upper level was scanned. We returned to the cave in December 2012, when more complete scanning of both levels was performed with multiple Zebedee systems. Having multiple operators enabled the mapping team to scan different routes through the cave simultaneously, providing both redundancy and efficiency, as we could cover different sides of the many rockpiles more quickly in this manner. We estimate that it would be feasible to get an overall model of the cave structure using a single Zebedee system in under an hour, but we were aiming for fairly dense and complete coverage of all visible surfaces and therefore covered all reachable areas of the cave meticulously. In addition to the mapping team, the expedition included a team of archaeologists from the South Australian Museum, a photogrammetry researcher capturing the artwork in high-resolution detail, and representatives from the Mirning, who are the traditional owners of the land in which Koonalda resides. A significant portion of the data collection was performed

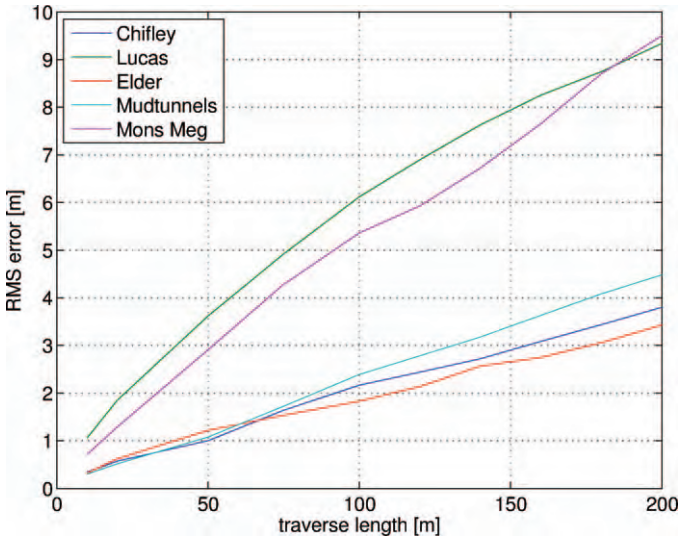

Figure 8. Positional root-mean-square (RMS) error curves calculated for five datasets, each of which forms part of a closed loop but is not itself a loop. The curves show the observed error as a function of the operator's traverse length, that is, the distance walked rather than the distance the swaying laser scanner traveled. For each dataset, the error is computed based on the difference between the endpoints of the open- and closed-loop solutions for different segment lengths of the Zebedee handle trajectory.

by one of the Mirning representatives, who successfully captured over an hour of data, predominantly covering the lower level of the cave, after one to two minutes of instruction on how to operate the system.

Figure 9 illustrates a full 3D map of the scanned area of the cave, including the sinkhole, the upper and lower levels, and the squeeze area. The squeeze is a 3 m long passage about 30 cm high connecting the northwest end of the upper level to a balcony above one of the lakes in the western end of the lower level. The data were recorded by three operators in a total of three hours of acquisition time, but less elapsed time due to the multiple units. The operators generally traversed the cave at a slow walking pace that varied somewhat based on local terrain. Visualizing the map in Figure 9 as a 3D model on screen can facilitate scientific modeling and analysis of various aspects of its history, including geomorphology, extent of former twilight zones, and possible former entrances. A comparative overlay between the 1976 survey map and the Zebedee 3D map is presented in Figure 10. The two maps are generally in agreement, though there is a slight angular difference at the squeeze. It is difficult to know which is closer to the true structure without further independent measurements; we note, however, that the Zebedee model closes a loop through measurements of the lower level from the balcony, and we are unaware of whether the traverse was closed in the 1976 survey. An example close-up view of an area in the upper level known as the Ramparts is presented in Figure 11. This rendering illustrates the level of detail available in the 3D point cloud data. In general, the density of the point cloud is a factor of how quickly the operator traverses the cave and how much time is spent scanning a particular area of interest. The lakes on the lower level of the cave (not shown in the figure) appear as empty areas in the point cloud, because the beam from the infrared laser is for the most part absorbed or specularly reflected by water, though it can penetrate where the water is sufficiently shallow.

Conclusions

We have introduced a new system that enables the application of mobile LiDAR mapping technology to surveying natural cave environments for the first time. The Zebedee 3D mapping system has been demonstrated in a variety of caves, with the most extensive results in Jenolan Caves and Koonalda Cave in Australia. The proposed method offers improvements over current practice and state-of-the-art technology in a number of ways. Mobility increases efficiency by transforming the mapping process into a continuous one in which a single person can survey a cave in approximately the same time it takes to traverse through it. The portability and flexibility of the equipment ensures that it can go nearly everywhere its operator can, including through tight squeezes, up ladders, and down abseils. Coverage of the environment is achieved through mobility, rather than worrying about viewpoint positioning as in the case of static terrestrial LiDAR. The equipment can be operated by non-experts with almost no training. In general, a brief coaching session is sufficient. In addition, workflow automation for both data acquisition and processing enables non-experts to generate 3D models directly from raw data and prevents errors that can occur with manual techniques. The 3D point cloud maps that are generated and the surface models that are created from them are significantly more detailed and accurate locally compared to traditional hand sketches and coarse 3D models based on left-down-up-right measurements at stations. Maps can also be transformed into a georeferenced coordinate frame if suitable control points within or GPS measurements outside the cave are available and can be associated with the existing data. While rough maps from traditional survey methods can be suitable for general navigation through a cave, for some applications, such as scientific research and environmental assessment, greater detail and resolution are required.

There are some limitations to the current system, several of which are being addressed as the technology progresses. Over large scales, the accuracy of the system can be lower than traditional methods applied with the best current equipment and expertise. We are working on advancements to the algorithms and hardware that should improve the system performance over time. The centimeter-scale precision of the range measurements of the Hokuyo scanner preclude the capture of fine details such

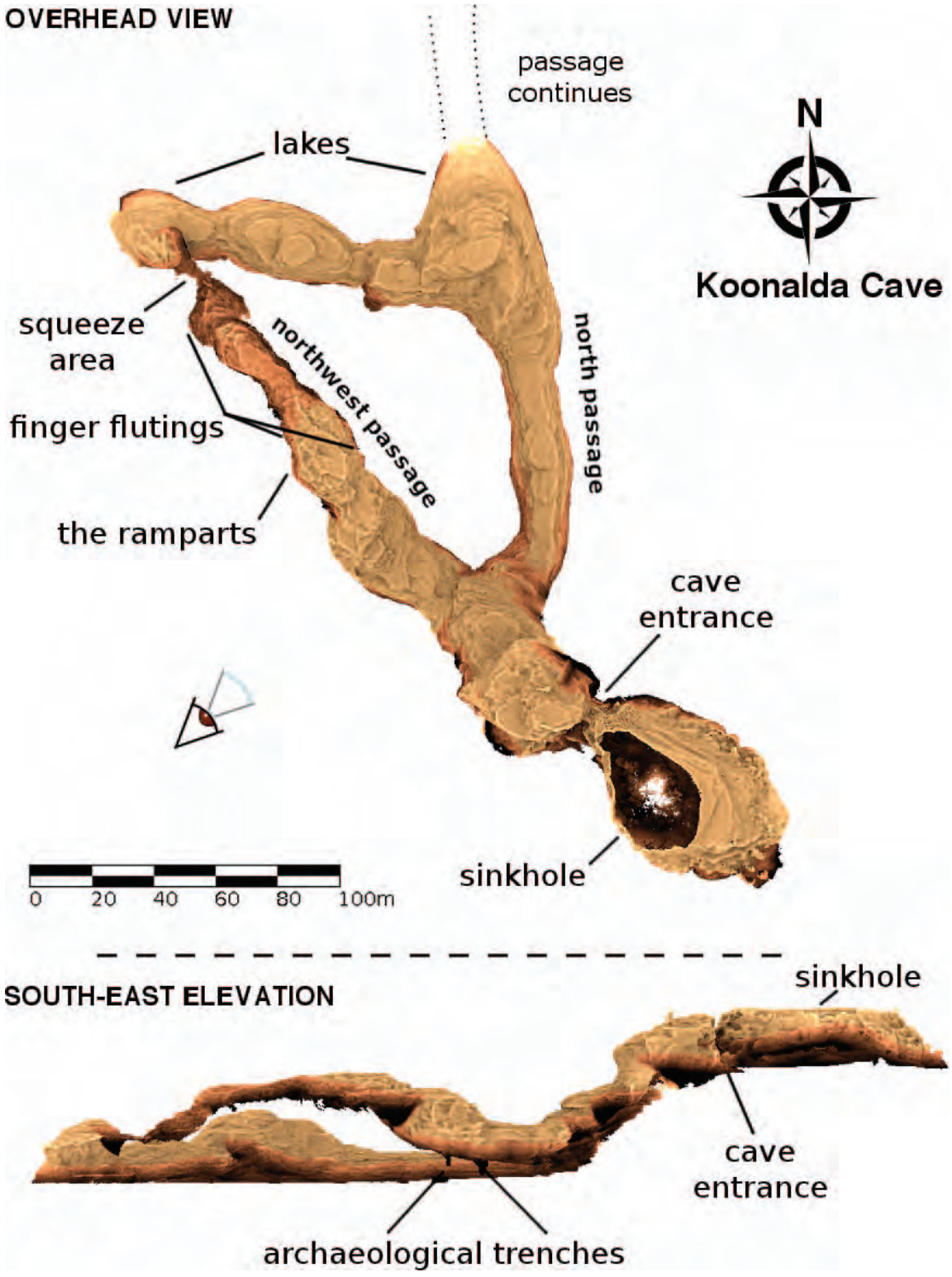

Figure 9. Three-dimensional map of Koonalda Cave generated using the Zebedee system. The eye icon indicates the viewing direction of the side elevation. Several areas of interest are marked. The model consists of approximately 300 million points, each of which is colored according to the relative local height above the cave floor. The point cloud was generated using five separate datasets representing under three hours of data collection, some of which was done in parallel by multiple operators. The survey of the north passage was not completed, as it contains deeper lakes and would have required a boat or other equipment to proceed. Two archaeological trenches are visible in the southeast elevation view.

Figure 10. Overhead view of a 3D map of the upper level of Koonalda Cave generated with the Zebedee system. A line drawing from a 1976 map (using tacheometer, 5 mm graduated staff, and Suunto compass) has been manually overlaid for comparison. Some differences in the wall locations can be attributed to the fact that the 1976 survey was sketched at a particular height, whereas this view of the 3D map highlights the outer hull of the cave walls. Note the slight differences between the two maps in the upper left near the squeeze area. The 3D map consists of approximately 150 million points, each of which is colored according to the relative local height above the cave floor.

as the finger flutings at Koonalda and very thin speleothem features at Jenolan. However, in cases where these features are relatively localized, other techniques such as photogrammetry or static laser scanning can be used to produce high-resolution models that can be merged into the point cloud (photogrammetry is currently being investigated for modeling the finger flutings at Koonalda). Improvements in LiDAR technology could eventually result in a lightweight scanner with millimeter precision and other improved features that could seamlessly be incorporated into the Zebedee system. The existing equipment cannot be used underwater, though the core algorithms could be adapted for use with sonar or other suitable sensing modalities. In theory, there are some types of environments

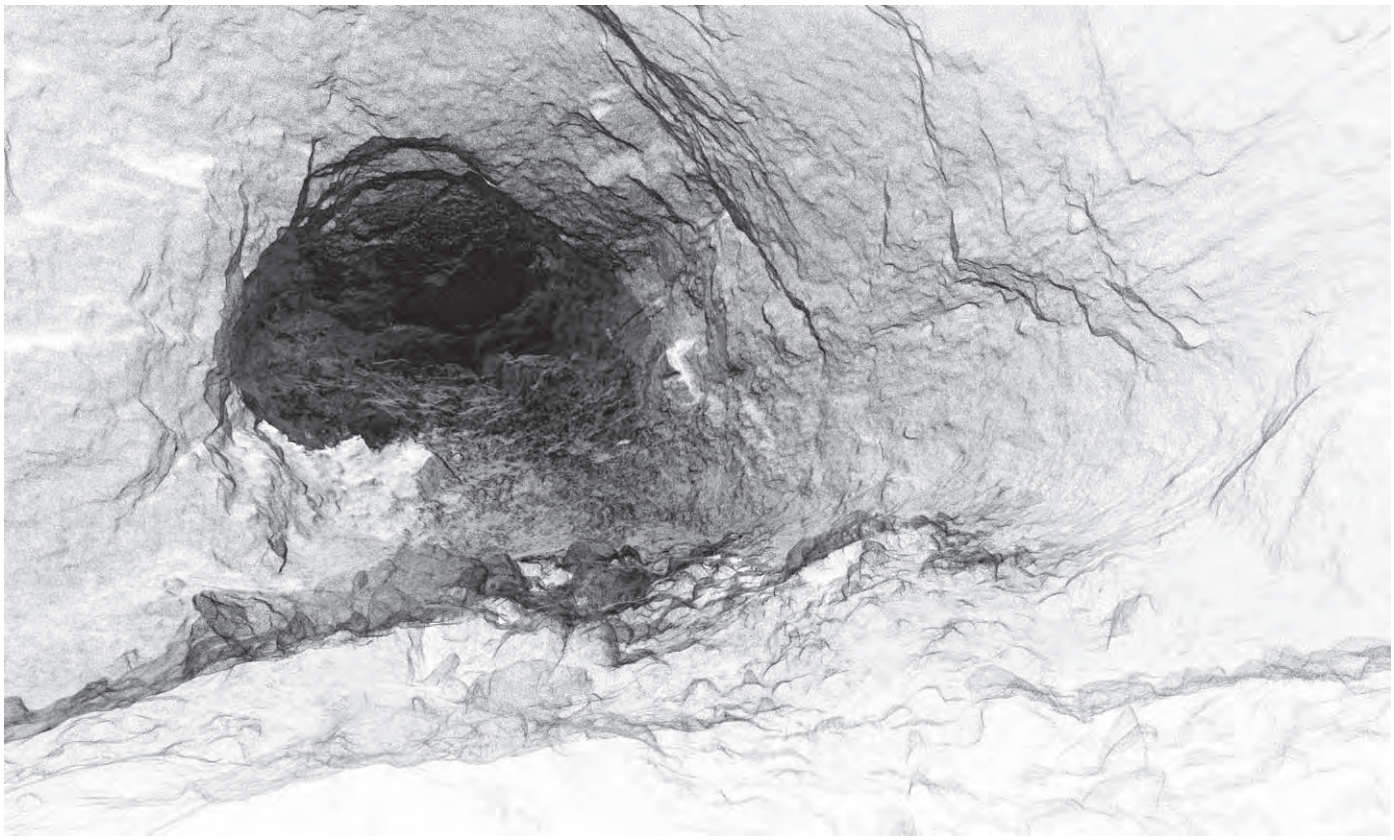

Figure 11. View of the 3D point cloud viewed from inside Koonalda Cave at the bottom of the Ramparts. In the foreground are several boulders, beyond which is a steep slope formed by significant ceiling collapse. The point cloud has been downsampled to 3 cm revolution.

that are theoretically troublesome for this technology, but these are not expected to occur in caves. For example, a very large (relative to the maximum scanning range) geometrically featureless void or a long, smooth tunnel-like environment would make it difficult to estimate the scanner's motion in all dimensions. Finally, the hardware currently costs thousands of dollars, which may limit affordability for some cave survey applications.

Our data collection strategy thus far has primarily been intended to map the caves, and we did not specifically plan in experimental procedures that would provide a straightforward way to quantitatively compare the results with previous surveys. We intend to address this in upcoming field trips when we will collect dedicated datasets specifically for comparison purposes. We also plan to replace some of our earlier datasets with data collected from more up-to-date hardware, which we expect will improve the overall accuracy of the maps.

Two-dimensional plan and section maps are widely used for navigation through caves, and high-resolution 3D models are not necessarily suitable for this purpose. Further processing can be done to convert the 3D models into the standard 2D symbolic representations for printing out on paper. Another possibility is that 3D electronic or even solid representations of caves could become a standard navigation tool in the future. We are further investigating methods for colorizing the point clouds according to the visual appearance of the caves, and have recently generated preliminary results towards this goal by adding a small camera to the handheld unit.

Although Zebedee has been deployed across a wide range of mapping applications, including forests, mines, interiors and exteriors of buildings, and industrial sites, the concept was initially inspired by imagining how we could adapt larger, vehicle-borne technology into a form suitable for mapping caves. We envision that the availability of this technology will create new opportunities for scientific studies of natural caves that were previously impossible. The fact that the system can be fully automated also opens up the possibility that similar hardware can be deployed on robotic vehicles in cave environments too difficult or hazardous for human exploration.

ACKNOWLEDGEMENTS

We acknowledge the assistance and support of a number of individuals and organizations in making this work possible. Paul Flick is largely responsible for the mechan-

ical and electronic design and assembly of both the Zebedee and Hannibal hardware platforms. We wish to acknowledge the traditional land owners of both of the cave sites visited.

Our 2010 field trip to the Jenolan Caves was partially supported by the Australian Nuclear Science and Technology Organisation (ANSTO).We wish to acknowledge in particular the contribution of Chris Waring there in helping to coordinate the fieldwork for multiple trips, assisting with data collection, and introducing the opportunity to map the caves. We thank the Jenolan Caves Reserve Trust and the many guides who have assisted our efforts over the years. The survey locations illustrated in Figure 7 are courtesy of the Jenolan Caves Survey Project. We also thank the Sydney Speleological Society and Jenolan Caves Historical and Preservation Society for assistance in locating source materials.

We wish to thank the Mirning People for their support and involvement with this project at Koonalda. Our work there has been partially supported by the Department of Industry, Innovation, Science, Research and Tertiary Education through an Inspiring Australia–Unlocking Australia's Potential grant and by the South Australian Museum. We wish to acknowledge Keryn Walshe of the SA Museum and Flinders University for inspiring this effort and coordinating the fieldwork. We also thank SA Parks & Wildlife and the South Australian State Emergency Service for providing assistance with access and entry to the cave. The 1976 survey data appearing in Figure 10 was produced by I. D. Lewis and K. R. Mott, Cave Exploration Group South Australia and the SA Museum and provided courtesy of the SA Museum Archives/Archaeology/Gallus/Koonalda.

We also wish to thank and acknowledge Claude Holenstein, Ciril Baselgia, and Hans Moorkens of the Commonwealth Scientific and Industrial Research Organisation (CSIRO) for their contributions in developing the 3D surface reconstruction software used to generate the maps in Figure 4; Peyman Moghadam (CSIRO), Stuart Hankin (ANSTO), and Michael Laing (Mirning) for assistance with data collection; Elise Bosse for developing the web/smartphone interface to the Zebedee system; and Aaron Morris for initial inspiration towards addressing the challenge of mobile cave mapping.

References

Baselgia, C., Bosse, M., Zlot, R., and Holenstein, C., 2014, Solid model reconstruction of large-scale outdoor scenes from 3D LiDAR data, *in* Yoshida, K., and Tadokoro, S., eds., Field and Service Robotics: Berlin, Springer Tracts in Advanced Robotics 92, p. 541–554. doi:10.1007/978-3-642-40686-7_36.

Bosse, M., and Zlot, R., 2009, Continuous 3D scan-matching with a spinning 2D laser, *in* ICRA '09: IEEE International Conference on Robotics and Automation, p. 4312–4319. doi:10.1109/ROBOT.2009.5152851.

Bosse, M., and Zlot, R., 2013, Place recognition using keypoint voting in large 3D LiDAR datasets, *in* 2013 IEEE International Conference on Robotics and Automation (ICRA), p. 2677–2684. doi:10.1109/ICRA.2013.6630945.

Bosse, M., Zlot, R., and Flick, P., 2012, Zebedee: Design of a spring-mounted 3D range sensor with application to mobile mapping: IEEE Transactions on Robotics, v. 28, no. 5, p. 1104–1119. doi:10.1109/TRO.2012.2200990.

Canter, P., and Stott, A., 2011, Mapping interior spaces with speed, ease & accuracy: The American Surveyor, v. 8, no. 4

Davis, D.G., and Land, L., 2006, Recently discovered passages in Fort Stanton Cave, New Mexico, and implications for speleogenesis and regional geomorphic processes in the northern Sacramento Mountains, *in* Land, L., Lueth, V.W., Raatz, W., Boston, P., and Love, D.L., eds., Caves and Karst of Southeastern New Mexico: New Mexico Geological Society 57th Annual Field Conference, p. 219–226.

Dryjanskii, M., 2010, The subterranean world of Easter Island: GeoInformatics, v. 13, no. 1, p. 6–9.

Durrant-Whyte, H., and Bailey, T., 2006, Simultaneous localization and mapping (SLAM): Part I the essential algorithms: IEEE Robotics & Automation Magazine, v. 13, no. 2, p. 99–110. doi:10.1109/MRA.2006.1638022.

Fairfield, N., Wettergreen, D., and Kantor, G., 2010, Segmented SLAM in three-dimensional environments: Journal of Field Robotics, v. 27, no. 1, p. 85–103. doi:10.1002/rob.20320.

Gary, M.O., Fairfield, N., Stone, W.C., Wettergreen, D., Kantor, G., and Sharp, Jr., J.M., 2008, 3D mapping and characterization of Sistema Zacatón from DEPTHX (DEep Phreatic THermal eXplorer), *in* Yuhr, L.B., Alexander, Jr., E.C., and Beck, B.F., eds., Proceedings of the 11th Multidisciplinary Conference on Sinkholes and Engineering and Environmental Impacts of Karst: American Society of Civil Engineers Geotechnical Special Publication no. 183, p. 202–212. doi:10.1061/41003(327)20.

Heeb, B., 2008, Paperless caving – an electronic cave surveying system, *in* Gonon, T., ed., Proceedings of the 4th European Speleological Congress, Vercors 2008: Lyon, Fédération française de spéléologie, Spelunca Mémoires 33, p. 130–133.

Holenstein, C., Zlot, R., and Bosse, M., 2011, Watertight surface reconstruction of caves from 3D LiDAR data, *in* 2012 IEEE/RSJ International Conference on Intelligent Robots and Systems, p. 3830–3837. doi:10.1109/IROS.2011.6095145.

Hunter, D., 2010, A field trial of common hand-held cave survey instruments and their readers, Bullita Cave System, July 2010: Caves Australia, no. 183, p. 10–12.

James, J.M., Martin, D.J., Tunnock, G.M., and Warild, A.T., 2009, A cave survey for research and tourist cave management, *in* White, W.B., ed., Proceedings 15th International Congress of Speleology: Huntsville, National Speleological Society, v. 3, p. 1381–1387.

Kershaw, B., 2012, Managing the survey information of the caves of Judbarra / Gregory National Park, Northern Territory: Helictite, v. 41, p. 87–94.

Liu, T., Carlberg, M., Chen, G., Chen, J., Kua, J., and Zakhor, A., 2010, Indoor localization and visualization using a human-operated backpack system, *in* Mautz, R., Kunz, M., and Ingensand, H., eds., Proceedings of the 2010 International Conference on Indoor Positioning and Indoor Navigation: IEEE, 10 p. doi:10.1109/IPIN.2010.5646820.

McIntire, D., 2010, Laser scanning mushpot cave: The American Surveyor, v. 7, no. 9, p. 18–27.

Middleton, G.J., 1991, Oliver Trickett: Doyen of Australia's Cave Surveyors, 1847–1934: Sydney Speleological Society Occasional Paper no. 10, 156 p.

Morris, A., Ferguson, D., Omohundro, Z., Bradley, D., Silver, D., Baker, C., Thayer, S., Whittaker, C., and Whittaker, W., 2006, Recent developments in subterranean robotics: Journal of Field Robotics, v. 23, no. 1, p. 35–57. doi:10.1002/rob.20106.

Nüchter, A., Surmann, H., Lingemann, K., Hertzberg, J., and Thrun, S., 2004, 6D SLAM with an application in autonomous mine mapping, *in* Proceedings, 2004 IEEE International Conference on Robotics and Automation, ICRA '04, p. 1998–2003. doi:10.1109/ROBOT.2004.1308117.

Osborne, R.A.L., Zwingmann, H., Pogson, R.E., and Colchester, D.M., 2006, Carboniferous clay deposits from Jenolan Caves, New South Wales: implications for timing of speleogenesis and regional geology: Australian Journal of Earth Sciences, v. 53, no. 3, p. 377–405. doi:10.1080/08120090500507362.

Petrie, G., 2010, Mobile mapping systems: An introduction to the technology: GeoInformatics, v. 13, no. 1, p. 32–43.

Rüther, H., Chazan, M., Schroeder, R., Neeser, R., Held, C., Walker, S., Matmon, A., and Howritz, L.K., 2009, Laser scanning for conservataion and research of African cultural heritage sites: The case study of Wonderwerk Cave, South Africa: Journal of Archaeological Science, v. 36, p. 1847–1856. doi:10.1016/j.jas.2009.04.012.

Sadier, B., Delannoy, J.-J., Benedetti, L., Bourlès, D.L., Jaillet, S., Geneste, J.-M., Lebatard, A.-E., and Arnold, M., 2012, Further constraints on the Chauvet cave artwork elaboration: Proceedings of the National Academy of Sciences of the United States of America, v. 109, no. 21, p. 8002–8006. doi:10.1073/pnas.1118593109.

Slavova, T., 2012, Modern methods and devices for mapping underground galleries and natural caves, *in* Proceedings of the 4th International Conference on Cartography and GIS. 7 p.

Stone, W.C., am Elde, B.A., Wefer, F.L., and Jones, N.A., 2000, Automated 3D mapping of submarine tunnels, *in* Stone, W.C., ed., Robotics 2000: Fourth International Conference and Exposition/ Demonstration on Robotics for Challenging Situations and Environment American Society of Civil Engineers, p. 148–157. doi:10.1061/ 40476(299)19.

Warild, A., 2007, Vertical, 5th edn.: Alan Warild, 206 p.

Waring, C., Wilson, S., Hurry, S., and Griffith, D., 2009, Cave speleothem growth response to external weather from continuous cave atmosphere (CO2) and drip-water chemistry (DIC) isotopic measurement [abs.]: Geophysical Research Abstracts, v. 11, 11778 p.

Zlot, R., and Bosse, M., 2014, Efficient large-scale three-dimensional mobile mapping for underground mines: Journal of Field Robotics, v. 31, no. 5, p. 758–779. doi:10.1002/rob.21504.

J. Zhu, T.P. Taylor, J.C. Currens, and M.M. Crawford – Improved karst sinkhole mapping in Kentucky using LiDAR techniques: a pilot study in Floyds Fork Watershed. *Journal of Cave and Karst Studies,* v. 76, no. 3, p. 207–216. DOI: 10.4311/2013ES0135

IMPROVED KARST SINKHOLE MAPPING IN KENTUCKY USING LIDAR TECHNIQUES: A PILOT STUDY IN FLOYDS FORK WATERSHED

JUNFENG ZHU*, TIMOTHY P. TAYLOR, JAMES C. CURRENS, AND MATTHEW M. CRAWFORD
Kentucky Geological Survey, University of Kentucky, 504 Rose Street, 228 MMRB, Lexington, Kentucky 40506

Abstract: The existing sinkhole database for Kentucky is based on low-resolution topographic maps created more than fifty years ago. LiDAR (Light Detection and Ranging) is a relatively recent technique that rapidly and accurately measures features on earth's surface in high-resolution. To test the feasibility of using LiDAR to map sinkholes in Kentucky, we have developed a method of processing LiDAR data to identify sinkholes and tested the method in portions of the Floyds Fork watershed in central Kentucky. The method consisted of four steps, creating a high-resolution digital elevation model (DEM) from LiDAR data, extracting surface depression features from the DEM, inspecting the depression features for probable sinkholes, and verifying the probable sinkholes in the field. A total of 1,683 probable sinkholes were identified in the study area, compared to 383 previously mapped for the same area. We field-checked 121 randomly-selected probable sinkholes and confirmed that 106 of them were karst sinkholes. This method increased the number of sinkholes by a factor of four with a success rate between 80% and 93% for the study area, demonstrating that the LiDAR sinkhole-mapping method is reliable and efficient. This method identified approximately 55% of the previously mapped sinkholes, and approximately 98% of the missed sinkholes appeared to be filled or covered for urban development and agriculture purposes. The next step is to extend this method to provide high-resolution sinkhole maps for other karst areas in Kentucky where LiDAR data become available.

INTRODUCTION

Detailed mapping of sinkholes is critical in understanding hydrological processes and mitigating geological hazards in karst landscapes. Sinkholes are surface depressions that form in places where carbonate rocks are dissolved from water and overlying soil particles are carried away underground, causing the surface to subside gently or collapse suddenly (Ford and Williams, 1989; Currens, 2002; Brinkmann, 2013). There are three general types of sinkholes, dissolution sinkholes, cover-subsidence sinkholes, and cover-collapse sinkholes (Tihansky, 1999). Sinkholes serve as a major connection between surface water and groundwater by collecting rainfall and draining it internally into the subsurface. Sinkholes can cause damage to private property and civil infrastructure such as buildings and roads. Cover-collapse sinkholes, which occur when the material overlying subsurface voids collapses, can cause damage to buildings and roads, farm ponds, and farming equipment (Currens, 2002). Because of their fixed cross-section area, sinkholes are prone to overflow and flooding. Some sinkholes can act as springs and discharge water to the surface during intense storms (Currens, 2002). Dinger et al. (2007) estimated the damages associated with sinkholes in Kentucky were approximately $23 million dollars per year. Consequently, existing land-use planning in karst areas often relies on detailed mapping of sinkholes (Fleury, 2009).

Some sinkholes can be recognized from the USGS 1:24,000 scale topographic maps. These topographic maps include closed depression features, often indicative of sinkholes in karst terrains. In the last few decades, several states have developed digital sinkhole databases based on the topographic maps (Beck, 1984; Florea et al., 2002; Paylor et al., 2003; Alexander et al., 2013). Developing a sinkhole database from topographic maps first requires digitization of the closed depressions, which is often labor intensive because the number of sinkholes is commonly in the thousands on a regional scale (Florea et al., 2002). In addition, the topographic maps have elevation contour intervals of 3 m, 6 m, or higher, resulting in shallow and small sinkholes being overlooked. Furthermore, most USGS topographic maps were created prior to the 1970s, and many new sinkholes may have developed since then. Although people recognize that not all closed depressions illustrated in these topographic maps are sinkholes, extensive field verification of the depressions rarely occurs, because the process is slow and costly.

Remote-sensing data have long been recognized as useful in locating sinkholes (Newton, 1976). High-resolution, high-accuracy data obtained from modern

* Corresponding author: Junfeng.zhu@uky.edu

remote-sensing technology provide opportunities to improve sinkhole mapping. For example, Littlefield et al. (1984) applied Landsat images to study the relationship between lineaments and sinkholes in west-central Florida. Dinger et al. (2007) used a spectrum enhancement method on 1 m resolution natural-color images to extract circular shapes that represented areas with different vegetation signatures than surrounding areas. Some of the circular shapes were found in the field to be active sinkholes. In this study, we used LiDAR (Light Detection and Ranging) to improve sinkhole mapping. LiDAR is a remote-sensing technique that rapidly and accurately measures features on the earth's surface by sending out short laser-light pulses and measuring their returns from an aircraft or a terrestrial platform. A laser pulse can have one or multiple returns because the pulse can encounter multiple reflection surfaces when it travels toward the earth's surface. Collected LiDAR data, called point clouds, are often post-processed to classify the points into several categories, including ground, vegetation, building, and water. LiDAR excels in revealing small surface features and has been widely used in studying natural resources and the environment (Evans and Hudak, 2007; Floyd et al., 2011; Crawford, 2012). LiDAR has also been applied in studying sinkholes in some other states. Seale (2005) and Seale et al. (2008) used LiDAR, also called airborne laser swath mapping, to map sinkholes in Pinellas County, Florida. They suggested that contemporaneous aerial photographs should be used in conjunction with LiDAR for reliable sinkhole mapping. Rahimi et al. (2010) and Rahimi and Alexander (2013) applied LiDAR to verify sinkholes mapped in the 1980s and 1990s in Winona County, Minnesota. They found that most of the inventoried sinkholes that had not been filled later for agricultural uses were visible using LiDAR. Mukherjee and Zachos (2012) used a sink-filling method to identify sinkholes from LiDAR and found an excellent match between LiDAR-identified and actual sinkholes in Nixa, Missouri. To test the feasibility of LiDAR in providing accurate and detailed sinkhole information for Kentucky, we developed a sinkhole-mapping method based on LiDAR point clouds and applied the method in a small karst watershed in central Kentucky.

STUDY AREA

The study area, Floyds Fork Watershed, is located approximately 16 km east of Louisville, Kentucky (Fig. 1). The watershed consists of two 10-digit USGS hydrologic units and drains parts of Bullitt, Henry, Jefferson, Oldham, Shelby, and Spencer counties, covering approximately 736 km^2. The Floyds Fork stream originates in the southwestern portion of Henry County and flows southwest to the Salt River, which flows to the Ohio River. The area has a subtropical climate with average annual precipitation of 117 cm (National Drought Mitigation Center, 2013).

Most of the Floyds Fork watershed is in the Outer Bluegrass physiographic region, and a small southwest portion of the downstream watershed is in the Knobs region (Fig. 1) (Woods et al., 2002). The Outer Bluegrass region has low to moderate relief with variable soil depth ranging from thick over limestone to thin over shales (Newell, 2001). The region is underlain by limestones, dolomites, and shales of Late Ordovician and Silurian age. The major formations are, from oldest to youngest, the Grant Lake Limestone, the Bull Fork Formation, the Drake Formation, the Osgood Formation, the Laurel Dolomite, the Waldron Shale, and the Louisville Limestone. The Osgood Formation and the Waldron Shale are composed of mostly shale (90% or higher) and very little dolomite. The remaining units are carbonate rocks (i.e., limestone and dolomite) with small amounts of calcareous shale. Most karst development occurs in these formations. The Knobs region is dominated by rounded hills, ridges, and narrow, high-gradient valleys (Woods, et al, 2002). Most of the Knobs region is non-karst and is underlain by diverse shale, mudstone, and limestone sedimentary rocks of Silurian and Mississippian age.

DATA AND METHOD

The data used in the sinkhole-mapping method included mainly LiDAR point clouds and aerial photography. The LiDAR data were provided by the Louisville/Jefferson County Information Consortium (LOJIC) through the Kentucky Division of Geographic Information and cover Bullitt, Jefferson, and Oldham Counties. LiDAR data were collected in March 2009 with an average point spacing of 1 m and a vertical root-mean-square error of 8.8 cm. The LiDAR points were post-processed into several categories. The categories associated with physical features include ground, low vegetation, medium vegetation, high vegetation, building, and water. The actual study area, which excluded non-karst areas, was approximately 580 km^2, or 79% of the watershed (Fig. 1). Bing Maps was the primary aerial photography used for this study. Data from Bing Maps were imported directly into ArcMap 10.1 (ESRI, 2012) as base maps. In addition to Bing Maps, we also used Google Earth historic images and aerial photography collected by LOJIC at two different times, one in 2009 and the other in 2012.

The sinkhole-mapping method has four steps, building a digital elevation model (DEM) from LiDAR point clouds, extracting surficial depression features for the DEM, inspecting the depression features for probable sinkholes, and field-checking the probable sinkholes. The first three steps were carried out in ArcMap 10.1.

In the first step, the LiDAR ground points were used to create a DEM with a cell size of 1.5 m using an average binning method. The average binning method calculates the elevation for each cell by assigning the average value of all points in the cell. More sophisticated interpolation

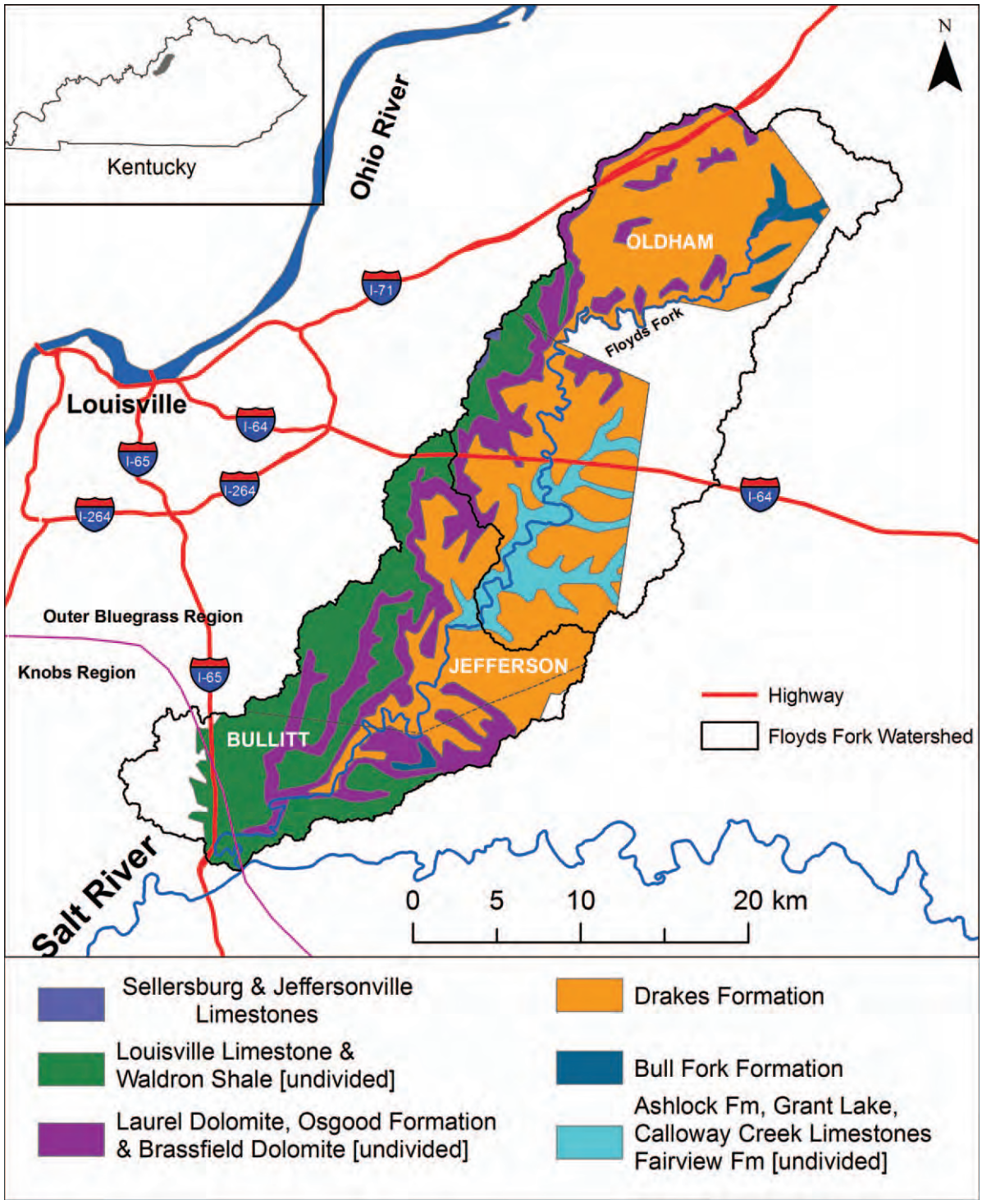

Figure 1. Location and geology of the study area. The Floyds Fork watershed is indicated by the irregular black line, with the bedrock geology shown for the karst portion that is the study area. The thin purple line is the boundary between the Blue Grass and Knobs regions.

methods, such as kriging, could potentially be used for this application. Because the cell size of the DEM was larger than the LiDAR point spacing, meaning at least one measurement is available for each cell, the average binning method was considered sufficient for this study.

Depression features were extracted from the DEM at the second step. A fill tool in ArcGIS was used to identify depression features on the DEM. The fill tool was originally developed to remove small depressions resulting from data noise; here it was used to find natural

depressions. The tool fills depressions on the DEM with an optional user-specified maximum sink depth. All depressions that are less than the maximum depth and are lower than their lowest adjacent neighbor will be filled to the height of their pour points. We used a maximum depression depth of 6 m, which allows identification of sinkholes that are less than 6 m deep. We considered this depth sufficient to identify most natural sinkholes in the study area. Mukherjee and Zachos (2012) found that a 4-m depth threshold was sufficient for identifying existing sinkholes in Nixa, Missouri. The fill tool generated a new filled DEM, and the depressions were then extracted by subtracting the filled DEM from the original DEM to create a depression raster.

The depressions identified in the fill procedure included depressions that were not sinkholes. Furthermore, we were interested in locating sinkholes that were considered to have a significant hydrologic impact in the Floyds Fork watershed, that is, sinkholes with relatively large drainage areas. For this reason, we selected the depressions with an area larger than 46 m^2 and depth of greater than 0.3 m for further processing. The selected depressions were then converted from raster format to polygon format. These polygons were further smoothed, and the holes inside some polygons that were artifacts of the raster-to-polygon conversion process were removed. These procedures for generating depression polygons from LiDAR can be accomplished by sequentially using several ArcGIS commands, including LAS Dataset To Raster, Fill, Raster Calculator, Raster to Polygon, Smooth Polygon, and Eliminate Polygon Part. To streamline these procedures, we built a model tool with a single user interface. The model tool asks the user to provide a single input, the LiDAR dataset, and then executes the aforementioned commands with default parameter values (DEM cell size, fill depth, depression area, smooth tolerance, etc.) automatically to create depression polygons. The tool also allows a user to change the parameter values on the same user interface.

In the third step, every polygon was visually inspected and manually classified into one of three categories, probable sinkholes, suspicious sinkholes, and non-sinkholes. A shaded-relief map with 5× vertical exaggeration was created from the LiDAR DEM to amplify the shape and depth of the depression features. The shaded-relief map along with aerial photography was used to classify the polygons. Seale et al. (2008) and Alexander et al. (2013) also used aerial photography to help identify sinkholes in their studies. To ensure a consistent classification, the polygon classification was carried out by a procedure consisting of an initial classification, a review, and discussion. The initial classification and the review were conducted by different individuals. The review results were then discussed to reach the final classifications. Although many polygons needed to be inspected, many of them were unambiguously stream channels, water-filled ponds, swimming pools, and drainage structures and were very easily and quickly identified as non-sinkholes. On the other hand, natural sinkholes tend to have a circular or elliptical shape and many of them have one or more internal drainage points (i.e., throats) that are readily visible on the shaded-relief map. On occasions, the classification procedure could not lead us to a decision, and these ambiguous polygons were assigned to suspicious sinkholes.

In the fourth step, probable sinkholes were randomly sampled for field-checking. To create a random sample of probable sinkholes over the entire area, we first divided the area by creating a 3,000-by-4000 ft grid, producing a set of cells larger than the number of probable sinkholes, and then randomly selecting one sinkhole from each cell that contained at least one, creating a pool of probable sinkholes from which those to be field-checked were randomly selected. Field investigators used a GPS-enabled iPad with a map showing locations of the selected probable sinkhole. The iPad tracked locations of the field investigators in real-time in relation to the location of each target to minimize location errors; since sinkholes in the study area generally occur in clusters, it is easy to check the wrong location. To check a probable sinkhole in the field we considered whether the feature was a depression, whether drain holes existed inside the feature, whether man-made structure(s) existed within the feature, whether there was vegetation within the feature, and whether water existed within the feature. The same sampling and field-checking methods were also used for suspicious sinkholes.

RESULTS AND DISCUSSION

We extracted approximately 10,720 depression polygons in the study area from the DEM created from the LiDAR dataset. Among the extracted polygons, 1,696 were classified as probable sinkholes and 282 as suspicious sinkholes. Approximately 10% of the probable sinkholes from Bullitt County and 5% from Jefferson and Oldham Counties were selected for field-checking. Excluding the samples that were inaccessible, mostly due to absent landowners, we field-checked 121 probable sinkholes and confirmed 106 of them (88%) as sinkholes (Fig. 2). We also randomly selected and field-checked 18 suspicious sinkholes and found 5 of them were actual sinkholes. The total number of actual sinkholes detected in the LiDAR data would be, based on the field-checking statistics, 1563. The LiDAR-derived sinkhole coverage is available to the public on the Kentucky Geological Survey's online map service (http://kgs.uky.edu/kgsmap/kgsgeoserver/viewer.asp).

The large number of polygons generated indicated that the depression-extraction procedure was effective in locating surface depressions. Although some of the polygons were associated with sinkholes, more than 80% of them were stream channels, ponds, or road drains or other man-made structures. The number of sinkhole-like depressions can be reduced by using an automated

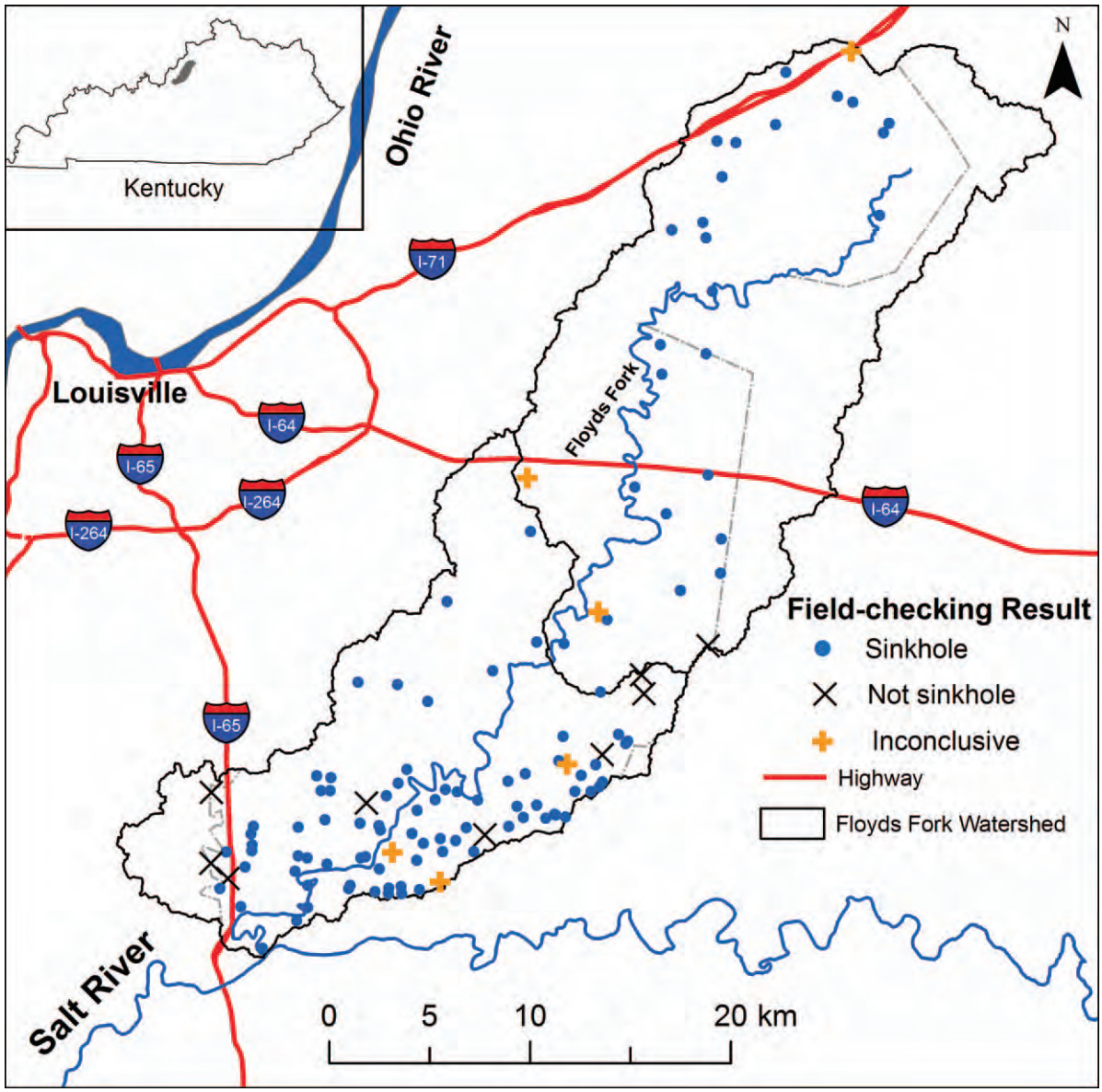

Figure 2. Field-checking results for randomly sampled probable sinkholes identified from the LiDAR data.

procedure. For example, Miao et al. (2013) illustrated one such procedure by using a random forest algorithm that uses shape and depth parameters to extract circular- or elliptical-shaped sinkholes from depressions. In our study area, we found that although most sinkholes have a circular or elliptical shapes, some sinkholes have more complicated shapes and may potentially be excluded by an automated procedure.

The polygon-classification process was actually quite fast and effective, because many polygons were easy to identify when using shaded-relief maps and high-resolution aerial photography (Fig. 4). Polygons associated with stream channels were the easiest to identify as non-sinkholes. On aerial photography, each had an elongated shape and overlapped stream channels; on a shaped-relief map, each had a smooth and flat bottom. The smoothed bottoms were artifacts on the DEM resulting from LiDAR beams being absorbed at the water surface. Polygons associated with water-filled ponds were also easily identifiable as non-sinkholes, because these polygons also had flat bottoms on shaded-relief maps. Polygons associated with man-made structures that have unnatural and irregular shapes were easily identifiable as non-sinkholes from aerial photography. On the other hand, some polygons associated with cover-collapse sinkholes were readily identifiable. On a shaded-relief map, those polygons had an internal drain that showed as a hole or throat inside the depression. Such polygons, when shown by aerial photography to be in a forested area of cluster of trees surrounded by grassland, were likely to be true cover-

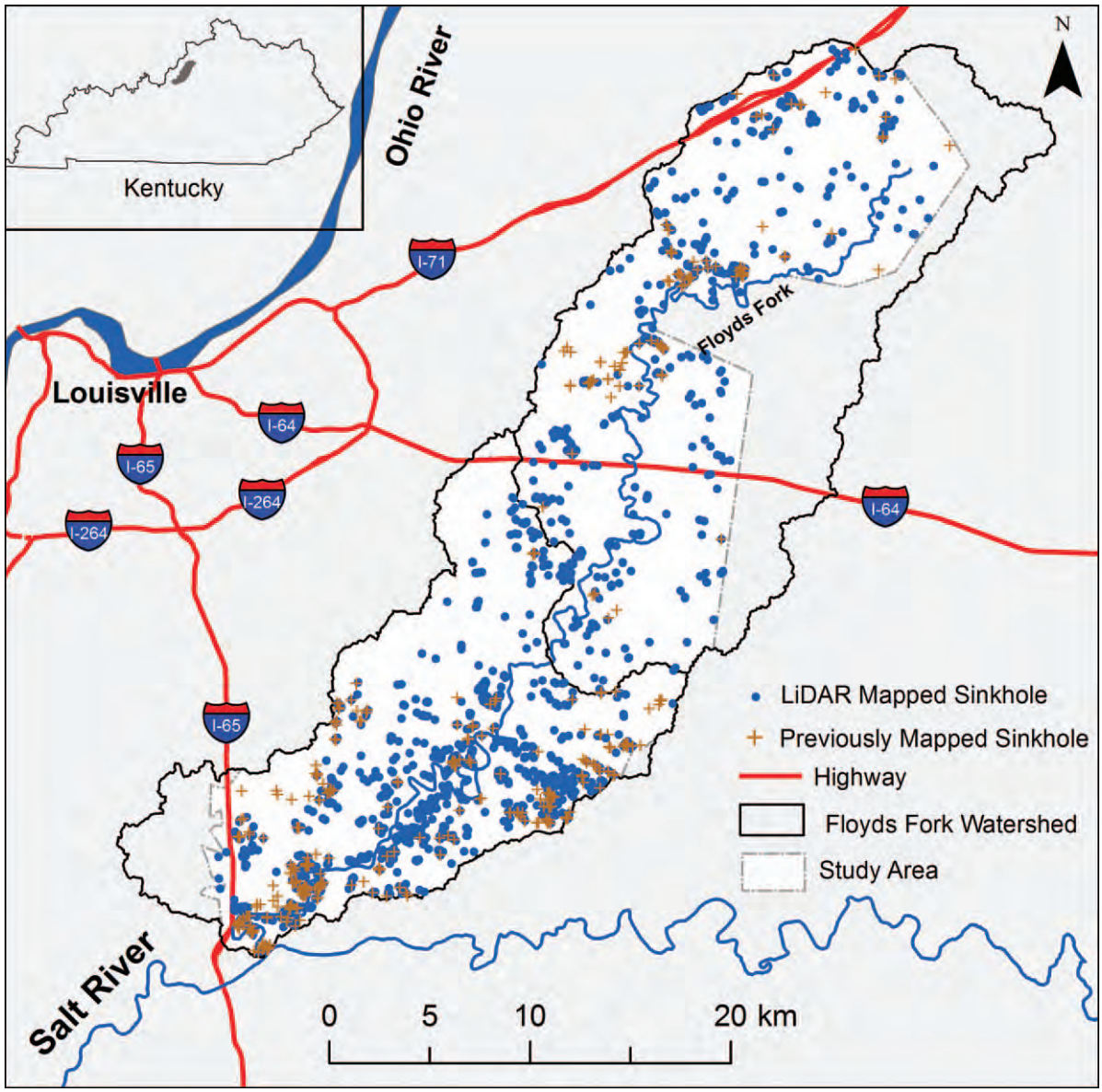

Figure 3. Comparison between sinkholes mapped from the LiDAR data and those previously mapped from topographic maps.

collapse sinkholes, but if those polygons were close to residential houses or roads, they could be either sinkholes or man-made retention basins with drains that appeared as holes. Polygons associated with subsidence sinkholes were harder to screen. On a shaded-relief map, they appeared as shallow, bowl-shaped depressions; on aerial photography, they could be in the middle of a farm field or close to a residential area. These polygons could have been either sinkholes or ponds that were empty when LiDAR was flown. For these polygons, we used historical aerial images to determine if these features were natural sinkholes or man-made ponds.

The field-checking of probable sinkholes showed an 88% success rate. However, the field-checked sinkholes were approximately 7% of all the sinkholes we identified. To understand the overall success rate and the margin of error for the study area, we considered this problem as a binomial distribution with two possible outcomes, sinkhole and non-sinkhole, and used sample statistics to estimate population parameters. The estimated proportion, i.e., the success rate (p) and standard deviation (σ_s) are (Zar, 1999):

$$p = \frac{X}{n} \quad \text{and} \quad \sigma_s = \sqrt{\frac{p(1-p)}{n-1}\left(1-\frac{n}{N}\right)}, \qquad (1)$$

where N is size of the population, n is the number of samples, and X is the number of success in the samples. We identified 1,696 probable sinkholes from LiDAR and field-checked 121. Among the 121 field-checked sinkholes, there are 106 sinkholes, 9 non-sinkholes, and 6 inconclusive. Considering all the inconclusive as non-sinkholes, the

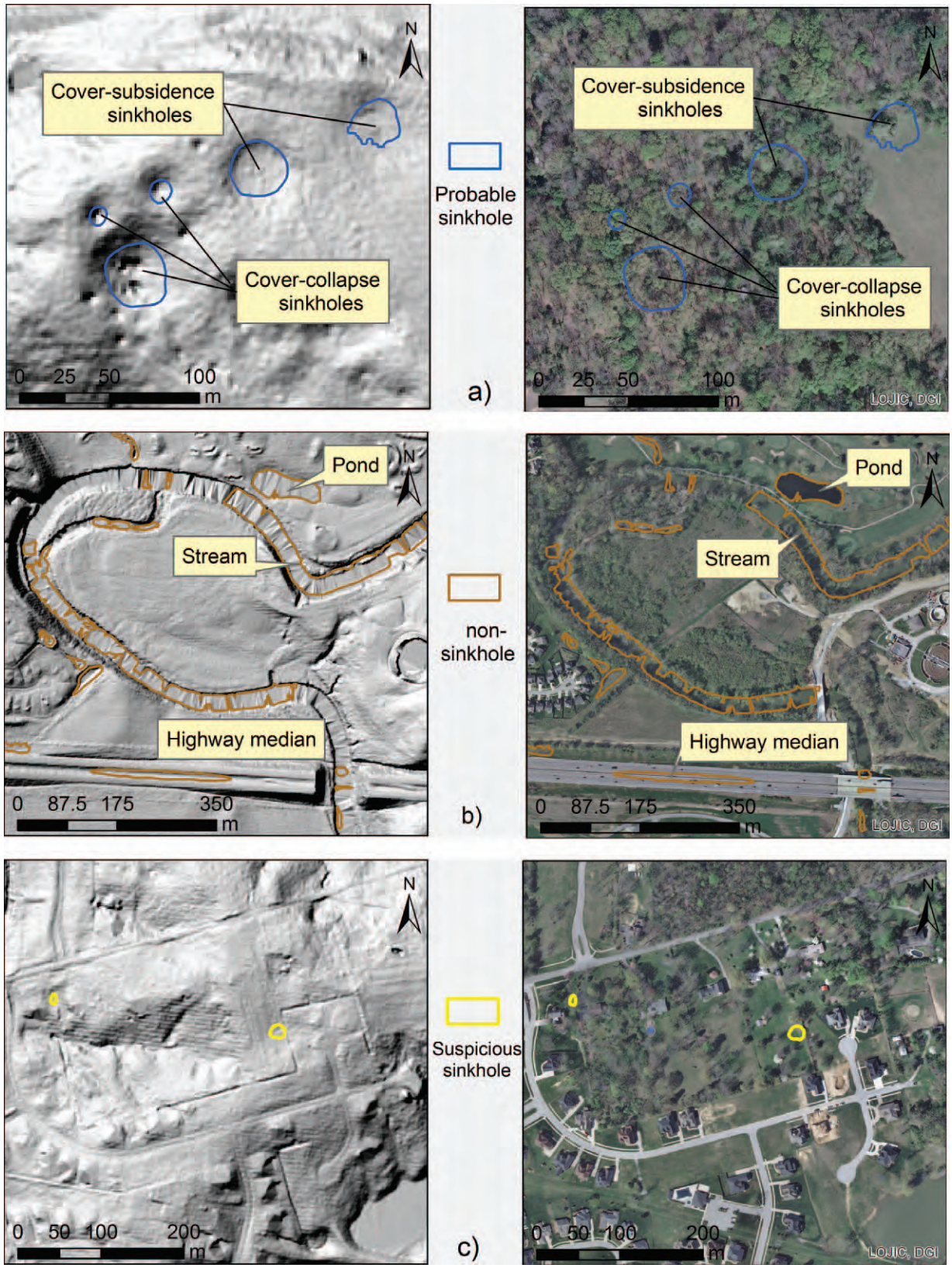

Figure 4. Examples of polygon classification, showing polygons overlain with shaded-relief (left) or aerial images (right): a) Examples of probable sinkholes. b) Examples of non-sinkholes. c) Examples of suspected sinkholes. The shaded-relief maps are 5× vertically exaggerated.

Table 1. Summary of field-checking of probable sinkholes, showing three types of depression characteristics and their success rates.

Depression Characteristics	Number of Field-Checked	Number of True Sinkholes	Success Rate
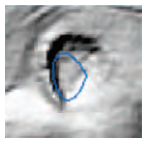 With-berm-no-hole	16	7	44%
 No-berm-no-hole	34	30	88%
 No-berm-with-hole	71	69	97%

estimated success rate and standard deviation are 0.88 and 0.03, respectively.

To estimate the margin of error, we calculated 95% of confidence interval based on Zar (1999), which calculates the lower confidence interval using

$$L_1 = \frac{X}{X + (n - X + 1) F_{0.05(2),\upsilon_1,\upsilon_2}}, \quad (2)$$

where $\upsilon_1 = 2(n - X + 1)$, $\upsilon_2 = 2X$, and $F_{0.05(2),\upsilon_1,\upsilon_2}$ is the 2-tailed 0.05 critical value for a F distribution with degrees of freedom ν_2 and ν_1; and the upper confidence limit using

$$L_2 = \frac{(X+1) F_{0.05(2)\upsilon_1',\upsilon_2'}}{n - X + (X+1) F_{0.05(2)\upsilon_1',\upsilon_2'}}, \quad (3)$$

where $\upsilon_1' = \upsilon_2 + 2$, $\upsilon_2' = \upsilon_1 - 2$, and $F_{0.05(2),\upsilon_1',\upsilon_2'}$ is the 2-tailed 0.05 critical value for a F distribution with degrees of freedom ν_2 and ν_1. Using equations (2) and (3), the lower and upper confidence limits are 0.80 and 0.93. In another words, we have 95% confidence in stating that the success rate of the method for the study area falls between 80% and 93%.

The success rate between 80% and 93% for the study area suggested that this method is reliable and promising. To further improve the reliability of the method, we explored the relationship between the field-checked depressions and true sinkholes by examined two prominent depression features, berms and holes, both of which were prominent on the shaded-relief maps. A berm is a prominent ridge along the rim of a depression, and a hole is a spot at the bottom of the depression that appears much deeper than its surroundings. All of the field-checked depressions fit into one of three categories: with-berm-no-hole, no-berm-no-hole, and no-berm-with-hole. The number of field-checked depressions in each category and the success rate for each category are summarized in Table 1. The no-berm-with-hole category made up 59% of the overall field-checked depressions, and this category had the highest success rate (97%) among the three categories. Most of the no-berm-with-hole features were revealed in the field as cover-collapse sinkholes, with the remainder being sinkholes with vertical rock openings or cover-subsidence sinkholes. The no-berm-no-hole category made up 28% of the overall field-checked depressions. This category proved 88% successful, and most sinkholes in this category were cover-subsidence sinkholes. The with-berm-no-hole category made up 13% of the overall checked sinkholes and had the lowest success rate (44%). The berm-like shape proved to be a man-made structure for a water-holding pond. But through time, as residual insoluble fill in rock joints is eroded into underlying conduits, many ponds started to leak and eventually were unable to hold water, thus functioning as sinkholes. For this type of depression it was difficult to distinguish between a pond that holds water periodically and a pond-turned-sinkhole.

Among the fifteen probable sinkholes that were not confirmed as true sinkholes in the field, nine of them were confirmed as non-sinkholes; they were either stream meander cutoffs, ponds with water or trash, or man-made drains. The other five features, shown as inconclusive in

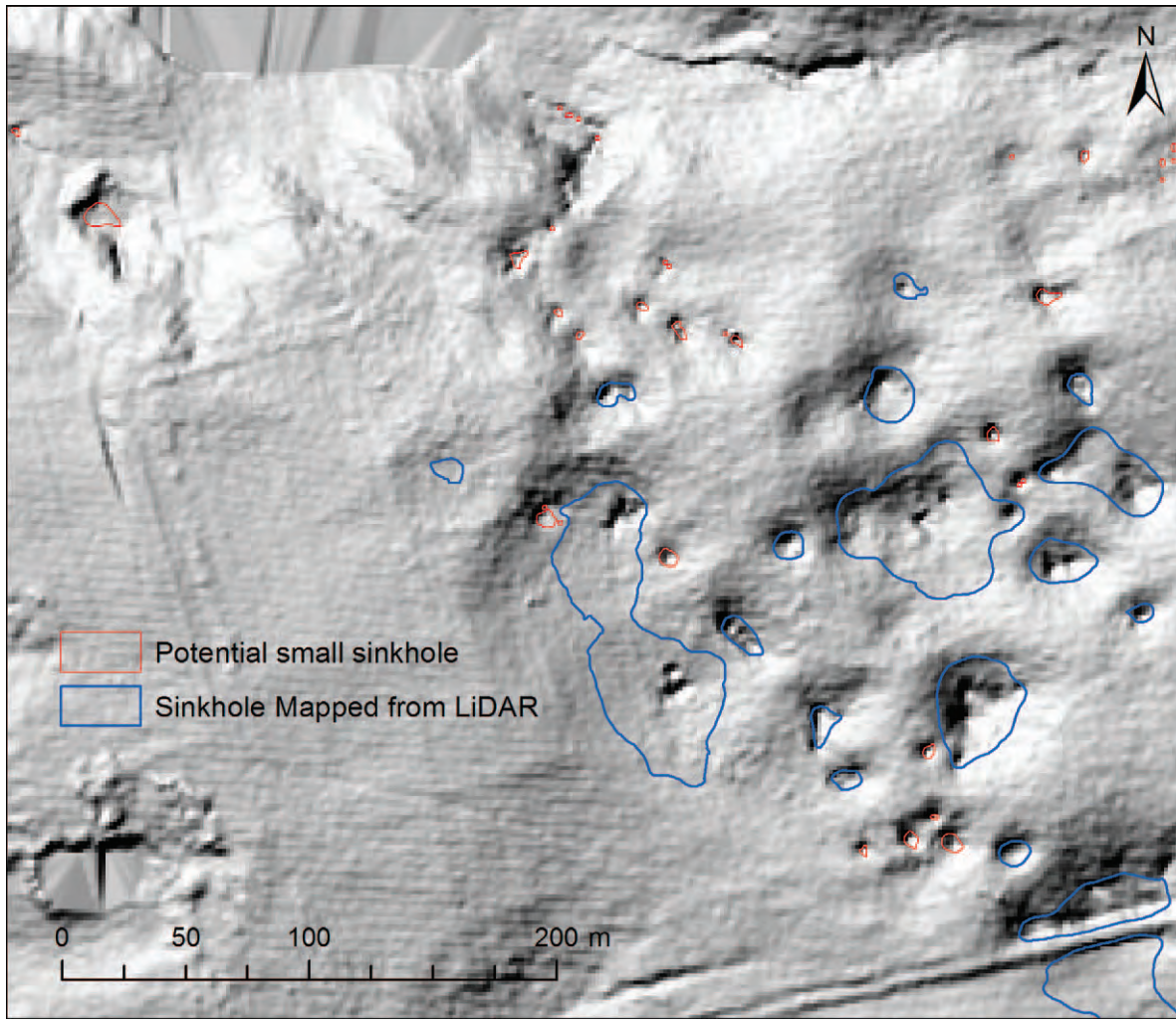

Figure 5. Shaded-relief map (5× vertically exaggerated) showing examples of potential small sinkholes not processed in this study.

Figure 2, could not be determined in the field. They appeared as a mix of natural karst features disturbed by human activities.

Since we focused on depression features that were 46 m^2 and larger, smaller potential sinkholes were not included. From the shaded-relief maps, we noticed that in some areas where large sinkholes were present there were also smaller depression features that appeared to be sinkholes. Figure 5 shows an example of such areas. The method we developed can be readily tailored to identify the smaller sinkholes when resources become available.

The existing Kentucky sinkhole coverage, which was derived from the USGS topographic maps, had 383 sinkholes for the same area (Fig. 3). Among the 383 sinkholes, 215 (56%) of them were also detected from the LiDAR data, and 168 (44%) of them were missed. Sixteen of the sinkholes found in both databases had slightly different locations but obviously corresponded to the same features, judging from the shaded-relief map. A visual inspection of the sinkholes missed by the LiDAR analysis using recent aerial images showed that approximately half of them overlapped with man-made structures, such as roads, buildings, parking lots, and quarries, and the rest were located on open fields, such as pasture, but had either no or a very shallow depression associated with them. We speculate that many of those sinkholes may have been filled for agriculture or other purposes. This comparison showed that any sinkhole coverage needs to be updated frequently, because sinkholes are temporary features and can be easily enhanced, destroyed, or altered by human activities.

Conclusions

In this study, we developed a sinkhole-mapping method that uses high-resolution LiDAR and aerial photography to map karst sinkholes in detail. We applied the method to parts of the Floyds Fork watershed in central Kentucky and revealed four times as many sinkholes as the existing database for the same area. Field-checking suggested that the success rate of this method was between 80% and 93%

for the study area, indicating the method is accurate and reliable.

High-density and high-accuracy LiDAR data provide a great opportunity for mapping karst sinkholes in high resolution and with great detail. In particular, bare-earth elevation data in LiDAR point clouds revealed sinkholes in forested areas that were undetectable using only aerial images. The depression-extraction procedure was effective in locating surface depressions, but it did not distinguish sinkholes from other depressions, resulting in the need for additional visual screening. Shaded-relief maps, especially with vertical exaggeration, revealed depression features in great detail and served as the primary tool for the visual screening process. Examining aerial images from different sources and time periods was also critical to distinguishing sinkholes from other depression features. Shape and depth characteristics of the depressions were closely related to the physical features they represented. Most non-sinkhole depressions can be easily identified. Furthermore, field-checking suggested that no-berm-with-hole depressions were most likely to be sinkholes and the with-berm-no-hole depressions could be either sinkholes or ponds.

ACKNOWLEDGEMENTS

This study was supported by the Kentucky Geological Survey, and we would like to thank the Louisville/Jefferson County Information Consortium and the Kentucky Division of Geographic Information for providing the LiDAR data. Thanks also go to Liz Adams, Caleb Essex, Bailee Hodelka, Chase Lockhart, Mike Lynch, Brittany Shelton, Richard Smath, and Patrick Whalen, who assisted in the field-checking. We also thank three anonymous reviewers for their constructive comments, which greatly improved the manuscript.

REFERENCES

Alexander, S.C., Larson, E., Bomberger, C., Greenwaldt, B., Alexander, E.C., Jr., and Rahimi, M., 2013, Combining LiDAR, aerial photography, and Pictometry® tools for karst features database management, *in* Land, L., Doctor, D.H., and Stephenson, J.B., eds., Proceedings of the Thirteenth Multidisciplinary Conference on Sinkholes and the Engineering and Environmental Impacts of Karst: Carlsbad, National Cave and Karst Research Institute, Symposium 2, p. 441–448.

Beck, B.F., 1984, A Computer-Based Inventory of Recorded Recent Sinkholes in Florida: Orlando, Sinkhole Research Institute, University of Central Florida, Rept. No. 84-85-1, 12 p.

Brinkmann, R., 2013, Florida Sinkholes, Science and Policy: Gainesville, University Press of Florida, 256 p.

Crawford, M.M., 2012, Using LiDAR to Map Landslides in Kenton and Campbell Counties, Kentucky: Kentucky Geological Survey, ser. 12, Report of Investigations 24, 12 p.

Currens, J.C., 2002, Kentucky is Karst Country! What You Should Know about Sinkholes and Springs: Kentucky Geological Survey, Information Circular 4, Series XII, 35 p.

Dinger, J.S., Zourarakis, D.P., and Currens, J.C., 2007, Spectral enhancement and automated extraction of potential sinkhole features from NAIP imagery – initial investigations: Journal of Environmental Informatics, v. 10, no. 1, p. 22–29. doi:10.3808/jei.200700096.

ESRI, 2012, ArcGIS Desktop: Release 10.1 SP1: Redlands, California, Environmental Systems Research Institute.

Evans, J.S., and Hudak, A.T., 2007, A multiscale curvature algorithm for classifying discrete return LiDAR in forested environments: IEEE Transactions On Geoscience and Remote Sensing, v. 45, no. 4, p. 1029–1038. doi:10.1109/TGRS.2006.890412.

Florea, L.J., Paylor, R.L., Simpson, L., and Gulley, J., 2002, Karst GIS advances in Kentucky: Journal of Cave and Karst Studies, v. 64, p. 58–62.

Floyd, C.T., Syverson, K.M., and Hupy, C.M., 2011, Using LiDAR data and ArcGIS to evaluate subtle glacial landforms associated with the Early Chippewa and Emerald Phase Ice-Margin positions, Barron County, Wisconsin [abs.]: Institute on Lake Superior Geology Proceedings, 57th Annual Meeting, Ashland, WI, v. 57, p. 35–36.

Fleury, S., 2009, Land Use Policy and Practice on Karst Terrains: Living on Limestone: New York, Springer, 187 p. doi:10.1007/978-1-4020-9670-9,

Ford, D.C., Williams, P., 1989, Karst Geomorphology and Hydrology: London, Unwin-Hyman, 601 p.

Littlefield, J.R., Culbreth, M.A., Upchurch, S.B., and Stewart, M.T., 1984, Relationship of modern sinkhole development to large-scale photolinear features, *in* Beck, B.F., ed., Sinkholes: Their Geology, Engineering & Environmental Impact: Rotterdam, A. A. Balkema, p. 189–195.

Miao, Xin, Qiu, Xiaomin, Wu, Shuo-Sheng, Luo, Jun, Gouzie, D.R., and Xie, Hongjie, 2013, Developing efficient procedures for automated sinkhole extraction from lidar DEMs: Photogrammetric Engineering & Remote Sensing, v. 79, no. 6, p. 545–554. doi:10.14358/PERS.79.6.545.

Mukherjee, A., and Zachos, L.G., 2012, GIS analysis of sinkhole distribution in Nixa, Missouri [abs.]: Geological Society of America Abstracts with Programs, v. 44, no. 7, 549 p.

National Drought Mitigation Center, 2013, Annual Climatology: Louisville, KY (SDF), http://drought.unl.edu/archive/climographs/LouisvilleANC.htm, accessed October 24, 2013.

Newell, W.L., 2001, Physiography, *in* McDowell, R.C., ed., The Geology of Kentucky — A Text to Accompany the Geologic Map of Kentucky: U.S. Geological Survey Professional Paper 1151-H, p. 79–83.

Newton, J.G., 1976, Early Detection and Correction of Sinkhole Problems in Alabama, with a Preliminary Evaluation of Remote Sensing Applications: Alabama Highway Department, Bureau of Research and Development, Research Report no. HPR-76, 83 p.

Paylor, R.L., Florea, L.J., Caudill, M.J., and Currens, J.C., 2003, A GIS Coverage of Sinkholes in the Karst Areas of Kentucky: Kentucky Geological Survey, metadata file and shapefiles of highest elevation closed contours, 1 CDROM, (http://kgs.uky.edu/kgsweb/download/karst/ksinks.zip).

Rahimi, M., Alexander, S.C., and Alexander, E.C., Jr., 2010, LiDAR mapping of sinkholes: Winona County, MN [abs.], Geological Society of America Abstracts with Programs, Joint Meeting North-Central/South-Central Sections, v. 42, no. 2, p. 107–108.

Rahimi, M., and Alexander, E.C., Jr., 2013, Locating sinkholes in LiDAR coverage of a glacio-fluvial karst, Winona County, MN, *in* Land, L., Doctor, D.H., and Stephenson, J.B., eds., Proceedings of the Thirteenth Multidisciplinary Conference on Sinkholes and the Engineering and Environmental Impacts of Karst: Carlsbad, National Cave and Karst Research Institute, Symposium 2, p. 469–480.

Seale, L.D., 2005, Creation, analysis, and evaluation of remote sensing sinkhole databases for Pinellas County, Florida [M.S. Thesis]: Tampa, University of South Florida, 55 p.

Seale, L.D., Florea, L.J., Brinkmann, R., and Vacher, H.L., 2008, Using ALSM to identify closed depressions in the urbanized, covered karst of Pinellas County, Florida—1, methodological considerations: Environmental Geology, v. 54, p. 995–1005. doi:10.1007/s00254-007-0890-8.

Tihansky, A.B., 1999, Sinkholes, west-central Florida, *in* Galloway, D., Jones, D.R., and Ingebritsen, S.E., eds., Land Subsidence in the United States: U.S. Geological Survey Circular 1182, p. 121–140.

Woods, A.J., Omernik, J.M., Martin, W.H., Pond, G.J., Andrews, W.M., Call, S.M., Comstock, J.A., and Taylor, D.D., 2002, Ecoregions of Kentucky (color poster with map, descriptive text, summary tables, and photographs): Reston, VA., U.S. Geological Survey (map scale 1:1,000,000).

Zar, J.H., 1999, Biostatistical Analysis, 4th ed.: Upper Saddle River, NJ: Prentice Hall, 929 p.

T.J. Jovanelly – Sinkholes and a disappearing lake: Victory Lake case study. *Journal of Cave and Karst Studies,* v. 76, no. 3, p. 217–229.
DOI: 10.4311/2012ES0272

SINKHOLES AND A DISAPPEARING LAKE: VICTORY LAKE CASE STUDY

Dr. Tamie J. Jovanelly
Associate Professor of Geology, Berry College, P.O. Box 495036, Mount Berry, GA 30149, tjovanelly@berry.edu

Abstract: Human-induced sinkhole collapse can result in drastic changes to landscape aesthetics and present challenges to land managers seeking to determine the plausibility of restoration, the amount of financial investment needed, and the long-term sustainability of tampering with karstic environments. Alteration of groundwater flow in a karstic environment expedited the formation of large sinkholes in the southern end of man-made Victory Lake, causing it to drain immediately. Soon after the lake emptied in 1986, two unsuccessful attempts were made to restore the 13 ha (32 ac) lake. The sinkholes formed in the southern basin were completely in-filled, eliminating 3 ha (8 ac) of lake basin and significantly altering the original lake morphology. Some twenty-seven years later, Victory Lake is holding some water in the shallow basin at the northern end and would primarily be classified as a marshy wetland. This study was initiated to investigate the current relationship between the groundwater and surface water at the lake's altered basin to determine the potential for it to be restored fully or partially as a recreational focal point of the Berry College campus. Over the course of one year we measured the inputs (stream flow and precipitation) and outputs (evaporation and surface water outflow) of the lake system. We were able to conclude that groundwater is not likely contributing to the lake, based on inorganic and stable isotope (^{18}O and ^{2}H) water chemistry analysis and the deep position of the groundwater table relative to the lake bottom. From the results of dye-tracer tests conducted in the lake, we concluded that basin water may not be escaping downward at measurable rates because of its clay bottom. Our overall water-budget analysis confirms an adequate water volume entering by rainfall and ephemeral stream inflow; nearly 90% of the water leaves Victory Lake through surface-water outflow. Water loss through evapotranspiration during spring and summer months overcomes the gain accomplished during wetter and cooler months, particularly February. Through an investigation of water level records kept for campus monitoring wells from 1998 through 2012 we confirm that the groundwater table has stabilized and the immediate threat of new sinkhole formation is minimal. Restoration of Victory Lake to its original picturesque meeting spot may be possible through creative engineering strategies and project financing. However, we question the longevity of managing a karstic environment and consider the potential risks to infrastructure, groundwater, and human health should lake bottom failure occur again on campus.

Introduction

During the late 1980s geologists began to report an increasing pace of human-induced sinkholes in the eastern United States, with particular focus on the changing landscapes in Georgia, Alabama, and Florida (MacIntyre, 1986; Newton, 1987). More recently, stress on and overuse of the Florida aquifer has led to several occurrences of emptied lakes, including Lake Jackson (1619 ha; 4,000 ac) and Lake Scott (115 ha; 285 ac) (Penson, 2002; McBride et al., 2011). Human-induced sinkholes often result from dewatering by wells, quarries, and mines in limestone environments (Newton, 1987; Fidelibus et al., 2011). The processes forming sinkholes can be enhanced by human-induced change in the groundwater hydrologic regime by either inflows or outflows resulting from pumping activities (Benito et al., 1995; Martinez et al., 1998; Florea et al., 2009). Surface subsidence can develop within a matter of days when highly soluble rocks dissolve due to anthropogenic pressures (Martinez et al., 1998). The location of sinkhole collapse and speed of formation, rather than the diameter or depth, dictate the threat to human life and the potential for economic loss (Newton, 1987). To date, the Federal Emergency Management Agency reports that insurance claims relating to sinkholes, either natural or human-induced, in the United States totals $100 million annually. Sinkhole formation is closely related to local hydrologic conditions, and human-induced changes to the local hydrology commonly accelerate the process. It has been shown that areas in the eastern United States that have a higher sinkhole density tend to show a lower water quality due to the direct pathway of contamination from surface to the groundwater table (Lindsey et al., 2010). An understanding of groundwater and surface water interac-

tions in karstic environments is essential for aquifer protection and the development of local water resources (Praise and Gunn, 2007; McBride et al., 2011).

Previous studies have indicated the usefulness of creating water budgets for lakes in karstic terrains (Dalton et al., 2004; McBride et al., 2011; Aurit et al., 2013). More specifically, the great seasonal variability of lakes' water budgets tied to the Florida aquifer and the repercussions to surrounding communities has been the focus of recent United States Geological Survey investigations (Dalton et al., 2004; Spechler, 2010; McBride et al., 2011; Sepúlveda et al., 2012). The research conducted at Lake Seminole (Dalton et al., 2004) provided the framework for the water budget completed in this study. Dalton lists the challenges to measuring evaporation or evapotranspiration over a hydrologic year and emphasizes the importance of it as a driver in seasonal lake volume. Human impact on groundwater resources may have been best highlighted by Spechler (2010) in his study of the Florida aquifer in south-central Florida. Spechler was able to illustrate the stresses of population growth on the groundwater level. In addition, Spechler's results show the high variability over time in aquifer water quality from a large sampling of 129 area wells. The study by McBride et al. reports a four-year water budget of Lake Panasoffkee in west-central Florida and focuses on the groundwater and surface water connectedness of a karstic system. In their study, environmental isotopes of strontium, oxygen, and hydrogen confirm interplay between groundwater and surface-water systems. In addition, they were able to discern through the stable isotope analysis that rainfall was a primary source of groundwater recharge within the Lake Panasoffkee watershed. The recent USGS publication by Sepúlveda et al. uses measured water budget parameters of runoff, infiltration, lake water levels, stream flows, and evapotranspiration measured from 1995–2006 in east-central Florida to compute the interaction of groundwater flow system with the surface environment using MODFLOW-2005. This model allowed them to make some predictions about long-term groundwater recharge and withdrawal rates.

A water budget systematically quantifies the gain, loss, and storage of water in the water cycle using the principle of the conservation of mass. Typical field measurements for a water budget include precipitation, groundwater inflow, surface water inflow, evaporation, transpiration, groundwater outflow, and surface water outflow. For water-supply planning and management, water budgets for aquifers and watersheds are an important tool used to determine fluctuations and stress on the system (Winstanley et al., 2006; Healy et al., 2007). As all components of the water cycle are connected, estimating future water budgets allows planners and managers to evaluate water availability and the impacts of withdrawals on the system. Data collected for water budgets are often used for understanding current hydrological conditions so that future outcomes can be forecast.

A water budget can be used to explore the impact on a single parameter or the entire system to a variable such as temperature. Many researchers opt for defining a water budget based on the response of one inflow or outflow parameter (Loague and Freeze, 1985; Winter, 1985; Deevey, 1988; Hebbert and Smith, 1990). The isolation of a single parameter, such as groundwater, may make it easier to identify the response of associated streams, lakes, or wetlands (Winter, 1999). For example, Winstanley and Wendland (2007) used a water budget to investigate response to climate change over time, and they showed the influence of temperature on water availability.

Water budgets are not limited by geographical scale. Some range from a small drainage basin, as in this study (11 km^2), to considerably larger areas like the 618 km^2 explored by Shuster et al. (2003). However, as was the focus of a paper by Hamilton-Smith (2006) and reiterated by Horvat and Rubinic (2006), the start of a quality water budget begins with the accurate delineation of the total catchment area.

Despite variations in project size, scope, and region of study, two questions persist in water budget analysis: What is the best way to measure evaporation, and what is the error in such estimates? Winter (1981) found that annual averages had smaller errors (2 to 15%) than monthly averages (2 to 30%). It appears that the preference in how evaporation is measured depends on the amount of data available or the amount of time and money a study has to commit. Using Class A pan evaporation measurements and Georgia Automated Environmental Monitoring Network (GAMEN) data as controls, Dalton et al. (2004) evaluated six different methods of calculating lake evaporation rates. The complexity and the amount of data needed, such as windspeed, humidity, and solar radiation for these methods varies greatly. Dalton et al. (2004) and Rosenberry et al. (1993) determined that the energy-budget method was 8 to 26% more reliable than empirically derived equations and ultimately provided the best match if raw data are unavailable.

SITE DESCRIPTION

Victory Lake (34°17′54″N, 85°12′07″W) is a recreational man-made lake that was completed in 1928 (Fig. 1). This picturesque spot on the Berry College campus provided a place for the college community to walk, picnic, and canoe. It has been important to Berry College and its alumni for decades. In 1953, Berry College sold mineral rights to a limestone quarry operator approximately 0.8 km west of Victory Lake. The quarry had successful mining operations for the next thirty-three years (Fig. 2a). By June 1986, the open-pit quarry was 110-m deep and daily pumping rates topped 52,616 $m^3\ s^{-1}$ (Richard Fountain, personal communication). At this time, the recorded depth to the water table on the Berry College campus was 44 m. Overnight, four large sinkholes more than 6 m in diameter

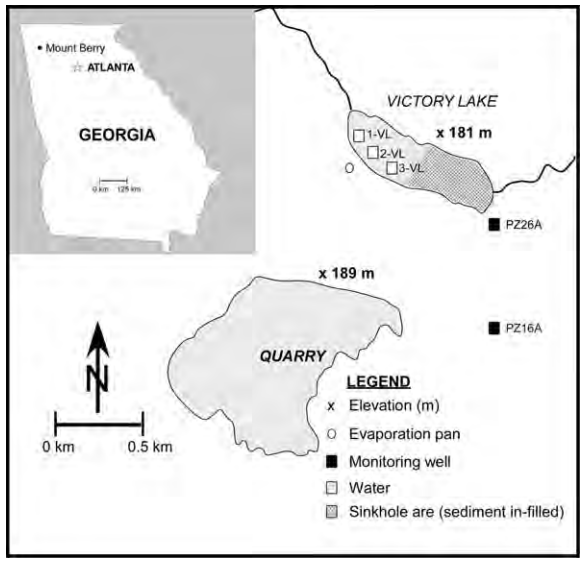

Figure 1. Location map of Victory Lake near Mount Berry, Georgia, showing its proximity to the quarry, surface-water sampling locations, monitoring wells, and other data sources. Geologic units and fault position estimated from Crawford (1990) [from Tom Crawford's unpublished 1990 geologic map of the Berry College campus.].

formed in the southern basin of Victory Lake that caused the lake to empty (Fig. 2b). Presumably, a cone of depression formed from the intense pumping at the quarry that caused the bottom of that part of the lake, which was over limestone, to collapse. The sinkholes were completely filled with earth materials after a few failed attempts at lake restoration (Fig. 2c). The lake basin was now reduced by 3 ha (8 ac), and water that originally drained through a tributary now left by way of a culvert. Some twenty-seven years later, siltation, plant encroachment, and beaver dams have turned Victory Lake into a shallow basin full of vegetation. Currently, the basin is only known to hold water for a short duration following a hard rainfall (Fig. 2d).

The purpose of this study is to determine the possibility of restoration of a lake influenced by karst topography. To do this, we conducted a fourteen-month investigation to measure the inflow and outflow components of the present-day Victory Lake's water budget. The goals of the water budget were to identify how lake volume responds to current patterns in seasonal changes in precipitation and temperature, to determine if groundwater is substantially adding to or leaving the system, to determine if current basin morphology is influencing the amount of water that the basin holds, and, ultimately, to determine the potential of lake restoration.

Study Area and Geologic Setting

Karstic features resulting from limestone dissolution are commonplace in the northwest Georgia physiographic region called the Ridge and Valley (Hubbard, 1988). The nearly two hundred caves mapped in the Cumberland Plateau north of Mount Berry are unlike Ridge and Valley underground caverns because they are typically connected and do not remain solitary underground voids (Jenkins, 2009; Buhlmann, 2001). Most of the voids in the Ridge and Valley region are formed by solution processes along fractures, joints, and bedding planes (Weary, 2005).

Two types of sinkholes occur most commonly in the Ridge and Valley region: cover-collapse and cover-subsidence (Hubbard, 1988). Cover-collapse sinkholes form when the surficial sediments contain a large amount of clay. The clay binds the soil so that it can bridge small cavities, but not large ones. Cover-subsidence sinkholes form when surficial sediments filter into cavities to gradually form surface depressions. (Florea et al., 2009). Although cover-subsidence sinkholes are known to be more destructive, both sinkhole varieties can pose risk to human health and economic risk to urban planners, developers, homeowners, and insurance companies (Scheidt et al., 2005). These types of natural sinkhole development are generally not predictable, although sinkholes can be expected where limestone formations are found (Newton, 1987).

The geology exposed at the surface around the perimeter of Victory Lake varies. The bedrock found under the western side of Victory Lake is predominately Mississippian-age limestone. This limestone is part of the Conasauga Formation. The Conasauga Formation consists of siltstone, claystone, shale, and limestone and was described by Anderson (1993). The formation is easily identifiable within the numerous sinkholes found in the forested area lining the western side of the lake. The contact between the shale and the limestone units of the Conasauga Formation can be seen at the quarry, however, the lower contact of the Conasauga Formation on Berry College's main campus is not exposed. From our review of the well logs from the twenty-two monitoring wells on campus that were drilled in 1998, the boundary is not clear. The maximum depth drilled in these monitoring wells is 93 m below the surface. The eastern side of the lake has exposures of Cambrian age sandstone. This sandstone is part of the Rome Formation, which consists of sandstone, siltstone, and claystone. This formation is known for tightly folded and steeply tilted beds (Anderson, 1993).

The geologic map of the Rome, Georgia, area was completed by Tom Crawford in 1990, but not published. Some revisions and additions were made by C. Williams in 1993. Crawford and Williams identified a normal fault, referred to as the Rome Fault, that crosscuts the southern portion of Victory Lake. To the east of this fault, and to the south of the quarry, Crawford and Williams also identified several vertical joint sets exposed in outcrops.

Hydrological Setting

Victory Lake is located in a topographically low area compared to regions immediately adjacent to it. The rim of the quarry's elevation is 189 masl, whereas Victory Lake's

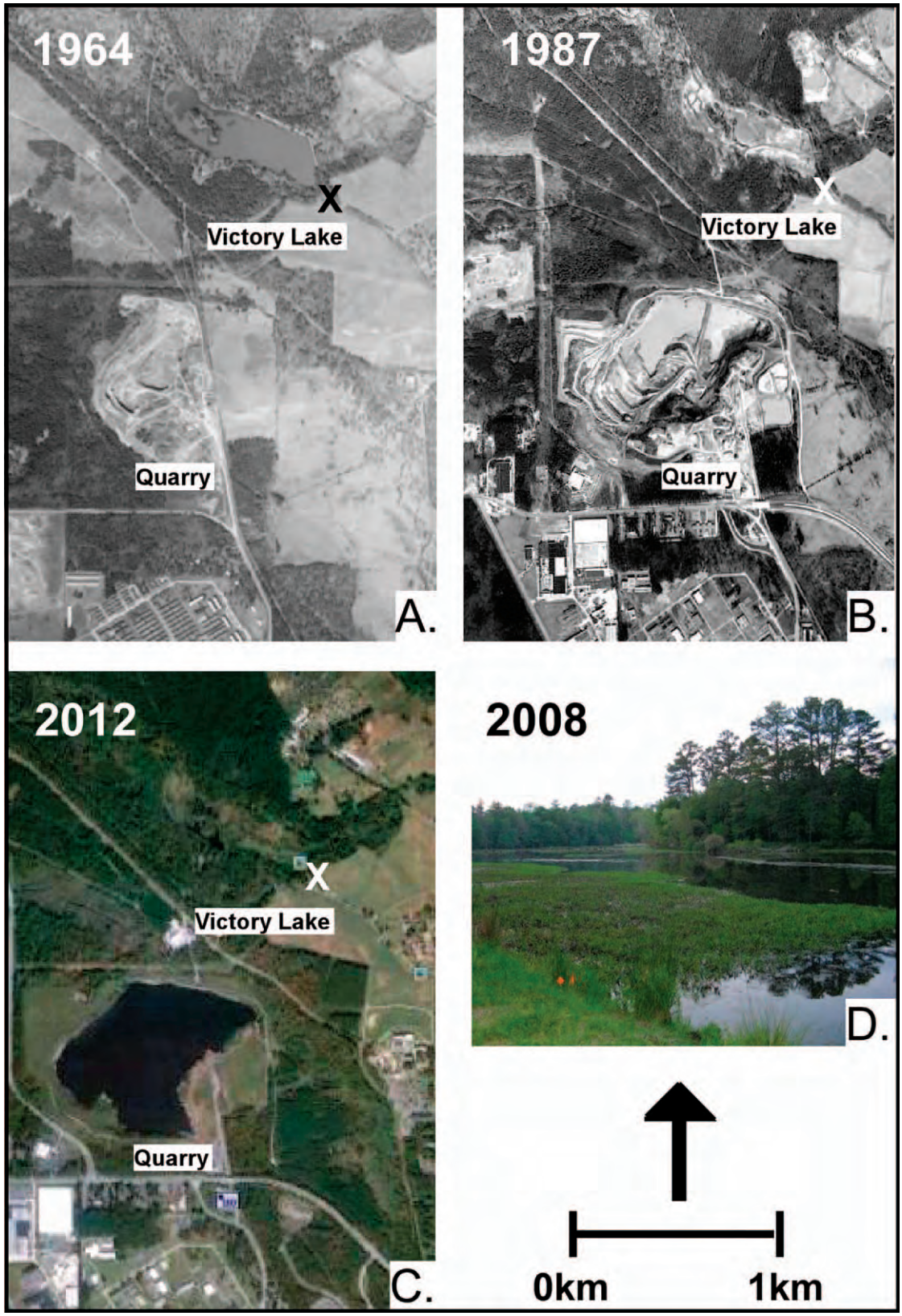

Figure 2. Aerial photography of Victory Lake. The X in photos A, B, C indicates the southeastern-most tip of Victory Lake. The photograph shown in D was taken from the southeastern-most position (X) looking north. A. This aerial photograph shows early stages of quarry excavation in 1964 and a full Victory Lake. B. This aerial photograph (1987) shows an empty Victory Lake. Notice that vegetation has not yet entered the basin. C. This 2012 aerial photograph (Google Earth) illustrates current conditions at Victory Lake. D. A photograph of Victory Lake after March (2008) rains.

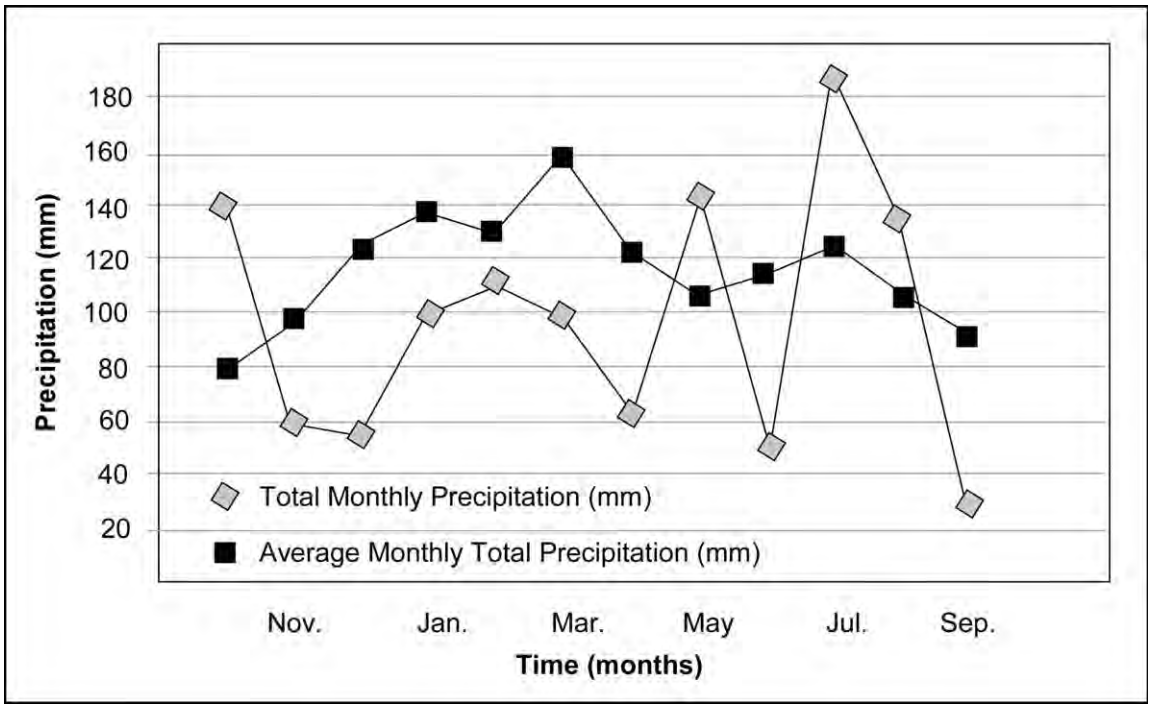

Figure 3. Average monthly total (1910–2009) precipitation (mm) measured for Rome, Georgia, (black squares) compared to the total monthly precipitation (mm) measured at Victory Lake for October 2007 to September 2008 (grey diamond). Average monthly total data were retrieved from the Georgia Automated Environmental Monitoring Network website www.georgiaweather.net.

elevation is approximately 181 masl. Under normal conditions, the groundwater flow pattern in the area is from west to east and follows the regional topography of the landscape.

An ephemeral stream with drainage basin approximately 5.0 km^2 enters Victory Lake on its northern end. Pre-1986, this creek continued from the southern end of Victory Lake to merge with Big Dry Creek. Today, a culvert funnels water from Victory Lake into Big Dry Creek.

Twenty-two monitoring wells (PZ26A and PZ16A) were installed on the main campus in June 1998 following the collapse of several campus buildings into sinkholes. The locations of two wells used for groundwater sampling in this study are shown on Figure 1. The water level data recorded from 1998–2000 provides valuable insight as to the significant depletion of the aquifer during and after the time of pumping; the quarry officially closed in 2000. The lowest depth-to-water measurement (47 m) was recorded in the well at the southern end of Victory Lake in July 1998. The water table immediately rebounded after quarry operations were halted. The current average depth to the water table is 10 m.

Climate

The mean temperature for Mount Berry over a thirty-year period is 16.5 °C. August is typically the warmest month, averaging 32.2 °C; January the coldest, averaging 11.8 °C. Average annual rainfall is 1425 mm; generally, the highest monthly rainfall occurs during March and the lowest in October. The hydrologic and climatic data collected for this paper represents one hydrologic year starting October 1 and ending September 30; see Figures 3 and 4.

Materials and Methods

Establishing Lake Water Budget

The water budget equation used in this study is $(P + I) - (ET + O) = \Delta S$, where P is precipitation, I is inflow, ET is evapotranspiration, O is outflow, and ΔS is change in storage. All water budget measurements are converted to m^3. Annual and seasonal water balances were computed based on a method from McCarthy et al. (1991) and Chescheir et al. (1995). The expression for percentage closure error is $(\Delta S_{calc} - \Delta S_{meas}) / F \times 100\%$, where F is the system flux (m^3) expressed as $F = (P + I + O + ET + |\Delta S_{calc}|) / 2$ and ΔS_{calc} is the residual storage and ΔS_{meas} is the measured storage.

Inflow and outflow stream velocity were measured weekly using a Price AA flow meter. The inflow velocity was measured at the confluence of a tributary and Victory Lake, and the outflow was measured at the culvert where the lake water has been diverted to prevent road flooding. Stage gauges were placed in these locations to measure changes in water depth over time.

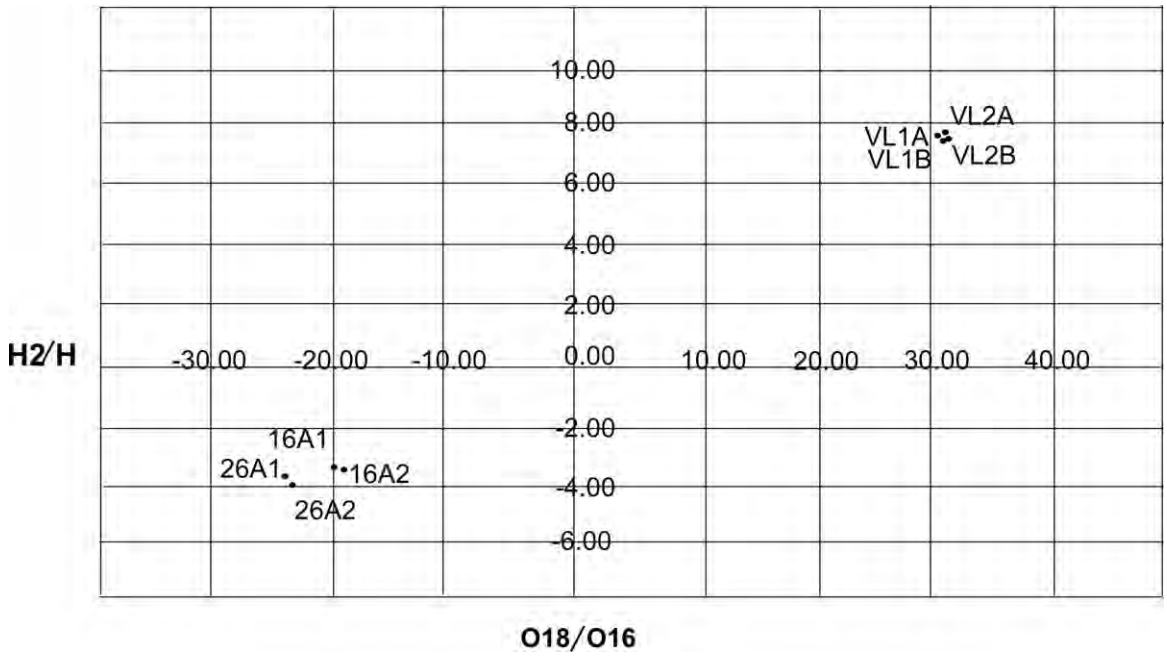

Figure 4. Average minimum/maximum monthly temperature (°C) measured for Rome, GA. Average data was retrieved from the Georgia Automated Environmental Monitoring Network website www.georgiaweather.net.

To measure precipitation onto Victory Lake, post-mounted butyrate-plastic rain gauges made to U.S. Weather Service specifications were placed in an open area at the northern and southern ends of the basin. These data were collected daily.

A Class AA evaporation pan was placed adjacent to Victory Lake in an open field free from shade and wind obstruction. The evaporation pan was visited daily from October 2007 to September 2008. The evaporation pan was stored for the winter months of December to February. Data for evapotranspiration came from the Georgia Environmental Monitoring Network website for the city of Rome.

Inorganic water chemistry data was analyzed from both the groundwater and surface water. Groundwater samples were collected at two monitoring wells in close proximity to Victory Lake (Fig. 1). Each well was purged for three hours before sample collection. Samples were immediately analyzed for general water chemistry at Berry College. Those samples collected for environmental isotopes (^{18}O and ^{2}H) were immediately placed on dry ice and mailed overnight to the University of Waterloo in Canada for analysis. The stable isotope composition of water is reported with reference to the Standard Mean Ocean Water, in parts per thousand (Craig, 1961).

A Rhodamine WT (C.I. Acid Red 388) dye tracer test was conducted in March 2008 to establish groundwater outflow or lack thereof. Standards and a calibration curve were created using concentrated stock solution of Rhodamine WT for the Model 10 Turner Designs Fluorometer. The measured injection of Rhodamine WT was based on the total liters of water calculated to be in Victory Lake during March 2008. Six liters of dye (1.428 kg) was introduced by slug injection at the northern entrance of Big Dry Creek. Groundwater samples were retrieved at monitoring well PZ26A (Fig. 1) hourly for 24 consecutive hours, then once every 4 hours for two days, then every day for three weeks.

RESULTS

GROUNDWATER

Table 1 compares inorganic water chemistry for the groundwater and surface water samples. The groundwater has higher alkalinity (222 to 246 mg L^{-1}) when compared to the surface water samples (110 to 132 mg L^{-1}). In addition, the CO_2 is considerably higher in the groundwater (18–20 mg L^{-1}) than in the surface water samples (0 to 5 mg L^{-1}). There is little variation in the amount of dissolved oxygen and nitrates among the samples. The warmer surface water has a lower pH than that of the groundwater.

Groundwater and surface water samples were analyzed for ^{18}O and ^{2}H (Fig. 5). All of the surface water samples contain larger fractions of ^{18}O and ^{2}H than the groundwater samples. The groundwater samples have a lighter signature for both ^{2}H (ranging from −3.18 to −3.94‰) and ^{18}O (ranging from −18.54 to −22.48‰).

The wells monitored (PZ26A and PZ16A) during the rhodamine-WT dye-tracer test are both located at the southern end of the lake (Fig. 1). Our fluorometer analysis did not detect any amounts of Rhodamine WT dye in the

Table 1. Surface water and groundwater chemical analyses.

	Surface Water Samples			Groundwater Samples	
Test	1-VL	2-VL	3-VL	PZ26A	PZ16A
Alkalinity, mg L^{-1}	132	112	110	246	222
CO_2, mg L^{-1}	0	5	0	20	18
Nitrate-Nitrogen, mg L^{-1}	<4.4	0	<0.2	<2	<1
Phosphate, mg L^{-1}	0	0	0	2	1
Temperature, °C	27	26.5	27	17	16.8
pH	7	6.9	6.8	7.7	7.7

groundwater samples collected throughout the three-week sampling duration.

Precipitation

The sampling months of October 2007 through September 2008 were classified as moderate drought to near-normal conditions (National Oceanic and Atmospheric Administration website, www.cpc.ncep.noaa.gov). From January 2008 to September 2008 the total rainfall recorded at Victory Lake was 915.37 mm. This was 175.54 mm lower than the yearly average for Rome, Georgia (Fig. 3). The average mean monthly temperatures recorded during the duration of the study correlates within 2 degrees to the long-term monthly average temperatures for all months, except October 2007 and December 2007, which were warmer than historic average (Fig. 4).

Evaporation

Because of the extensive in-filling of the remaining basin with sediment over twenty-seven years and the resulting overgrowth of plants, we deem evapotranspiration at Victory Lake to be more influential than evaporation. For this reason, the data we present is the evapotranspiration reported for the city of Rome found from the Georgia Environmental Monitoring Network.

Inflow and Outflow

Because Big Dry Creek is ephemeral, it only flows during periods of heavy and intense rainfall. Figure 6 compares stream inflow to direct rainfall onto the surface of the lake from October 2007 to November 2008. During periods of high rainfall, such as the months of December 2007 through March 2008, stream inflow is the dominant

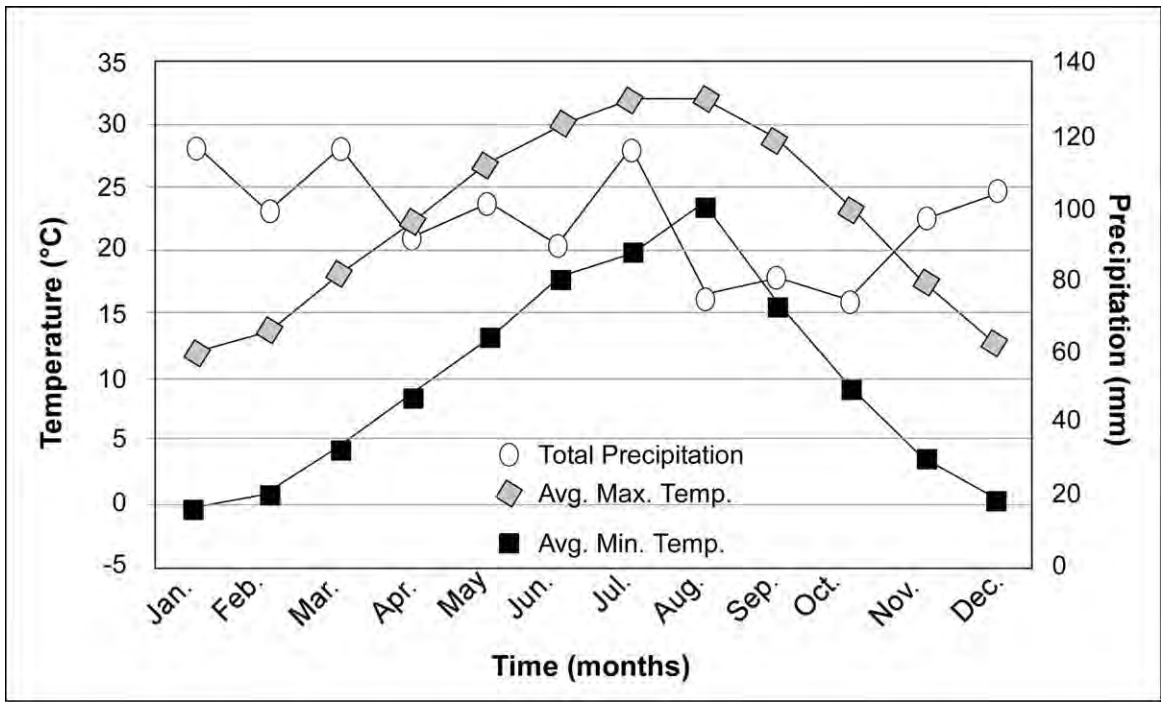

Figure 5. Groundwater (samples 16A and 26A) and surface water (samples VL1 and VL2) analyses for stable isotopes δ ^{18}O and δ ^{2}H.

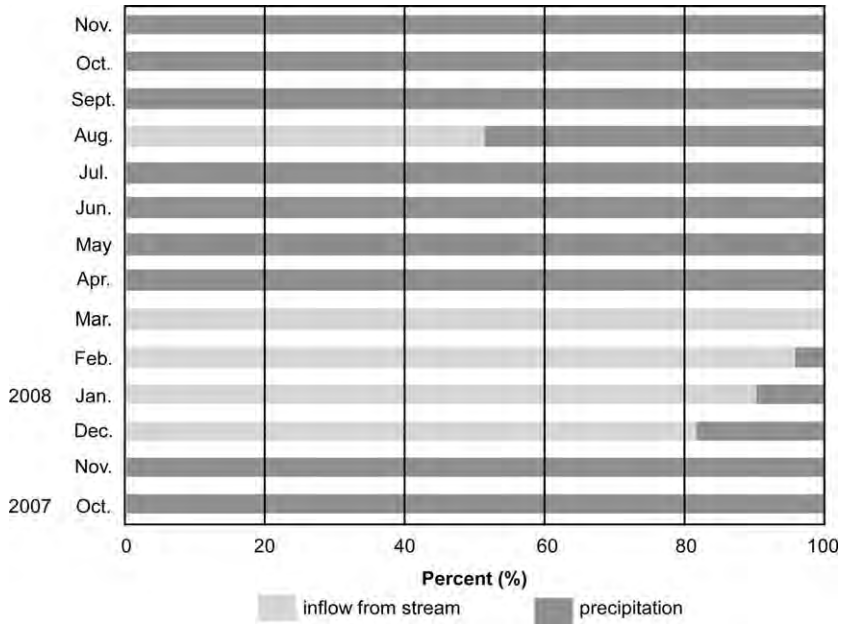

Figure 6. The percentages contributed to the water gain in Victory Lake by inflow from Big Dry Creek and rainfall directly onto the surface from October 2007 to November 2008.

process adding to the water volume in the basin. Rainfall onto its surface will be the major contributor to Victory Lake during the rest of the year. Similarly to inflow, water flow, in this case to downstream Big Dry Creek, is the dominant process of water loss when there are periods of high and intense precipitation (Fig. 7).

WATER BALANCE

Over the one-year study, Victory Lake's overall water budget indicates that the basin lost more water via evapotranspiration and surface water outflow (50.3%) than it gained via rainfall and stream inflow (49.7%) (Fig. 8). Which is the dominant variable, stream inflow,

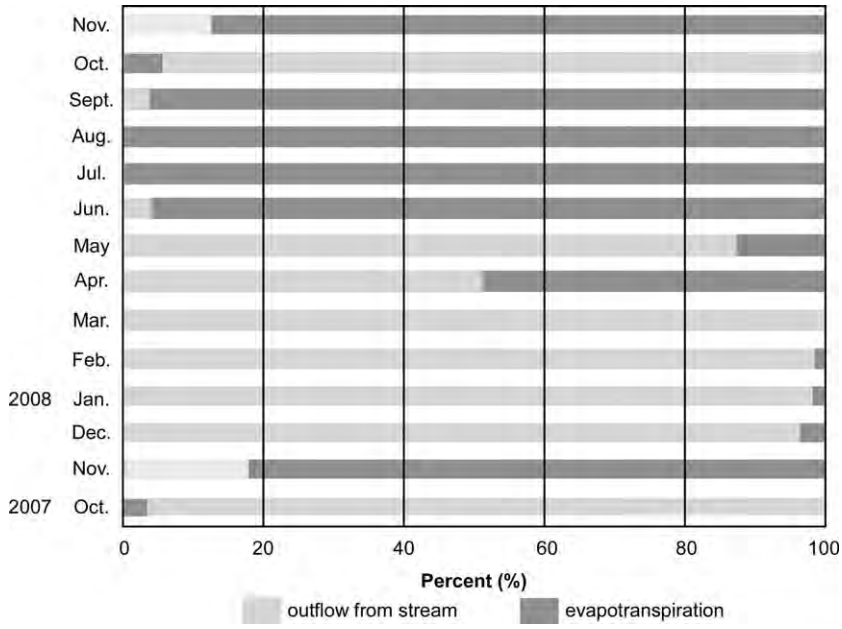

Figure 7. The percentages contributed to the water loss from Victory Lake by flow through the exit culvert and evapotranspiration from October 2007 to November 2008.

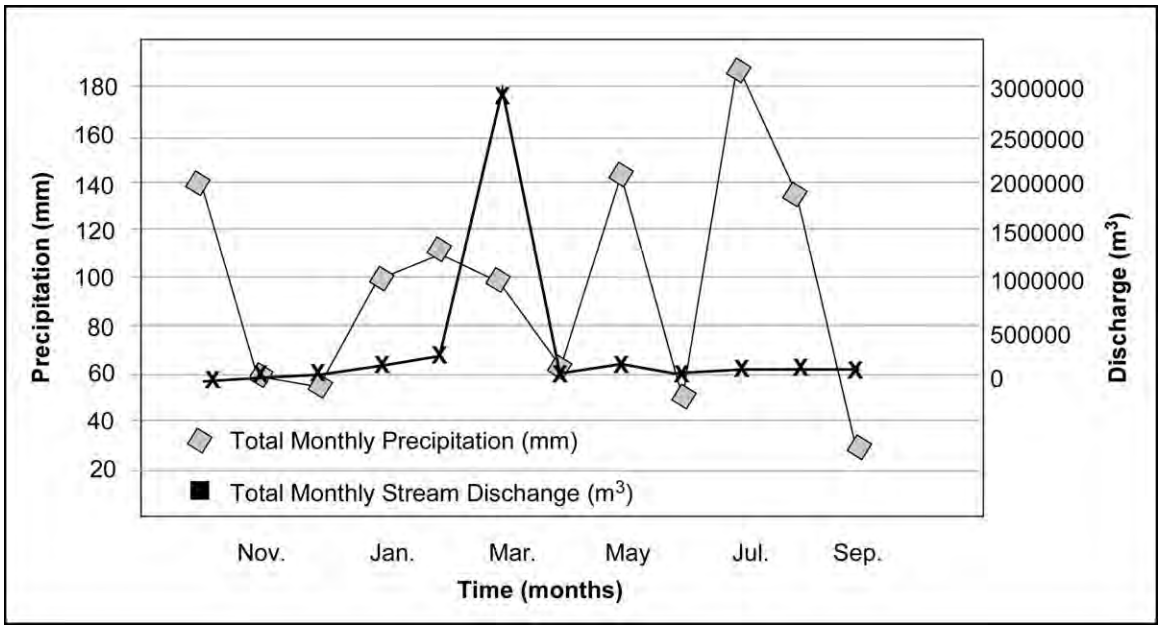

Figure 8. Total monthly precipitation recorded during the study (mm) compared to total monthly Victory Lake outflow through the exit culvert (m^3).

rainfall, evapotransiration, or stream outflow, varies seasonally. During the summer and fall months, the lake's outflow was driven by evapotranspiration, 67% and 54%, respectively. During the winter, water left the basin by stream outflow (48%). Water left the basin during the spring via outflow (41%) and evapotranspiration (37%).

Gains or losses in storage were determined by comparing the monthly fluctuations to the initial volume and surface area measured for the lake at the start of the study; the overall change for the year being negative (Table 2). Monthly increases in storage ranging from 5% to 23% occurred from October 2007 to January 2008 (Table 2). From October 2007 to January 2008 the lake volume doubles. By February 2008, however, there is a 62% decrease in storage. This reduction is followed by increases in rainfall additions and surface water inflow from spring rain events. By March 2008, the lake volume increased to 10 times that of the initial lake volume determined in September 2007. The March rains provided enough precipitation to completely fill in the lake basin. After the March storms, the storage in Victory Lake began to decrease despite May precipitation doubling that recorded in April. Losses continued to be calculated generally from May to November 2008, with a slight positive rebound in September.

A comparison of monthly inflow types (Fig. 6) reveals that direct rainfall dominated the gain during most of the study; in nine of fourteen months rainfall onto the lake contributed 100% to the inflow water budget (Fig. 6). During the winter and early spring, however, the stream provided more than 80% of the monthly inflow water budget (Fig. 6). Likewise, outflow through the culvert is the dominant process more than 90% of the time (Fig. 7). Evapotranspiration is prominent at the start of spring (March) and again in June and July, with over 95% of water being lost through plant growth then (Table 2).

DISCUSSION

The results from the chemical analyses indicate that the groundwater shows much higher evidence of alkalinity (222 and 246 mg L^{-1} compared to 110 to 132 mg L^{-1}) (Table 1). This is a typical characteristic of water pumped from a limestone aquifer (McBride et al., 2011). In addition, CO_2 is also considerably higher in the groundwater, 18 and 22 mg L^{-1} compared to the surface water's 0 to 5 mg L^{-1}. This pattern likely emerges because CO_2 is more soluble in cold water, and the monitoring well is a closed system. The variation in the amount of dissolved oxygen and nitrates between surface and groundwater is slight. As anticipated, the surface water is warmer and has a lower pH than that of the groundwater.

The Craig and Gordon (1965) model established that environmental isotopes ^{18}O and ^{2}H respond to changes in temperature, therefore analyzing ^{18}O and ^{2}H is particularly useful in the study of groundwater and surface water interactions. Several authors have successfully applied isotopic fractionation of ^{18}O and ^{2}H as a means to distinguish between groundwater and surface water in water budgets (Krabbenhoft et al., 1990a, 1990b, 1994; Yehdeghoa et al., 1997). More recently, McBride et al. (2011) used stable isotopes for similar purposes to establish inflow and outflow in a water budget. Thus, if the groundwater and surface water are connected, the ^{18}O

Table 2. Monthly water budget and storage for Victory Lake. All values in cubic meters. Lake volume is figured based on an initial estimate volume for September 2007.

	Gains to Victory Lake			Losses to Victory Lake				
Month & Year	Flow from Big Dry Creek, m^3	Rainfall onto the Lake, m^3	Total Gain, m^3	Flow out the Culvert, m^3	Evapotranspiration (GAEMN data), m^3	Total Loss, m^3	Calculated Change in Volume, m^3	Lake Volume, m^3
October 2007	0	10,668.47	10,668.47	162.59	5,281.90	5,444.51	5,222.96	24,637.96
November 2007	0	4,505.39	4,505.39	609.39	2,693.04	3,302.34	1,203.05	25,841.01
December 2007	19,407.05	4,136.59	23,543.65	14,912.27	789.60	15,701.87	7,841.78	33,682.79
Janunary 2008	73,084.69	7,486.18	80,570.87	77,169.21	1,812.72	78,981.93	1,588.94	35,271.73
February 2008	214,327.29	8,448.09	222,775.38	233,551.60	2,748.48	236,300.08	−13,524.70	21,747.03
March 2008	2,919,790.8	7,497.58	2,927,288.38	2,831,445.22	5,310.48	2,836,755.70	90,532.68	112,279.71
April 2008	0	4,752.52	4,752.52	8,886.56	7,943.04	16,829.60	−12,077.07	100,202.64
May 2008	0	10,984.04	10,984.04	100,612.96	10,232.88	110,845.84	−99,861.81	340.83
June 2008	0	1,923.82	1,923.82	488.84	12,902.40	13,391.24	−11,467.42	0
July 2008	0	6,204.89	6,204.89	0	12,099.36	12,099.36	−5,894.46	0
August 2008	12,439.68	11,618.97	24,058.65	22,003.18	10,341.24	32,344.42	−8,285.77	0
September 2008	0	216.71	216.71	0	7,659.12	7,659.12	−7,442.40	889.17
October 2008	0	5,877.92	5,877.92	0	4,988.76	4,988.76	889.17	135.83
November 2008	0	1,475.18	1,475.18	0	2,228.52	2,228.52	−753.34	0
Study Period Average	2,31,360.68	6,128.31	237,488.99	234,988.69	6,216.54	241,205.23	−3,716.24	•••

and ^{2}H signatures should be similar. Conversely, if the groundwater and surface water are not connected, the results will be distinctly different. The data shown in Figure 5 indicate that the surface water samples are heavier in ^{18}O and ^{2}H. This occurs when the surface water samples have undergone evaporation processes that selectively remove the lighter isotopes (^{16}O and ^{1}H), leaving an excess of ^{18}O and ^{2}H. The groundwater samples show the opposite signature. The distinct difference in the environmental isotope signatures of groundwater and surface water samples indicate that during our study it is likely that the systems were not connected. In addition, from monitoring wells at the southern end of the lake, we measured changes in the water table weekly. Throughout the study the groundwater table was more than 9 m below the surface. With this evidence we chose to eliminate groundwater inflow from our water budget.

Lake-water seepage into the ground is a challenging parameter to measure. In this study we conducted a Rhodamine WT fluorescent dye-tracer test to check for seepage from surface water to groundwater through a slug injection at the northern end of Victory Lake. During our sampling interval we did not measure any Rhodamine WT in groundwater samples. Next, we considered the very distinct environmental isotope results we retrieved for the groundwater and surface water samples. Moreover, we considered that, prior to human-induced sinkhole formation at the southern end of Victory Lake, the lake basin, which is floored with clay, held water for nearly sixty years. For the purposes of this water budget we eliminated groundwater outflow as a parameter during the duration of the study. Future studies will include geophysical investigation to confirm groundwater flow paths.

The inflow variables measured in this study include inflow from Big Dry Creek draining into Victory Lake and rainfall onto it. This study determined that the stream is ephemeral and only flows after intense rainfall events ($>$ 35 mm) or prolonged rainfall (12 hours or greater). The drainage basin of the primary stream is 5 km^2. The area adjacent to the stream just upstream of the lake is a cypress wetland that is usually saturated when we record considerable inflow entering Victory Lake. For the overall water budget of Victory Lake inflow makes up 48% (Fig. 3). However, when looking at monthly percentages rainfall dominated over stream inflow for most months. This discrepancy is explained by looking at the amount of water entering the system. When substantial precipitation events occur, then surface runoff will contribute to the inflow volume of the stream. The stream does not flow at other times. Therefore, the effects of major precipitation events are multiplied by the surface water runoff into by the stream. These jumps in stream inflow volume were seen in December 2007 through March 2008 (Table 2). Moreover, when precipitation events are lesser in duration and intensity, as from April 2008 to July 2008, the stream does not flow.

During the winter and early spring months the outflow leaving through the culvert was the dominant process occurring >95% of the time (Fig. 7). As would be expected, the other outflow component, evapotranspiration, became more prominent during spring and summer months (Fig. 7). Since Victory Lake emptied in 1986, the lake basin has not been full for prolonged periods of time. As a result, fast-growing plants and sedimentation have encroached on the basin to infill most portions. This is why we consider evaportranspiration in this study. More influential by volume of total loss than evapotranspiration was the amount of water lost through the culvert at the southern end of the lake basin (49% overall).

Conclusions

Nature or human-induced hydrologic changes can alter the fundamental character of karst sites. Worldwide, sinkholes have been an increasing problem. For example, a 60 km stretch of land along the Dead Sea coast has seen an increase in new sinkhole formation at the rate of 150 to 200 per year, causing drastic alterations to nearby lakes and groundwater flow paths (Yechieli et al., 2006). Similar challenges have been documented in eastern England and western Greece (Cooper et al., 2013; Deligianni et al., 2013). As seen most recently with the emptying of the lakes at Five Blues Lake National Park, Belize, natural or human-induced hydrologic changes can alter the fundamental character of karst sites (Day and Reynolds, 2012). Similar to Five Blue Lake National Park, Floridian lakes Jackson and Scott have also experienced draining due to sinkhole activity (Penson, 2002; McBride et al., 2011). Various water budgets calculated by USGS investigators in karstic areas, like Florida, have helped researchers to better understand water movement and seasonal variability (Dalton et al., 2004; Spechler, 2010; McBride et al., 2011; Sepúlveda et al., 2012). This case study presents a water budget that combines the approaches used by Dalton et al., Spechler, and McBride et al., but was applied to capture a signature of the Rome Formation limestone aquifer in the Ridge and Valley Province of northwest Georgia.

Victory Lake was once a popular, picturesque meeting place and a focal point for visitors and recreation. Sinkhole collapse at Victory Lake twenty-seven years ago resulted in drastic change to campus aesthetics. The restoration of the lake to its original state is of interest to the faculty, students, and staff. From the data collected and analyzed for this study we believe that restoration of Victory Lake is possible. Since the quarrying operations concluded in 2000 there has not been significant sinkhole formation occurring on campus, and the water table has rebounded. Through the development of this water budget we were able to confirm that the groundwater table has stabilized and that the current basin could hold water well enough to support a lake. There are two main reasons that the overall water budget for the lake showed a loss. Over the past

twenty-seven years the lake has not been maintained or dredged. Ephemeral inflow from Big Dry Creek has caused sedimentation to occur within the basin, causing it to shallow from 2.5-m deep to less than 1 m. The shallow basin morphology encourages surface water to run off quickly. As seen in Figures 2c and 2d, during the growing seasons of spring and summer evapotranspiration due to plant encroachment into the lake drastically reduces the amount of water left in the basin. However, the author admits that only long-term monitoring and continual data collection would confirm that the lake perennially loses more water than it gains, as this research provides limited data for only one hydrologic year.

The challenge in dealing with situations involving the rapid emptying of karst lakes, as suggested by Day and Reynolds (2012), is that sudden underground drainage is a rare phenomenon. The evidence for success of management and restoration of such landscapes to their original form is inconclusive. Although several creative engineering strategies, such as a clay or synthetic liner and a supplemental water supply, have been suggested to rebuild Victory Lake, it remains difficult to weigh the financial investment against the limited guarantee suggested by karst topography. Moreover, the repercussions of the lake emptying for a second time could be the destabilization of downgradient cover-collapse or cover-subsidence sinkholes on campus. This long-term risk to the human health, building infrastructure, and economic loss should be weighed.

Day and Reynolds (2012) suggest that appropriate management strategies in karst terrains should acknowledge the temporal variability of the hydrologic regime and prepare visitors for an experience falling within a wide spectrum of hydrologic conditions. Perhaps this management strategy should be considered at Victory Lake. The current landscape at Victory Lake lends itself easily to a pleasing wetland environment that hosts varying wildlife seasonally. In addition, the mystic of visiting a ''disappearing lake'' may provide a unique and interesting environmental interpretation of living in a dynamic karst landscape.

ACKNOWLEDGEMENTS

The author would like to thank the sponsors of the Laura Maddox Smith Environmental Science Grant for providing project funding and NSF grant 0620101 for providing resources and support. Gratitude is extended to the Berry College students who helped in collecting data: Melissa Kemm, Roy Srymanske, Joshua Stevenson, and Lauryn Gilmer.

REFERENCES

Anderson, C., 1993, Index and short description of the geologic terms used by the GSS: Bulletin of the Georgia Speleological Survey, v. 25, p. 4–8.

Aurit, M.D., Peterson, R.O., and Blanford, J.I., 2013, A GIS analysis of the relationship between sinkholes, dry-well complaints and groundwater pumping for frost-freeze protection of winter strawberry production in Florida: PLoS ONE, v. 8, no. 1, p. 163–167. doi:10.1371/journal.pone.0053832.

Benito, G., Pérez del Campo, P., Gutiérrez-Elorza, M., and Sancho, C., 1995, Natural and human-induced sinkholes in gypsum terrain and associated environmental problems in NE Spain: Environmental Geology, v. 25, no. 3, p. 156–164. doi:10.1007/BF00768545.

Buhlman, K.A., 2001, A biological inventory of eight caves in northwestern Georgia with conservation implications: Journal of Cave and Karst Studies, v. 63, no. 3, p. 91–98.

Chescheir, G.M., Amatya, D.M., and Skaggs, R.W., 1995, Monitoring the water balance of a natural wetland, *in* Cambell, K.L., ed., Versatility of Wetlands in the Agricultural Landscape: St. Joseph, Michigan, American Society of Agricultural Engineers, p. 451–462.

Cooper, A.H., Odling, N.E., Murphy, P.J., Miller, C., Greenwood, C.J., and Brown, D.S., 2013, The role of sulfate-rich springs and groundwater in the formation of sinkholes over gypsum in eastern England, *in* Land, L., Doctor, D.H., and Stephenson, J.B., eds., Proceedings of the 13th Multidisciplinary Conference on Sinkhole and the Engineering and Environmental Impacts of Karst: Carlsbad, National Cave and Karst Research Institute, Symposium 2, v. 13, p. 141–150.

Craig, H., 1961, Isotopic variations in meteoric waters: Science, v. 133, p. 1702–1703. doi:10.1126/science.133.3465.1702.

Craig, H., and Gordon, L.I., 1965, Deuterium and oxygen 18 variations in the ocean and marine atmosphere, *in* Tingiorgi, E., ed., Stable Isotopes in Oceanographic Studies and Paleotemperatures: Pisa, Laboratorio de Geologia Nucleare, p. 9–130.

Dalton, M.S., Aulenbach, B.T., and Torak, L.J., 2004, Ground-Water and Surface-Water Flow and Estimated Water Budget of Lake Seminole, Southwestern Georgia, and Northwestern Florida: U.S. Geological Survey, Scientific Investigations Report 2004-5073, 49 p.

Day, M., and Reynolds, B., 2012, Five Blues Lake National Park, Belize: A cautionary management tale: Journal of Cave and Karst Studies, v. 74, no. 2, p. 213–220. doi:10.4311/2011JCKS0203.

Deevey, S.E., Jr., 1988, Estimation of downward leakage from Florida lakes: Limnology and Oceanography, v. 33, no. 6, p. 1308–1320.

Deligianni, M.G., Veni, G., and Pavlopoulos, K., 2013, Land use and limitations in the sinkhole and polje karst of the Ksiromero Region, Western Greece: Carbonates and Evaporites, v. 28, no. 1–2, p. 167–173. doi:10.1007/s13146-013-0133-x.

Fidelibus, M.D., Gutiérrez, F., and Spilotro, G., 2011, Human-induced hydrogeological changes and sinkholes in the coastal gypsum karst of Lesina Marina area (Foggia Province, Italy): Engineering Geology, v. 118, no. 1–2, p. 1–19. doi:10.1016/j.enggeo.2010.12.003.

Florea, L.J., Budd, D., and Brinkmann, R., 2009, Caves and karst of West-Central Florida, *in* Palmer, A.N., and Palmer, M.V., eds., Caves and Karst of the USA; Huntsville, National Speleological Society, p. 189–196.

Hamilton-Smith, E., 2006, Spatial planning and protection measure for karst areas: Acta Carsologica, v. 35, no. 2, p. 5–11.

Healy, R.W., Winter, T.C., LaBaugh, J.W., and Franke, O.L., 2007, Water Budgets: Foundations for Effective Water-Resources and Environmental Management: US Geological Survey, Circular 1308, 90 p.

Hebbert, R.H.B., and Smith, R.E., 1990, Hillslope parameter estimation using the inverse procedure: Journal of Hydrology, v. 119, p. 307–334. doi:10.1016/0022-1694(90)90049-4.

Horvat, B., and Rubinic, J., 2006, Annual runoff estimation—an example of karstic aquifers in the transboundary region of Croatia and Slovenia: Hydrological Sciences Journal, v. 51, no. 2, p. 314–324. doi:10.1623/hysj.51.2.314.

Hubbard, D.A., Jr., 1988, Selected Karst Features of the Central Valley and Ridge Province: Virginia Division of Mineral Resources, Publication 83, 1:250,000 scale map with text.

Jenkins, M., 2009, Deep southern caves: National Geographic Magazine, June, 2009, p. 124–141.

Krabbenhoft, D.P., Anderson, M.P., and Bowser, C.J., 1990a, Estimating groundwater exchange with lakes: 2. Calibration of a three-dimensional, colute transport model to a stable isotope plume: Water Resources Research, v. 26, p. 2455–2462. doi:10.1029/WR026i010p02455.

Krabbenhoft, D.P., Bowser, C.J., Anderson, M.P., and Valley, J.W., 1990b, Estimating groundwater exchange with lakes: 1. The stable isotope mass balance method: Water Resources Research, v. 26, p. 2445–2453. doi:10.1029/WR026i010p02445.

Krabbenhoft, D.P., Bowser, C.J., Kendall, C., and Gat, J.R., 1994, Use of oxygen-18 and deuterium to assess the hydrology of groundwater/lake systems, *in* Baker, L.A., ed., Environmental Chemistry of Lakes and Reservoirs: Washington, D.C., American Chemical Society, p. 67–90. doi:10.1021/ba-1994-0237.ch003.

Lindsey, B.D., Katz, B.G., Berndt, M.P., Ardis, A.F., and Skach, K.A., 2010, Relations between sinkhole density and anthropogenic contaminants in selected carbonate aquifers in the eastern United States: Environmental Earth Sciences, v. 60, no. 5, p. 1073–1090. doi:10.1007/s12665-009-0252-9.

Loague, K.M., and Freeze, R.A., 1985, A comparison of rainfall-runoff modeling techniques on small upland catchments: Water Resources Research, v. 21, no. 2, p. 229–248. doi:10.1029/WR021i002p00229.

MacIntyre, D.F., 1986, A quantitative review of the hydrology of Lake Jackson, Florida, 1971-81, [Masters Thesis]: Gainesville, University of Florida, 238 p.

Martinez, J.D., Johnson, K.S., and Neal, J.T., 1998, Sinkholes in evaporite rock: American Scientist, v. 86, no. 1, p. 38–51. doi:10.1511/1998.1.38.

McBride, W.S., Bellino, J.C., and Swancar, A., 2011, Hydrology, Water Budget, and Water Chemistry of Lake Panasoffkee, West-Central Florida: U.S. Geological Survey Scientific Investigations Report 2010–5237, 96 p.

McCarthy, E.J., Skaggs, R.W., and Farnum, P., 1991, Experimental determination of the hydrologic components of a drained forest watershed: Transactions of the ASABE, v. 34, no. 5, p. 2031–2039.

Newton, J.G., 1987, Development of sinkholes resulting from man's activities in the Eastern United States: U.S. Geological Survey, Circular 968, 54 p.

Penson, G., 2002, Restoring a disappearing lake: Land and Water, v. 46, no. 5, p. 1–10.

Praise, M., and Gunn, J., 2007, Natural and Anthropogenic Hazards in Karst Areas: Recognition, Analysis and Mitigation: London, Geological Society Special Publications 279, 202 p.

Rosenberry, D.O., Sturrock, A.M., and Winter, T.C., 1993, Evaluation of the energy budget method of determining evaporation at Williams Lake, Minnesota, using alternative instrumentation and study approaches: Water Resources Research, v. 29, no. 8, p. 2473–2483. doi:10.1029/93WR00743.

Scheidt, J., Lerche, I., and Paleologos, E., 2005, Environmental and economic risks from sinkholes in west-central Florida: Environmental Geosciences, v. 12, p. 207–217. doi:10.1306/eg.05130404009.

Schuster, P.F., Reddy, M.M., LaBaugh, J.W., Parkhurst, R.S., Rosenberry, D.O., Winter, T.C., Antweiler, R.C., and Dean, W.E., 2003, Characterization of lake water and ground water movement in the littoral zone of Williams Lake, a closed-basin lake in north central Minnesota: Hydrologic Processes, v. 17, no. 4, p. 823–838. doi:10.1002/hyp.1211.

Sepúlveda, N., Tiedeman, C.R., O'Reilly, A.M., Davis, J.B., and Burger, P., 2012, GroundwaterFlow and Water Budget in the Surficial and Floridan Aquifer Systems in East-Central Florida: U.S. Geological Survey Scientific Investigations Report 2012-5161, 214 p.

Spechler, R.M., 2010, Hydrogeology and Groundwater Quality of Highlands County, Florida: U.S. Geological Survey Scientific Investigations Report 2010–5097, 84 p.

Weary, D.J., 2005, An Appalachian regional karst map and progress towards a New National Karst Map, *in* Kuniansky, E.L., ed., U.S. Geological Survey Karst Interest Group Proceedings, Rapid City, South Dakota, September 12–15, 2005: U.S. Geological Survey Scientific Investigations Report 2005-5160, p. 93–102.

Winstanley, D., Angel, J.A., Changnon, S.A., Knapp, H.V., Kunkel, K.E., Palecki, M.A., Scott, R.W., and Wehrmann, H.A., 2006, The Water Cycle and Water Budgets in Illinois: A Framework for Drought and Water-Supply Planning: Champaign, Illinois, Illinois State Water Survey I/EM 2006-02, 114 p.

Winstanley, D., and Wendland, W.M., 2007, Climate change and associated changes to the water budget, *in* Dando, W.A., ed., Climate Change and Variations: A Primer for Teachers, v. 1, National Council for Geographic Education, Pathways in Geography 35.

Winter, T.C., 1981, Uncertainties in estimating the water balance of lakes: Journal of American Water Resources Association, v. 17, no. 1, p. 82–115.

Winter, T.C., 1985, Approaches to the study of lake hydrology, *in* Likens, G.E., ed., Ecosystem Approach to Aquatic Ecology: Mirror Lake and its Environment, p. 128–135.

Winter, T.C., 1999, Relation of streams, lakes, and wetlands to groundwater flow systems: Hydrogeology Journal, v. 7, p. 28–45. doi:10.1007/s100400050178.

Yechieli, Y., Abelson, M., Bein, A., Crouvi, O., and Shtivelman, V., 2006, Sinkhole "swarms" along the Dead Sea coast: Reflection of disturbance of lake and adjacent groundwater systems: Geological Society of America Bulletin, v. 118, no. 9-10, p. 1075–1087. doi:10.1130/B25880.1.

Yehdeghoa, B., Rozanski, K., Zojer, H., and Stichler, W., 1997, Interaction of dredging lakes with the adjacent groundwater field: an isotope study: Journal of Hydrology, v. 192, p. 247–270. doi:10.1016/S0022-1694(96)03102-2.

BOOK REVIEW

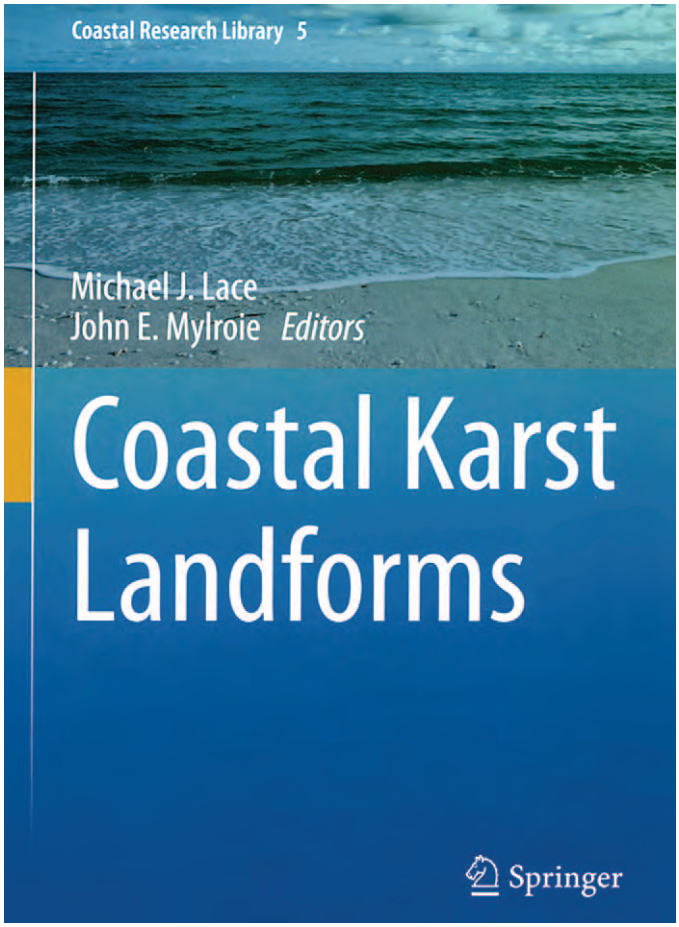

Coastal Karst Landforms

Michael J. Lace and John E. Mylroie (eds.), 2013. Coastal Research Library, vol. 5, Springer, Dordrecht, The Netherlands, 429 p. ISBN 978-94-007-5015-9, $129 (hard-cover, 7.2 × 10.2 inches), $99 (eBook – PDF format).

This book is part of a series on coastal research written for geoscientists and land managers, but which will also appeal to non-technical cavers. Most of the twenty-one authors are from the group of American scientists and cartographers coordinated by John and Joan Mylroie of Mississippi State University. This book is a summary of their work on island karst over the past thirty years. Other contributors include specialists in various fields or geographic areas. Each chapter has separate authorship, and although they vary in depth and style, they are well integrated. The result is the most accessible coverage of this topic and is an important addition to the karst literature.

The book gives a positive impression, with its clear layout, striking color photos, well-drafted illustrations, and glossary. It includes two parts: principles of coastal karst development, and selected case studies. Topics in the first section include pseudokarst caves, erosional and depositional features, hydrology and geochemistry, coastal karst development in carbonate rocks, biology and archeology, and karst resources management. The chapter on coastal karst development is perhaps the focal point of the section, as it lays out the various models of cave origin devised by the team. This includes the well-known Carbonate Island Karst Model, which associates various karst styles with the local geologic setting. Coverage of biology is brief. It could have expanded to include the occurrence of guano, which on several islands has spawned an important industry, and microorganisms, which play important roles in redox reactions.

Part 2 describes specific examples of coastal karst that have been much cited as type examples. With its detailed cave descriptions, this section will be of interest to non-technical cavers. These chapters include the Bahama Islands, Puerto Rico and its outlying islands, Barbados, Mallorca, the Mariana Islands, sea caves along the western U.S. coast, Florida, and the Yucatan Peninsula. On large islands such as Puerto Rico, the coverage of karst is limited to coastal features, since the great amount of strictly meteoric karst lies outside the scope of the book. In areas where there is a genetic relationship between coastal karst and inland features, the coverage includes both. Especially relevant to karst researchers is the revelation that in Mallorca and the Yucatan Peninsula the typical spongework pattern of coastal caves is related to poorly cemented, young limestones and is not specific to saltwater-freshwater mixing. A chapter on coastal karst in telogenetic limestones is interesting. While other chapters make distinctions between true karst and pseudokarst, this chapter gives examples of voids formed in indurated limestone that mimic the shapes of flank-margin caves.

Limits on space and time were apparent in some chapters. Coverage of coastal caves in Australia has a narrow focus, as it covers mainly a few caves visited by the authors. An overview of the coastal karst research by authors such as the late Joe Jennings would have been a good addition. There is no mention of caves in the huge Nullarbor Plateau, many of which open to the ocean and are thought to represent relict sea-level stands. Those interested in the mixing-zone model might wish for a chapter on chemical field data that support the solutional models. It also would have been instructive to include an overview of the significance of coastal karst in interpreting past sea-level stands and their relationship to other sea-level indicators.

DOI: 10.4311/2013ES0129

This book is a fine addition to the karst literature. It covers a topic that had received only sparse coverage before this group of authors began their long-term focus on coastal and island karst. Its details are largely geomorphic and descriptive, which makes it attractive to a wide readership, but it includes enough concepts and detailed site analyses to make it of technical value as well.

Reviewed by Margaret V. Palmer, 619 Winney Hill Road, Oneonta, NY 13820 (palmeran@oneonta.edu).

GUIDE TO AUTHORS

The *Journal of Cave and Karst Studies* is a multidisciplinary journal devoted to cave and karst research. The *Journal* is seeking original, unpublished manuscripts concerning the scientific study of caves or other karst features. Authors do not need to be members of the National Speleological Society, but preference is given to manuscripts of importance to North American speleology.

LANGUAGES: The *Journal of Cave and Karst Studies* uses American-style English as its standard language and spelling style, with the exception of allowing a second abstract in another language when room allows. In the case of proper names, the *Journal* tries to accommodate other spellings and punctuation styles. In cases where the Editor-in-Chief finds it appropriate to use non-English words outside of proper names (generally where no equivalent English word exists), the *Journal* italicizes them. However, the common abbreviations i.e., e.g., et al., and etc. should appear in roman text. Authors are encouraged to write for our combined professional and amateur readerships.

CONTENT: Each paper will contain a title with the authors' names and addresses, an abstract, and the text of the paper, including a summary or conclusions section. Acknowledgments and references follow the text.

ABSTRACTS: An abstract stating the essential points and results must accompany all articles. An abstract is a summary, not a promise of what topics are covered in the paper.

STYLE: The *Journal* consults The Chicago Manual of Style on most general style issues.

REFERENCES: In the text, references to previously published work should be followed by the relevant author's name and date (and page number, when appropriate) in parentheses. All cited references are alphabetical at the end of the manuscript with senior author's last name first, followed by date of publication, title, publisher, volume, and page numbers. Geological Society of America format should be used (see http://www.geosociety.org/pubs/geoguid5.htm). Please do not abbreviate periodical titles. Web references are acceptable when deemed appropriate. The references should follow the style of: Author (or publisher), year, Webpage title: Publisher (if a specific author is available), full URL (e.g., http://www.usgs.gov/citguide.html) and date when the web site was accessed in brackets; for example [accessed July 16, 2002]. If there are specific authors given, use their name and list the responsible organization as publisher. Because of the ephemeral nature of websites, please provide the specific date. Citations within the text should read: (Author, Year).

SUBMISSION: Effective February 2011, all manuscripts are to be submitted via Peertrack, a web-based system for online submission. The web address is http://www.edmgr.com/jcks. Instructions are provided at that address. At your first visit, you will be prompted to establish a login and password, after which you will enter information about your manuscript (e.g., authors and addresses, manuscript title, abstract, etc.). You will then enter your manuscript, tables, and figure files separately or all together as part of the manuscript. Manuscript files can be uploaded as DOC, WPD, RTF, TXT, or LaTeX. A DOC template with additional manuscript specifications may be downloaded. (Note: LaTeX files should not use any unusual style files; a LaTeX template and BiBTeX file for the *Journal* may be downloaded or obtained from the Editor-in-Chief.) Table files can be uploaded as DOC, WPD, RTF, TXT, or LaTeX files, and figure files can be uploaded as TIFF, EPS, AI, or CDR files. Alternatively, authors may submit manuscripts as PDF or HTML files, but if the manuscript is accepted for publication, the manuscript will need to be submitted as one of the accepted file types listed above. Manuscripts must be typed, double spaced, and single-sided. Manuscripts should be no longer than 6,000 words plus tables and figures, but exceptions are permitted on a case-by-case basis. Authors of accepted papers exceeding this limit may have to pay a current page charge for the extra pages unless decided otherwise by the Editor-in-Chief. Extensive supporting data will be placed on the *Journal*'s website with a paper copy placed in the NSS archives and library. The data that are used within a paper must be made available. Authors may be required to provide supporting data in a fundamental format, such as ASCII for text data or comma-delimited ASCII for tabular data.

DISCUSSIONS: Critical discussions of papers previously published in the *Journal* are welcome. Authors will be given an opportunity to reply. Discussions and replies must be limited to a maximum of 1000 words and discussions will be subject to review before publication. Discussions must be within 6 months after the original article appears.

MEASUREMENTS: All measurements will be in Systeme Internationale (metric) except when quoting historical references. Other units will be allowed where necessary if placed in parentheses and following the SI units.

FIGURES: Figures and lettering must be neat and legible. Figure captions should be on a separate sheet of paper and not within the figure. Figures should be numbered in sequence and referred to in the text by inserting (Fig. x). Most figures will be reduced, hence the lettering should be large. Photographs must be sharp and high contrast. Color will generally only be printed at author's expense.

TABLES: See http://www.caves.org/pub/journal/PDF/Tables.pdf to get guidelines for table layout.

COPYRIGHT AND AUTHOR'S RESPONSIBILITIES: It is the author's responsibility to clear any copyright or acknowledgement matters concerning text, tables, or figures used. Authors should also ensure adequate attention to sensitive or legal issues such as land owner and land manager concerns or policies.

PROCESS: All submitted manuscripts are sent out to at least two experts in the field. Reviewed manuscripts are then returned to the author for consideration of the referees' remarks and revision, where appropriate. Revised manuscripts are returned to the appropriate Associate Editor who then recommends acceptance or rejection. The Editor-in-Chief makes final decisions regarding publication. Upon acceptance, the senior author will be sent one set of PDF proofs for review. Examine the current issue for more information about the format used.

ELECTRONIC FILES: The *Journal* is printed at high resolution. Illustrations must be a minimum of 300 dpi for acceptance.

Journal of Cave and Karst Studies

Volume 76 Number 3 December 2014

***Journal of Cave and Karst Studies* Distribution Changes**

During the November 9, 2013, Board of Governors meeting, the BOG voted to change the *Journal* to electronic distribution for all levels of membership beginning with the April 2014 issue. Upon publication, electronic files (as PDFs) for each issue will be available for immediate viewing and download through the Member Portal on www.caves.org. For those individuals that wish to continue to receive the *Journal* in a printed format, it will be available by subscription for an additional fee. Online subscription and payment options will be made available through the website in the near future. Until then, you can arrange to receive a print subscription of the *Journal* by contacting the NSS office at (256) 852-1300.